國 立 交 通 大 學

應用化學系分子科學碩士班

碩 士 論 文

利用法蘭克-康登擬合綠色螢光蛋白質發色團的吸收與螢光光譜

Franck-Condon Simulation of Absorption and Fluorescence Spectra for GFP Chromophore

研 究 生：黃琮偉 (Tsung-Wei Huang)

指導教授：朱超原 (Chao-Yuan Zhu)

中華民國 一〇〇年

利用法蘭克-康登擬合綠色螢光蛋白質發色團的吸收與螢光光譜

研究生: 黃琮偉　　指導教授: 朱超原

國立交通大學應用化學系分子科學碩士班

摘要

綠色螢光蛋白質的發色團是經過分子內的一些反應而形成，由第 65 號的絲胺酸(serine-65)、第 66 號的酪胺酸(tyrosin-66)和第 67 號的甘胺酸(glycine-67)組成主要的結構，而紅色螢光蛋白質的發色團則是由第 66 號的谷氨醯胺(glutamine-66)、第 67 號的酪胺酸(tyrosin-67)和第 68 號的甘胺酸(glycine-68)所組成。綠色以及紅色螢光蛋白質的發色團同時具有 4-hydroxybenzylideneimidazolinone 的部分，但 imidazolinone ring 所連接的官能基則不同。將兩者發色團的吸收性質互相比較，若所連接的官能基是 Π 共軛系統，將會造成明顯的紅位移。

在本研究工作裡，我們主要使用法蘭克-康登擬合(Franck-Condon simulation)綠色和紅色螢光蛋白質之發色團的吸收以及螢光光譜，而法蘭克-康登擬合的過程包含了均勻與非均勻加寬和簡諧與非簡諧的討論。在基態的計算方面，則使用了三種不同交換-相關效應的密度泛函(B3LYP, B3LYP-35, and BHandHLYP)和 Hartree-Fock 方法，結合使用極化連續模型來計算溶劑效應。而在激發態的計算方面，則必須基於使用相同層級的 *ab initio* 方法，例如含時密度泛函理論(TD-DFT)對應密度泛函理論(DFT)、單電子激發組態交互作用(CIS)則對應 Hartree-Fock 方

法。

本研究成果成功的論述了 **HBDI** 的吸收和螢光光譜，不論是在譜峰的位置，抑或是光譜的寬度，與實驗光譜相比都具有很好的一致性。

Franck-Condon Simulation of Absorption and Fluorescence Spectra for GFP Chromophore

Student: Tsung-Wei Huang Advisor: Dr. Chao-Yuan Zhu

Department of Applied Chemistry and Institute of Molecular Science

National Chiao Tung University

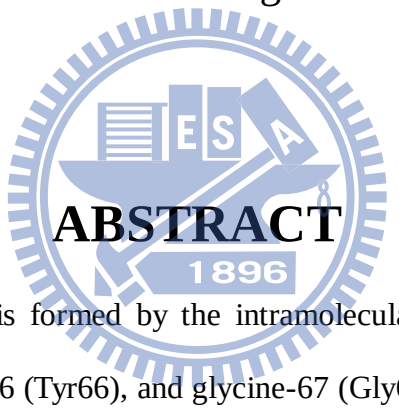

ABSTRACT

The GFP chromophore is formed by the intramolecular reaction from tripeptide serine-65 (Ser65), tyrosin-66 (Tyr66), and glycine-67 (Gly67) in the native protein for the primary structure while the chromophore in DsRed is also formed from the three amino acids which are glutamine-66 (Gln66), tyrosin-67 (Tyr67), and glycine-68 (Gly68) for the primary structure. Both the GFP and DsRed chromophores share the same 4-hydroxybenzylideneimidazolinone core, but the linkages at the imidazolinone ring are different. The extension of the conjugated Π-system in the chromophore may cause the significant red shift of the DsRed absorption properties compared to those of GFP.

In the present work, we demonstrate the absorption and fluorescence spectra of the GFP and DsRed chromophore in Franck-Condon simulation with including homogenous broadening, inhomogenous broadening, harmonic, and anharmonic

discussions. Three different exchange-correlation functionals (B3LYP, B3LYP-35, and BHandHLYP) of density functional theory (DFT) and Hartree-Fock (HF) method with and without the polarizable continuum model (PCM) were used for the ground state. At the same level of *ab initio* methods for the excited states, time-dependent density functional theory (TD-DFT) verse DFT and configuration interaction singles (CIS) verse HF, respectively.

The results presented in this study demonstrate that peak position and spectral widths of both absorption and fluorescence spectra for **HBDI** agree with experimental observations.

誌謝

兩年，在交大完成了碩士學位，一個人生旅途中的里程碑。

研究的過程雖然艱辛但成功的果實總是甜美。首先，萬分感謝朱超原老師以及林聖賢老師，給予我在研究上的指點迷津抑或是解決我在課業上的疑惑。感謝實驗室的琇雅學姊、哲源學長、孔哥令鈞、俊吉、李清旭學長、楊林學姊、李軍學長、宋迪學姊、雷依波學長、羅格非、易軍學姊、牛英利學長、莫燕學姊、孫廣旭、閻林胤、 Teranishi、Yamaki、美婷，給予我各方面的支持，讓這原本枯燥乏味的研究生活，增添了些許的色彩。感謝我的室友們–在睡夢中不忘研究的鎮廷、愛打球的虎牙哥富全、不離不棄是我兄弟的純情小綿羊哲豪，總在那夜深人靜時，想起那些一起度過的夜晚。感謝籃球社的籃球甜心璟妤社長、一起擊退硬課的偲丞、新任室友並肩作戰抵抗宅宅的岡岡、無私分享真的很黑的彥勳、很久沒來打球的小雞鈺芳、沒打過球卻很愛胸毛的小阿芳郁芳、以及一起打過球或是給予我幫助的各位學長同學們。

最後，感謝我的家人們，將這份榮耀與你們一起分享。

琮偉 謹誌

100 年 7 月 新竹交大

Table of Contents

List of Tables

List of Figures

Chapter 1　Introduction

In the 17th century, the invention of the microscope gave the way to observe cells, bacteria, and those things which we couldn't see apparently. In the middle of the 20th century, the discovery of the green fluorescent protein (GFP) leads into a new revolution and becomes one of the most widely studies. The rapid development of such useful tools which based on the GFP takes a great leap. Three scientists, Dr. Osamu Shimomura, Dr. Martin Chalfie and Dr. Roger Y. Tsien, were awarded the 2008 Nobel Prize in chemistry for the discovery and application of the GFP. The GFP makes a great impact in many areas and becomes a guide for biochemistry, biology, ecology, medicine, pharmacy and so on. Without a doubt, the more scientists know about its specifics, the greater they can develop.

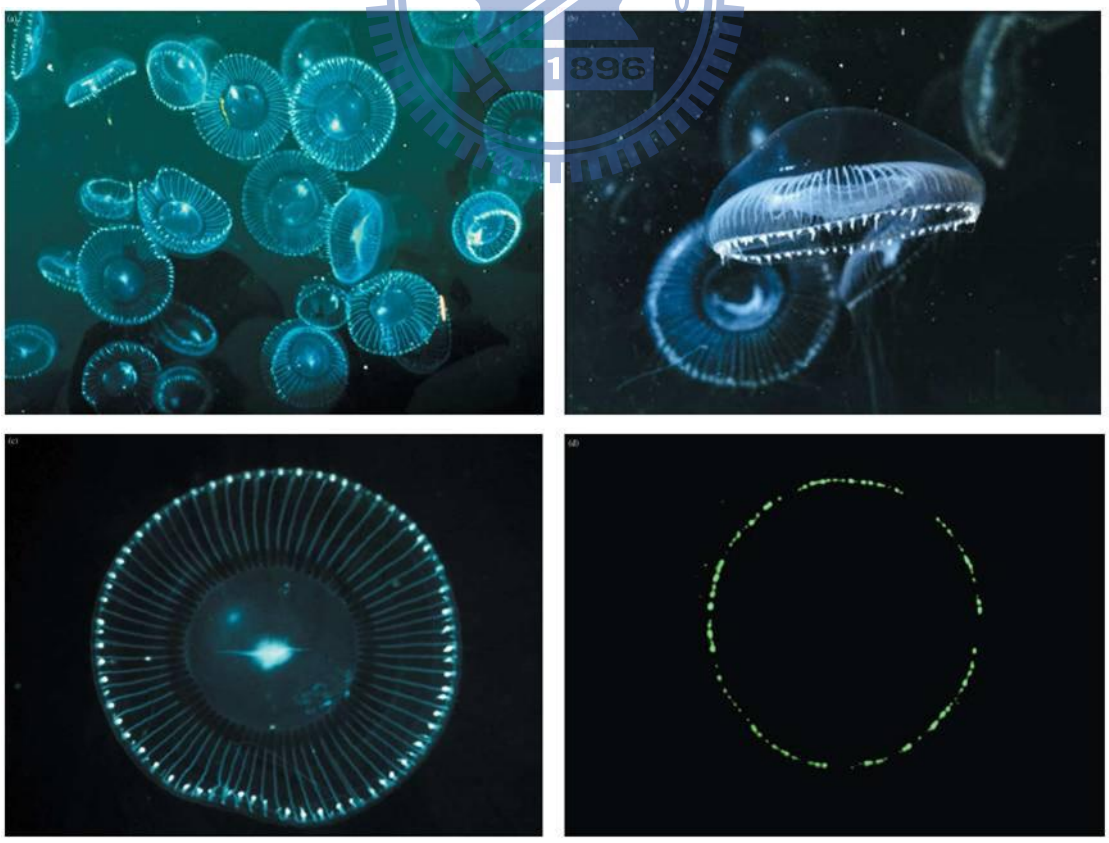

Fig. 1　The bioluminescent organ is located along the umbrella-like edge [1].

The GFP was first isolated from the jellyfish, *Aequorea victoria*, as a companion protein to *aequorin* by Shimomura and co-workers in the early 1960 [1, 2]. Dr. Osamu Shimomura tried to study these naturally luminescent materials and find out which part of the GFP was responsible for its fluorescence. His target was the luminescent substance, *aequorin*, and the GFP which is isolated as a by-product of aequorin with its bright conspicuous fluorescence [1]. These two luminescent substances are not only important but also widely used in the course of studies.

Fig. 1, the jellyfish, named *Aequorea victoria*, lives in the coast of the Northwest Pacific. Its outer edge of umbrella glows with the green light when it is disturbed. The pure *aequorin* is a blue luminescent material which is made from the jellyfish. They cut off the edge of the jellyfish and squeezed through rayon gauze. Then the turbid liquid was obtained which they called "squeezate" [1, 3]. They not only described the processes about how they obtained the *aequorin* but also remarked another protein with a bright green fluorescence in UV light named GFP. Now, after half century of their discovery, aequorin becomes a calcium probe and the GFP becomes a marker protein [1, 3].

$$\text{Aequorin} + Ca^{2+} \xrightarrow{\text{emit blue light}} \text{GFP} \xrightarrow{\text{emit green light}}$$

The seawater contains calcium ions (Ca^{2+}) that cause the *aequorin* emits blue light, even in the absence of oxygen. It stores a large amount of energy and releases the energy when calcium is added. The GFP absorbs the light of energy and then changes this energy into fluorescence. Because of the chromophore in the GFP, it transforms the blue light from *aequorin* into the green light [4].

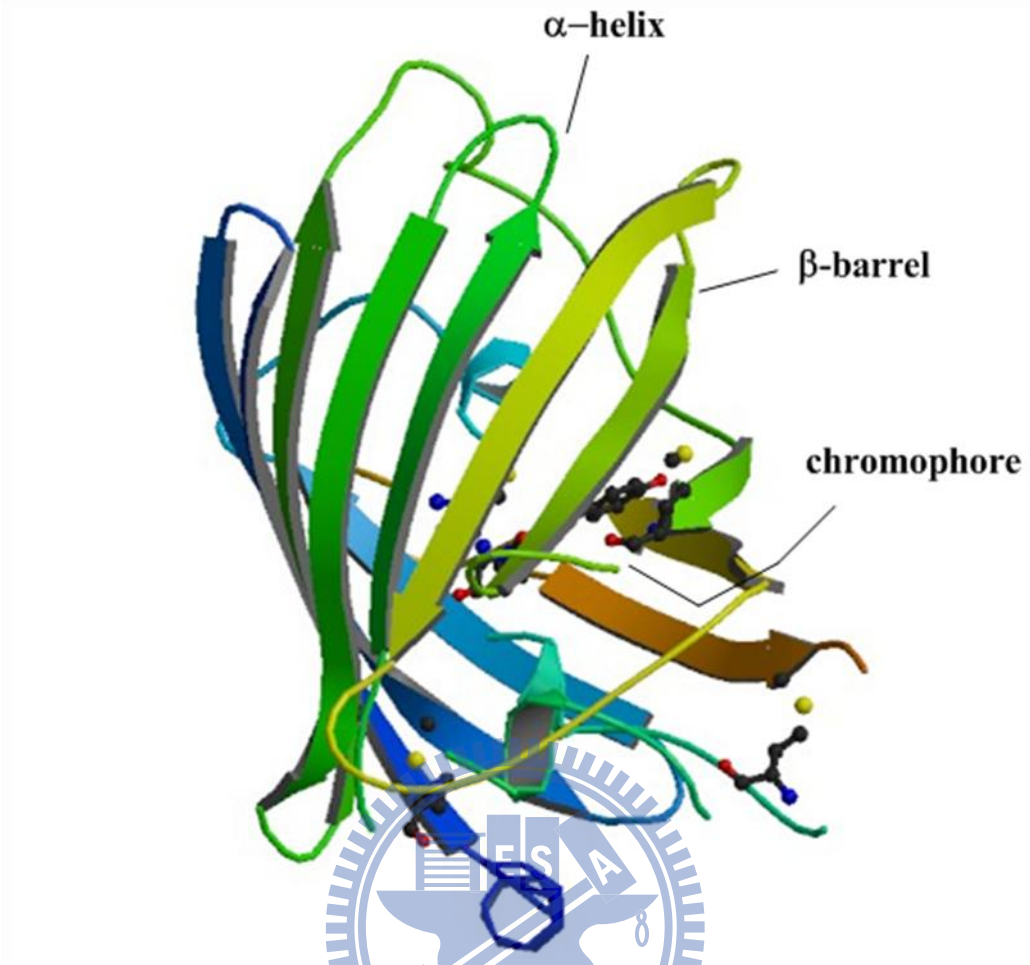

Fig. 2 The three-dimensional structure of the GFP which was first solved in 1996 independently by Ormö et al. (The figure were obtained from the Protein Data Bank (PDB) access code 1EMA.)

The GFP consists of 238 amino acids and its crystal structure is an 11-stranded *β*-barrel [5, 6]. The **Fig. 2** shows the first crystal structure until they have been reported for tens of years. The chromophore is derived from only a few important amino acids which are located near the center of the *β*-barrel. It is *p*-hydroxybenzylidene -imidazolinone (*p*-**HBDI,** see Scheme 1) formed from tripeptide serine-65 (Ser65), tyrosin-66 (Tyr66), and glycine-67 (Gly67) in the native protein for the primary structure [7-9].

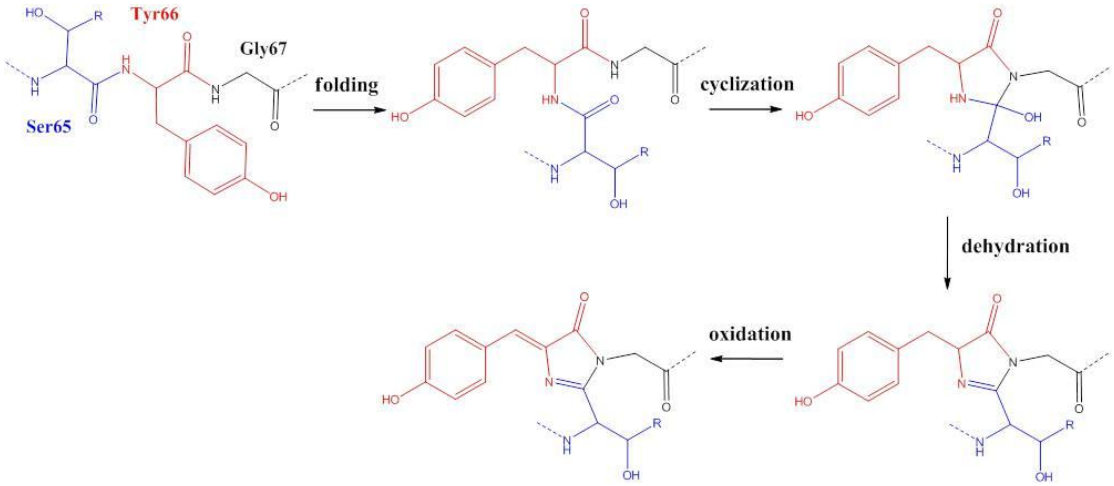

Fig. 3 The biosynthetic mechanism for the formation of the GFP chromophore.

Fig. 3 shows the mechanism begins by a nucleophilic attack of Gly67 on the carbonyl group of Ser65 to form a five-membered ring after the denatured GFP's folding. Then the reaction followed by loss of H_2O after the cyclization. The final step is the oxidation of the hydroxybenzyl side chain off Tyr66 [10].

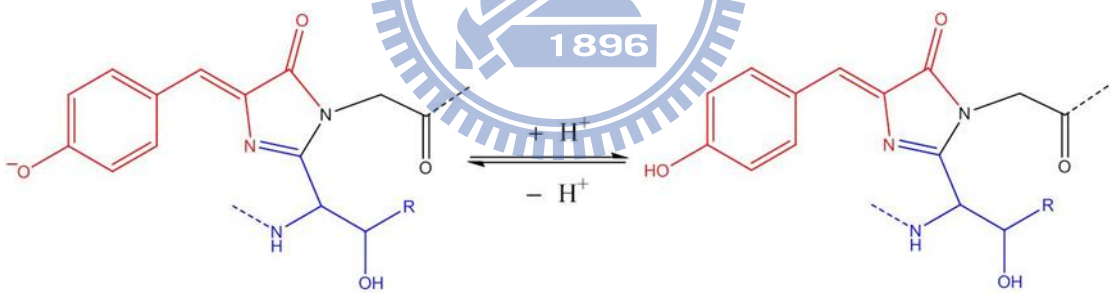

Fig. 4 Oxidation of Tyr66 leads into forming two fluorescent states – the neutral (protonated) and anionic (deprotonated) species.

The GFP variants may be divided into several classes based on the distinctive of their chromophores. There are wild-type mixture of neutral phenol, anionic phenolate, phenolate anion, and so on. The wild-type GFP (**wt-GFP**) has two characteristic absorption bands at room-temperature. One is a major excitation peak at 395 nm and another minor peak at 475 nm. When excitation is at about 395 nm that gives emission is at 508 nm [2, 9, 11]. **Fig. 4** represents the neutral and anionic forms which

may be responsible for the 395 nm and 475 nm excitation peaks, respectively. The equilibrium between these two forms is influence by external factors like temperature, PH, and the environment of the protein [6, 10]. The excited states of phenols are much more acidic than their ground states, so that the emission would occur only from the deprotonated species [9, 12].

Chattoraj and co-workers demonstrate that the neutral form can be converted to the anionic form by excited-state proton transfer. The room-temperature (298K) and 77K electronic absorption spectra of the GFP are much more different from Chattoraj's ultra-fast excited dynamic results [12-14].

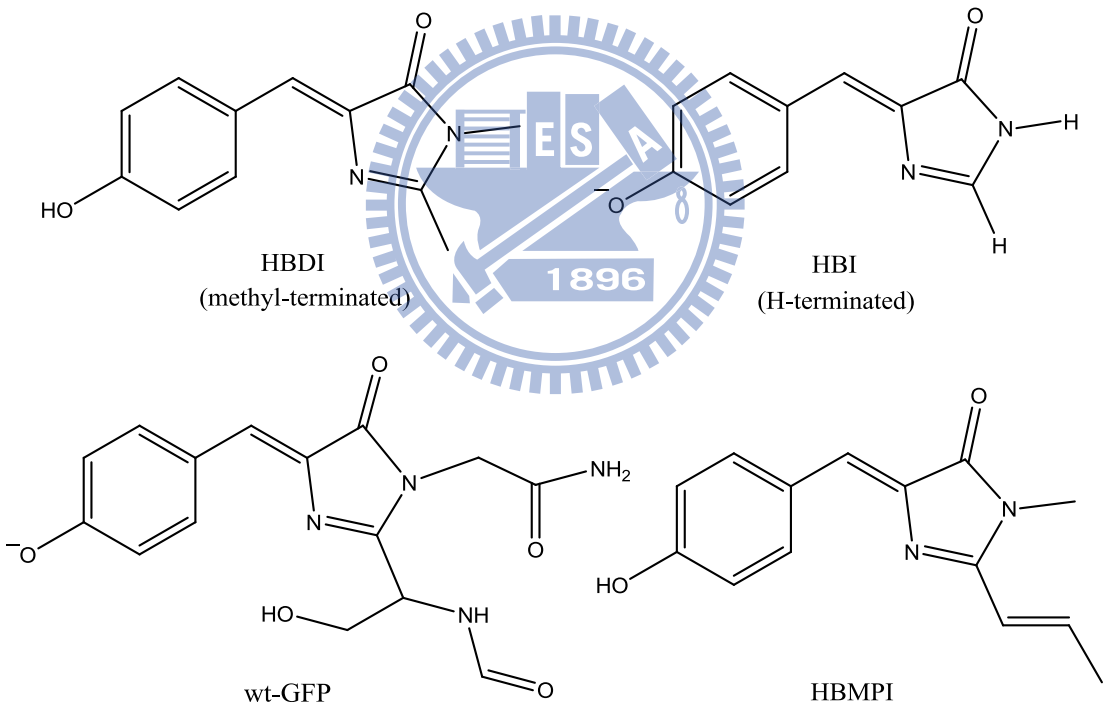

Scheme 1

Martin calculate the fluorescent path for the anionic **HBI** (Scheme 1) of the GFP by using the Complete Active Space Self-Consistent Field (CASSCF) level of theory with the 6-31G(d) basis set and the active space for 12 electrons in 11 orbitals [15].

Meech and co-workers study for the GFP and its mutants of the absorption and

emission spectra compared with the protein environment [16], ultrafast polarization spectroscopy for internal conversion process and excited-state-proton-transfer reaction [17, 18], temperature dependence and isoviscosity analysis for the internal conversion of the GFP chromophore [19].

DsRed is a recently cloned red fluorescent protein from Discosoma coralby the homology to the GFP. Like the formation of the GFP, the chromophore in DsRed is also formed by the intramolecular reaction of the three amino acids which is glutamine-66 (Gln66), tyrosin-67 (Tyr67), and glycine-68 (Gly68) (**HBMPI**, see Scheme 1)[20]. Both the GFP and DsRed chromophores share the same 4-hydroxybenzylidene-imidazolinone core, but they differ from the linkage at the imidazolinone ring. The more extended conjugated Π-system in the chromophore may cause the significant red shift of the DsRed absorption properties compared to those of GFP [21, 22].

In the present work, we investigate three GFP chromophore structures and one DsRed chromophore structure which are shown in scheme 1. There have been numerous studies for the equilibrium geometries of ground state and excited states. So we optimize the ground state, namely S_0 and the first-singlet-excited-state, namely S_1. First of all, discussions of the symmetry are very important. From the following theory which will demonstrate the principle for absorption and fluorescence spectra

Then, we compare the S_0 vibrational frequencies calculation with the experiments of Infrared (IR) spectra in order to demonstrate what the S_0 geometry is [23]. We would also compare the vibrational frequencies of S_0 with S_1. That means if the vibrational normal modes are similar in these two electronic states, the simulation of the absorption spectra could base on the displaced harmonic oscillator approximation [24]. Finally, we will simulate the absorption and fluorescence spectra using *ab initio* methods and also the solvent effects will be taken into account for the simulations.

Chapter 2 Theory

2.1 Density Functional Theory (DFT)

The first idea of describing the atomic and molecular systems as a functional of the electron density ρ(r) started with Thomas-Fermi model rather than the wavefunction [25]. In their quantum statistical model, a uniform electron gas, only the kinetic energy (the 1st term, T) was considered but it is a very coarse approximation to the true kinetic energy. The nuclear-electron (the 2nd term, E_{ne}) and electron-electron (the 3rd term, E_{ee}) contributions were treated as a classical way without any effects of exchange and correlation. The Thomas-Fermi energy expression is shown as

$$E_{TF}[\rho] = \frac{3}{10}\left(3\pi^2\right)^{2/3}\int \rho^{5/3}(\vec{r})d\vec{r} - Z\int \frac{\rho(\vec{r})}{r}d\vec{r} + \frac{1}{2}\iint \frac{\rho(\vec{r}_1)\rho(\vec{r}_2)}{r_{12}}d\vec{r}_1 d\vec{r}_2 \qquad (2.1)$$

Inclusion of the quantum mechanical exchange part for Eq. (2.1) is given the Thomas-Fermi-Dirac expression as

$$E_{TFD}[\rho] = E_{TF}[\rho] - \frac{3}{4}\left(\frac{3}{\pi}\right)^{1/3}\int \rho^{4/3}(\vec{r})d\vec{r} \qquad (2.2)$$

Unfortunately, the Thomas-Fermi-Dirac model does not achieve success in chemical applications just like the Thomas-Fermi model. But their points of view really play an important role for the development which is commonly called density functional theory (DFT).

The first Hohenberg-Kohn theorem states that the external potential V_{ext} (r) is (to within a constant) a unique functional of ρ(r) [26]. The ground state electronic energy is uniquely determined by the one-electron density. Thus, all the properties of the states are formally determined by the functional of the ground state electron density. The other Hohenberg-Kohn theorem states the functional that is satisfied with the

variational principle. It delivers the lowest energy for the ground state of the system only if the trial density is exactly the true ground state density. The simple equation can be expressed as [27]

$$\mathrm{E}[\tilde{\rho}] = \mathrm{T}[\tilde{\rho}] + \mathrm{E}_{\mathrm{ne}}[\tilde{\rho}] + \mathrm{E}_{\mathrm{ee}}[\tilde{\rho}] \geq \mathrm{E}_0[\rho_0] \tag{2.3}$$

The success of the DFT methods is based on the ingenious idea by Kohn and Sham in 1965 who is finding a better way for the determination of the kinetic energy [28]. Kohn realized that Hartree equation gave the better description for atomic ground states than Thomas-Fermi theory. The difference between these two theories is the treatment of the kinetic energy. Thus Kohn and Sham presented the concept of a non-interacting system moving under the influence of the effective external potential (V_{eff}, Eq.(2.4)) corresponding to the electron density. They suggested the Hartree Fock method and obtained the wavefunction of the exact kinetic energy in non-interacting system [29].

$$\mathrm{V}_{\mathrm{eff}}(\vec{r}) \equiv \mathrm{V}_{\mathrm{ext}}(\vec{r}) + \mathrm{V}(\vec{r}) + \mathrm{V}_{\mathrm{xc}}(\vec{r}) \tag{2.4}$$

$$\mathrm{T}_{\mathrm{S}} = -\frac{1}{2}\sum_{i}^{N}\langle\phi_i|\nabla^2|\phi_i\rangle \tag{2.5}$$

But this kind of expression is not equivalent to the true kinetic energy of non-interacting system. So they applied for exchange-correlation energy (E_{xc}) in the Kohn-Sham formulation. The ground state energy is given by

$$\begin{aligned}\mathrm{E}_{\mathrm{DFT}}[\rho] &= \mathrm{T}_{\mathrm{S}}[\rho] + \mathrm{E}_{\mathrm{ne}}[\rho] + \mathrm{J}[\rho] + \mathrm{E}_{\mathrm{xc}}[\rho] \\ &= -\frac{1}{2}\sum_{i}^{N}\langle\phi_i|\nabla^2|\phi_i\rangle + \int v_{\mathrm{ext}}(\vec{r})\rho(\vec{r})d\vec{r} + \frac{1}{2}\int\frac{\rho(\vec{r}_1)\rho(\vec{r}_2)}{r_{12}}d\vec{r}_1 d\vec{r}_2 \\ &\quad + \int e_{xc}(\vec{\mathrm{r}})\,\rho(\vec{\mathrm{r}})\mathrm{d}\vec{\mathrm{r}}\end{aligned} \tag{2.6}$$

$$\mathrm{E}_{\mathrm{xc}}[\rho] = (\mathrm{T}[\rho] - \mathrm{T}_{\mathrm{S}}[\rho]) + (\mathrm{E}_{ee}[\rho] - \mathrm{J}[\rho]) \equiv \int e_{xc}(\vec{\mathrm{r}})\rho(\vec{\mathrm{r}})\mathrm{d}\vec{\mathrm{r}} \tag{2.7}$$

where the e_{xc} term in Eq. (2.6) and (2.7) represents the exchange-correlation energy per particle. Besides, there are numerous approximations for E_{xc} in order to improve the accuracy.

The Local Density Approximation (LDA) is the simplest assumption that the density varies with the position slowly as the following equation [30, 31].

$$E_{xc}^{LDA}[\rho] = \int e_{xc}(\rho(\vec{r}))\,\rho(\vec{r})\,d\vec{r} \qquad (2.8)$$

where the e_{xc} term in Eq. (2.8) represents the exchange-correlation energy per particle of a uniform electron gas of the density. LDA gives the extremely useful results for other applications. The Local Spin-Density Approxition (LSDA) is the extension of LDA to the unrestricted system.

$$E_{xc}^{LSDA}[\rho_\alpha, \rho_\beta] = \int e_{xc}(\rho_\alpha(\vec{r}), \rho_\beta(\vec{r}))\,\rho(\vec{r})\,d\vec{r} \qquad (2.9)$$

Furthermore, in order to improve the accuracy of the non-uniform of the true electron density, the generalized gradient approximation (GGA) includes both electron density and its gradient of the density $\nabla(\vec{r})$. The expression can be simply defined as

$$E_{xc}^{GGA}[\rho_\alpha, \rho_\beta] = \int f(\rho_\alpha(\vec{r}), \rho_\beta(\vec{r}), \nabla\rho_\alpha(\vec{r}), \nabla\rho_\beta(\vec{r}))\,d\vec{r} \qquad (2.10)$$

When the extension takes higher order gradient of electron density into account, it is called meta-GGA method.

A number of hybrid functionals, which use the exact exchange energy is given by Hartree-Fock theory. This strategy performs accurate exchange-correlation energy. The most popular hybrid functional, B3LYP, expressed the exchange-correlation energy as [32]

$$E_{xc}^{B3LYP} = (1-a)E_x^{LSDA} + aE_x^{exact} + b\Delta E_x^{B88} + (1-c)E_c^{LSDA} + cE_c^{LYP} \qquad (2.11)$$

where a, b, and c are the semiemprical coefficients determined by fitting to

experimental data with values of 0.2, 0.72, and 0.81, respectively. For the B3LYP-35 functional, the values are 0.35, 0.585, and 0.81, respectively. For the BHandHLYP functional (Note that this is not the same as the "half-and-half" functional reported by Becke), the values are 0.5, 0.5, and 1, respectively. Much current work is still concerned about developing to improve the accurate exchange-correlation functionals.

The advantages of DFT, especially those involving gradient corrections and hybrid methods, have a significant improvement in the accuracy. However, DFT can be used to study larger molecules than other *ab initio* methods.

2.2 Time-Dependent Density Functional Theory (TD-DFT)

The successful treatment of DFT has inspired the theorists to develop many applications. However, the Hohenberg-Kohn-Sham formulation of DFT is time-independent treatment, thus it could not be demonstrated for arbitrary systems involving time-dependent problems such as molecular optics, absorption, fluorescence, nonradiative processes, and so on.

Therefore, time-dependent DFT (TD-DFT) is based on the Runge-Gross theorem just as DFT is based on Hohenberg-Kohn-Sham theorem [33, 34]. They specified an initial state $\Phi(t_0)$ at t = t_0 and density $n(\vec{r},t)$ obtained from a many-body system with Hamiltonian $\hat{H}$. They supposed the time-dependent Schrödinger equation of a many-body system can be solved.

$$\hat{H}(t) = \hat{T} + \hat{V}_{ext}(t) + \hat{V}_{ee} \qquad (2.12)$$

where $\hat{T}$ is the kinetic energy, $\hat{V}_{ext}(t)$ is the time-dependent potential, and the $\hat{V}_{ee}$ is the two-particle interaction. The time-dependent density is given as

$$n(\vec{r},t)=\langle\Phi(t)|\hat{n}(\vec{r})|\Phi(t)\rangle \tag{2.13}$$

with $\hat{n}(\vec{r})=\sum_s \hat{\psi}_s^{\ddagger}(\vec{r})\hat{\psi}_s(\vec{r})$, where s represents spin variable. At first, they demonstrated several important theorems before constructing the time-dependent Kohn-Sham Schrödinger equation.

The exact time-dependent density of the system can be computed from

$$\left[-\frac{1}{2}\nabla^2+V_{eff}(\vec{r},t)\right]\phi_j(\vec{r},t)=i\frac{\partial}{\partial t}\phi_j(\vec{r},t) \tag{2.14}$$

and

$$n(\vec{r},t)=\sum\phi_j^{\ddagger}(\vec{r},t)\phi_j(\vec{r},t) \tag{2.15}$$

where the exact density of the system can be obtained from single-particle orbitals $\phi_j(\vec{r},t)$ with one-particle potential $V_{eff}(\vec{r},t)$.

The hard work for time-dependent system is that it could not be based on the usual variational principle. Recently, due to the accuracy of the calculation, TD-DFT has replaced the single-excitation configuration interaction (CIS) which based on HF theory.

2.3 The Brief Polarizable Continuum Model (PCM) Method

So far, we only talk about the stationary-state quantum mechanics of an isolated molecule. But most of chemical reactions occur in the solutions that those solvents play an important role on the molecular properties like equilibrium structure, vibrational frequency, and so on.

For a continuum solvation model, the solvent generates a reaction field which is considered as a continuous dielectric and the solute is treated in a molecular cavity of realistic molecular shape. The interaction between the solute and the solvent may be

calculated by self-consistent reaction field method (SCRF) [35, 36].

Among several versions of polarizable continuum model (PCM) methods, integral equation formalism PCM (IEFPCM) method is a widely generalization of PCM applications for isotropic dielectrics, anisotropic dielectrics such as liquid crystals and polymers, and so on [37, 38].

2.4 Principles for Absorption and Fluorescence Spectra

In most molecular systems, the Born-Oppenheimer (B-O) approximation is very important for the theoretical treatment of molecular processes. The Franck-Condon overlap integrals of the two electronic states are essential for the vibronic structure of electronic spectra such as absorption spectra, fluorescence spectra, electronic transfer, and so on.

The quantum mechanical expression for the absorption coefficient is based on the time-dependent perturbation method and dipole approximation. The absorption coefficient for molecular systems in dense media can be expressed as [39]

$$\alpha(\omega)=\frac{4\pi^2\omega}{3a\hbar c}\left|\vec{\mu}_{ba}\right|^2\sum_{v}\sum_{v'}P_{av}\left|\left\langle\Theta_{bv'}\middle|\Theta_{av}\right\rangle\right|^2 \mathrm{D}\left(\omega_{bv',av}-\omega\right) \qquad (2.16)$$

where $\vec{\mu}_{ba}$ is the electronic transition dipole moment, P_{av} is the Boltzmann factor, $\left|\left\langle\Theta_{bv'}\middle|\Theta_{av}\right\rangle\right|^2$ represents the Franck-Condon factor , and the factor a is introduced to take into account the solvent effect. If the dephasing (or damping) effect is included, the Lorentzian lineshap function can be presented as the following relation.

$$\mathrm{D}\left(\omega_{bv',av}-\omega\right)=\frac{1}{\pi}\frac{\gamma_{ba}}{\left(\omega_{bv',av}-\omega\right)^2+\gamma_{ba}^2}=\frac{1}{2\pi}\int_{-\infty}^{\infty}dt e^{it\left(\omega_{bv',av}-\omega\right)-\gamma_{ba}|t|} \qquad (2.17)$$

$$\omega_{bv',av} = \omega_{ba} + \sum_j \left[\left(v' + \frac{1}{2} \right) \omega'_j - \left(v + \frac{1}{2} \right) \omega_j \right] \tag{2.18}$$

where r_{ba} is the so-called dephasing (or damping) constant. ω_{ba} denotes the electronic energy difference between the two electronic state a and b at the equilibrium geometry. The relation is presented as $\omega_{ba} = \frac{1}{\hbar}(E_b - E_a)$.

The wavefunction of harmonic oscillator is expanded into the product of each vibrational mode in Eq. (2.19) and Eq. (2.20). $\chi_{av_j}(Q_j)$ and $\chi_{bv'_j}(Q'_j)$ denote the vibrational wavefunctions of the *j*-th normal-mode for an initial electronic state a and a final electronic state b, respectively.

$$\Theta_{av}(Q) = \prod_j \chi_{av_j}(Q_j) \tag{2.19}$$

$$\Theta_{bv'}(Q') = \prod_j \chi_{bv'_j}(Q'_j) \tag{2.20}$$

where Q_j is mass weighted normal-mode coordinates including both intra- and intermolecular vibrations. Within displaced harmonic approximation, the previous absorption coefficient expression can be derived as

$$\alpha(\omega) = \frac{2\pi\omega}{3a\hbar c} \left| \vec{\mu}_{ba} \right|^2 \int_{-\infty}^{\infty} dt \exp\left[it(\omega_{ba} - \omega) - \gamma_{ba} |t| \right] \prod_j G_j(t) \tag{2.21}$$

And the time correlation function $G_j(t)$ is expressed as

$$G_j(t) = \sum_{v_j} \sum_{v'_j} P_{av_j} \left| \left\langle \chi_{bv'_j} \middle| \chi_{av_j} \right\rangle \right|^2 \exp\left[it\omega_j \left\{ \left(v'_j + \frac{1}{2} \right) - \left(v_j + \frac{1}{2} \right) \right\} \right] \tag{2.22}$$

After simplifying, $G_j(t)$ can be rewritten as

$$G_j(t) = \exp\left[-S_j \left\{ (2\bar{n}_j + 1) - (\bar{n}_j + 1) e^{it\omega_j} - \bar{n}_j e^{-it\omega_j} \right\} \right] \tag{2.23}$$

where $\bar{n}_j$ is the phonon distribution $\bar{n}_j = \left(e^{\hbar\omega_j / k_B T} - 1 \right)^{-1}$ and S_j is usually called the Huang-Rhys factor $S_j = \frac{\omega_j}{2\hbar} d_j^2$. In the Huang-Rhys factor expression, ω_j is the harmonic frequency of the *j*-th normal-mode and d_j is the displacement between the initial and final electronic state. The Huang-Rhys factors can give some information of spectra before the simulation. The Huang-Rhys factor $S_j < 1$ means weak coupling. On the other hand, $S_j >> 1$ means strong coupling.

Finally, the absorption coefficient of displaced harmonic oscillator is analytically derived as

$$\alpha(\omega) = \frac{2\pi\omega}{3a\hbar c} \left| \bar{\mu}_{ba} \right|^2 \int_{-\infty}^{\infty} dt \exp\left[it(\omega_{ba} - \omega) - \gamma_{ba} |t| - \sum_j S_j \left\{ (2\bar{n}_j + 1) - (\bar{n}_j + 1) e^{it\omega_j} - \bar{n}_j e^{-it\omega_j} \right\} \right] \quad (2.24)$$

For the cases of harmonic oscillator at T = 0 K, we can easily determine the Franck-Condon factor as Eq. (2.25).

$$\left| \left\langle \chi_{bv'_j} \middle| \chi_{a0_j} \right\rangle \right|^2 = \frac{S_j^{v'_j}}{v'_j!} e^{-S_j} \quad (2.25)$$

And the absorption coefficient is

$$\alpha(\omega) = \frac{2\pi\omega}{3a\hbar c} \left| \bar{\mu}_{ba} \right|^2 \int_{-\infty}^{\infty} dt \exp\left[it(\omega_{bv',a0} - \omega) - \gamma_{ba} |t| - \sum_j S_j \left(1 - e^{-it\omega_j} \right) \right] \quad (2.26)$$

where $\omega_{ba} = \frac{1}{\hbar}(E_b - E_a) > 0$.

For displaced harmonic oscillators, the absorption and fluorescence spectra show the mirror image relation which is due to the same transitions for invariant

Franck-Condon factor. The fluorescence coefficient is shown in Eq. (2.27).

$$I(\omega)=\frac{4\pi^2\omega}{3a\hbar c}\left|\bar{\mu}_{ba}\right|^2\sum_{v}\sum_{v'}P_{av}\left|\left\langle\Theta_{bv'}\middle|\Theta_{av}\right\rangle\right|^2 \mathrm{D}\left(\omega_{bv',av}+\omega\right) \qquad (2.27)$$

Following the similar procedures as above, then the fluorescence coefficient of displaced harmonic oscillator is analytically derived as

$$I(\omega)=\frac{2\pi\omega}{3a\hbar c}\left|\bar{\mu}_{ba}\right|^2\int_{-\infty}^{\infty}dt\exp\left[\ it\left(\omega_{ba}+\omega\right)-\gamma_{ba}|\,t|\right.$$
$$\left.-\sum_{j}S_j\left\{\left(2\bar{n}_j+1\right)-\left(\bar{n}_j+1\right)e^{it\omega_j}-\bar{n}_j e^{-it\omega_j}\right\}\right] \qquad (2.28)$$

where $\omega_{ba}=\frac{1}{\hbar}\left(E_b-E_a\right)<0$.

If the molecules are dissolved in the solvents, the solution environments are in disorder that caused the inhomogeneous phenomenon. For practical applications of solvent effect, the effects of inhomogeneity are taken into account. Suppose that the effects of inhomogeneity are associated with the electronic energy gap ω_{ba}. The Gaussian distribution function of inhomogeneities can be defined as

$$N\left(\omega_{ba}\right)=\frac{1}{\sqrt{\pi D_{ba}^2}}\exp\left[-\frac{\left(\omega_{ba}-\bar{\omega}_{ba}\right)^2}{D_{ba}^2}\right] \qquad (2.29)$$

where $\bar{\omega}_{ba}$ denotes the average energy gap and D_{ba} is the width of the distribution. Then

$$\left\langle e^{it\omega_{ba}}\right\rangle=\int_{-\infty}^{\infty}d\omega_{ba}N\left(\omega_{ba}\right)e^{it\omega_{ba}}=\exp\left(it\bar{\omega}_{ba}-\frac{D_{ba}^2t^2}{4}\right) \qquad (2.30)$$

Finally, the absorption coefficient of displaced harmonic oscillator with inhomogeneity is derived as

$$\langle\alpha(\omega)\rangle = \frac{2\pi\omega}{3a\hbar c}\left|\vec{\mu}_{ba}\right|^2 \int_{-\infty}^{\infty} dt \exp\left[it(\bar{\omega}_{ba}-\omega) - \frac{D_{ba}^2 t^2}{4} - \gamma_{ba}|t| - \sum_j S_j\left\{(2\bar{n}_j+1) - (\bar{n}_j+1)e^{it\omega_j} - \bar{n}_j e^{-it\omega_j}\right\}\right] \quad (2.31)$$

For the treatment of displaced anharmonic oscillator, the harmonic wavefunction will be utilized as a basis and the anharmonicity is considered as a perturbation [24]. Using the perturbation method to expand the *j*-th vibrational normal-mode potential as

$$V_j(Q) = a_{j2}Q_j^2 + \lambda a_{j3}Q_j^3 + \lambda^2 a_{j4}Q_j^4 + \cdots \quad (2.32)$$

in which λ is chosen as the perturbation parameter. The following presents the expansion of the wavefunction.

$$\chi_{v_j}(Q_j) = \chi_{v_j}^{(0)}(Q_j) + \lambda\chi_{v_j}^{(1)}(Q_j) + \lambda^2\chi_{v_j}^{(2)}(Q_j) + \cdots \quad (2.33)$$

where $\chi_{v_j}^{(0)}(Q_j)$ denote the zeroth-order harmonic wavefunction. The first-order correction to the wavefunction is

$$\chi_{vj}^{(1)}(Q_j) = -\frac{a_{j3}}{\hbar\omega_j}\left(\frac{\hbar}{2\omega_j}\right)^{3/2}\left\{3\left[\sqrt{(v_j+1)^3}\,\chi_{vj+1}^{(0)}(Q_j) - \sqrt{v_j^3}\,\chi_{vj-1}^{(0)}(Q_j)\right] + \frac{1}{3}\left[\sqrt{(v_j+1)(v_j+2)(v_j+3)}\,\chi_{vj+3}^{(0)}(Q_j) - \sqrt{v_j(v_j-1)(v_j-2)}\,\chi_{vj-3}^{(0)}(Q_j)\right]\right\} \quad (2.34)$$

We only consider the first-order anharmonic correction to the wavefunction which is based on the displaced harmonic oscillator. The second-order and the higher-order correction will be neglected due to the fewer contributions.

Finally, the absorption coefficient within the displaced anharmonic oscillator of the first-order correction is analytically derived as

$$\alpha(\omega)=\frac{2\pi\omega}{3a\hbar c}\left|\vec{\mu}_{ba}\right|^2\int_{-\infty}^{\infty}dt\exp\Bigg[\ it\left(\omega_{ba}-\omega+\Omega_0\right)-\gamma_{ba}\left|\ t\right|$$
$$-\sum_j S_j\left(1+3\eta_j\right)\left\{\left(2\bar{n}_j+1\right)-\left(\bar{n}_j+1\right)e^{it\omega_j}-\bar{n}_j e^{-it\omega_j}\right\}\Bigg] \tag{2.35}$$

where $\omega_{ba}=\frac{1}{\hbar}\left(E_b-E_a\right)>0$. And the fluorescence coefficient within the displaced anharmonic oscillator of the first-order correction is analytically derived as

$$I(\omega)=\frac{2\pi\omega}{3a\hbar c}\left|\vec{\mu}_{ba}\right|^2\int_{-\infty}^{\infty}dt\exp\Bigg[\ it\left(\omega_{ba}+\omega-\Omega_0\right)-\gamma_{ba}\left|\ t\right|$$
$$-\sum_j S_j\left(1+3\eta_j\right)\left\{\left(2\bar{n}_j+1\right)-\left(\bar{n}_j+1\right)e^{it\omega_j}-\bar{n}_j e^{-it\omega_j}\right\}\Bigg] \tag{2.36}$$

where $\omega_{ba}=\frac{1}{\hbar}\left(E_b-E_a\right)<0$. Ω_0 and η_j in the above equation represent the first-order anharmonic correction to the Franck-Condon factors. The expressions are given as

$$\Omega_0=-2\sum_j\eta_j S_j\omega_j \tag{2.37}$$

$$\eta_j=\frac{a_{j3}}{a_{j2}}d_j=\frac{\frac{\partial^3 V_j(Q)}{\partial Q_j^3}}{\frac{1}{2}\omega_j^2}d_j=\frac{\frac{1}{3}K_{j3}}{\frac{1}{2}\omega_j^2}d_j=\frac{2K_{j3}}{3\omega_j^2}d_j \tag{2.38}$$

Using the following relations

$$a_{j2}=\frac{1}{2}\omega_j^2 \tag{2.39}$$

$$a_{j3}=\frac{1}{3!}\frac{\partial^3 V_j(Q)}{\partial Q_j^3}=\frac{1}{3}K_{j3} \tag{2.40}$$

in which K_{j3} is the third derivative of the ground state potential energy surface

calculated by using GAUSSIAN 09 program package. Moreover, previously discussion has shown the displacement d_j in the Huang-Rhys factor $S_j = \frac{\omega_j}{2\hbar} d_j^2$. The detail is given by

$$d_j = Q'_j - Q_j = \sum_n L_{jn}\left(q'_n - q_n\right) \qquad (2.41)$$

where $q_n^{'}$ and q_n are mass-weighted Cartesian coordinates at the equilibrium geometries of the initial and final state, respectively. The transformation matrix L_{jn} also can be calculated by GAUSSIAN 09 program package.

Finally, the mirror image between the absorption and fluorescence spectra in displaced harmonic oscillator is broken down when the first-order anharmonic correction is taken into account. In other words, the Huang-Rhys factor is no longer invariant which is given as following.

$$S'_j = S_j\left(1 \pm 3\eta_j\right) \qquad (2.42)$$

where + is for absorption and – is for fluorescence.

Chapter 3 Computational Methods

All the calculations were carried out using GAUSSIAN 09 program package[40]. The equilibrium geometries belong to the C_S and C_1 symmetry. All 78 vibrational frequencies in **HBDI**, 57 vibrational frequencies in **HBI**, 111 vibrational frequencies in **wt-GFP**, and 87 vibrational frequencies in **HBMPI** were calculated by combining the use of Hartree-Fock (HF) and configuration interaction singles (CIS) with the 6-31+G(d) basis set for the ground (S_0) and first singlet excited (S_1) states, respectively. For comparison, three different DFT exchange-correlation functionals (B3LYP, B3LYP-35, and BHandHLYP) for S_0 with time dependent density functional theory (TD-DFT) for S_1 were also used with the same basis set. Besides, B3LYP, B3LYP-35, and BHandHLYP contain 20%, 35%, and 50% of HF exchanges, respectively. All the normal mode frequencies are multiplied by the scaling factors in HF and DFT with 6-31+G(d) basis set in order to improve the agreement between the experiments and the calculations. The sacling factors are 0.9614 for B3LYP/6-31+G(d), 0.94 for B3LYP-35/6-31+G(d), 0.92 for BHandHLYP/6-31+G(d), and 0.8970 for HF/6-31+G(d), respectively [41].

Furthermore, experimental and theoretical studies on the chromophore of GFP and its mutanis in various solvents have been reported numerously. In this study, the strategy is using PCM method to describe solvent effect on the properties of the ground and excited state geometries, absorption and fluorescence spectra, and so on. There have been published many PCM applications for recent year. It performs a self-consistent reaction field calculation for the interaction between the solute and the solvent. In this model, the solute is placed in a molecular cavity which is surrounded by the solvent.

In the present work, **HBDI** was considered in acetonitrile (CH_3CN, $\mathcal{E}$ = 35.69), methanol (CH_3OH, $\mathcal{E}$ = 32.61), and THF (C_4H_8O, $\mathcal{E}$ = 7.43) of the different dielectric constants ($\mathcal{E}$) for solvent effects. Anionic **HBI** was considered in acetonitrile (CH_3CN, $\mathcal{E}$ = 35.69), 1,2-ethanediol ($HOCH_2CH_2OH$, $\mathcal{E}$ = 40.245), and water (H_2O, $\mathcal{E}$ = 78.3553) for solvent effects. Anionic **HBMPI** was considered in acetonitrile (CH_3CN, $\mathcal{E}$ = 35.69), and water (H_2O, $\mathcal{E}$ = 78.3553) for solvent effects.

The vertical excitation energies were calculated by TD-DFT with three different DFT exchange-correlation functionals and CIS methods. In comparison, the vertical excitation energies with the semiempirical method Zerner's intermediate neglect of differential overlap (ZINDO) would also be utilized as a semiempirical approach. The combination of PCM and ZINDO is also applied for this study.

Based on the displaced oscillator which has been introduced previously, the vibrational normal modes between the two electronic states are the same. It means that the frequencies of the ground state and these two electronic structures should be calculated accurately.

Chapter 4 Results and Discussion

4.1 HBDI

4.1.1 Geometries of HBDI for C_S Symmetry

By using B3LYP/TD-B3LYP, and HF/CIS methods with 6-31+G(d) basis set optimized geometries in gas phase of the S_0 and S_1 states for **HBDI** are shown in **Fig. 5**. From the B3LYP/TD-B3LYP calculation, the bond lengths and angles in the S_0 phenol ring seem to have similar values to the S_1 phenol ring. Both the bridge bonds 4C−13C and 13C−15C have single−double bond character between S_0 and S_1 states. And the bridge angle 4C−13C−15C reduces from 130.1˚ to 129.8˚. In the imidazolidinone ring, it is quite obvious that the 16C−17N bonds and 17N−16C−20N angle expand by ca. 0.05 Å and 3˚ from S_0 to S_1, respectively. The differences in others are only about 0.03−0.04 Å for bond lengths and 0.1˚−1.5˚ for angles.

From the HF/CIS calculation, the bridge bonds still have single−double bond character but change larger than the B3LYP/TD-B3LYP calculation. The bridge angle reduces from 130.2˚ to 128.4˚ whose difference is much larger than the B3LYP/TD-B3LYP calculation.

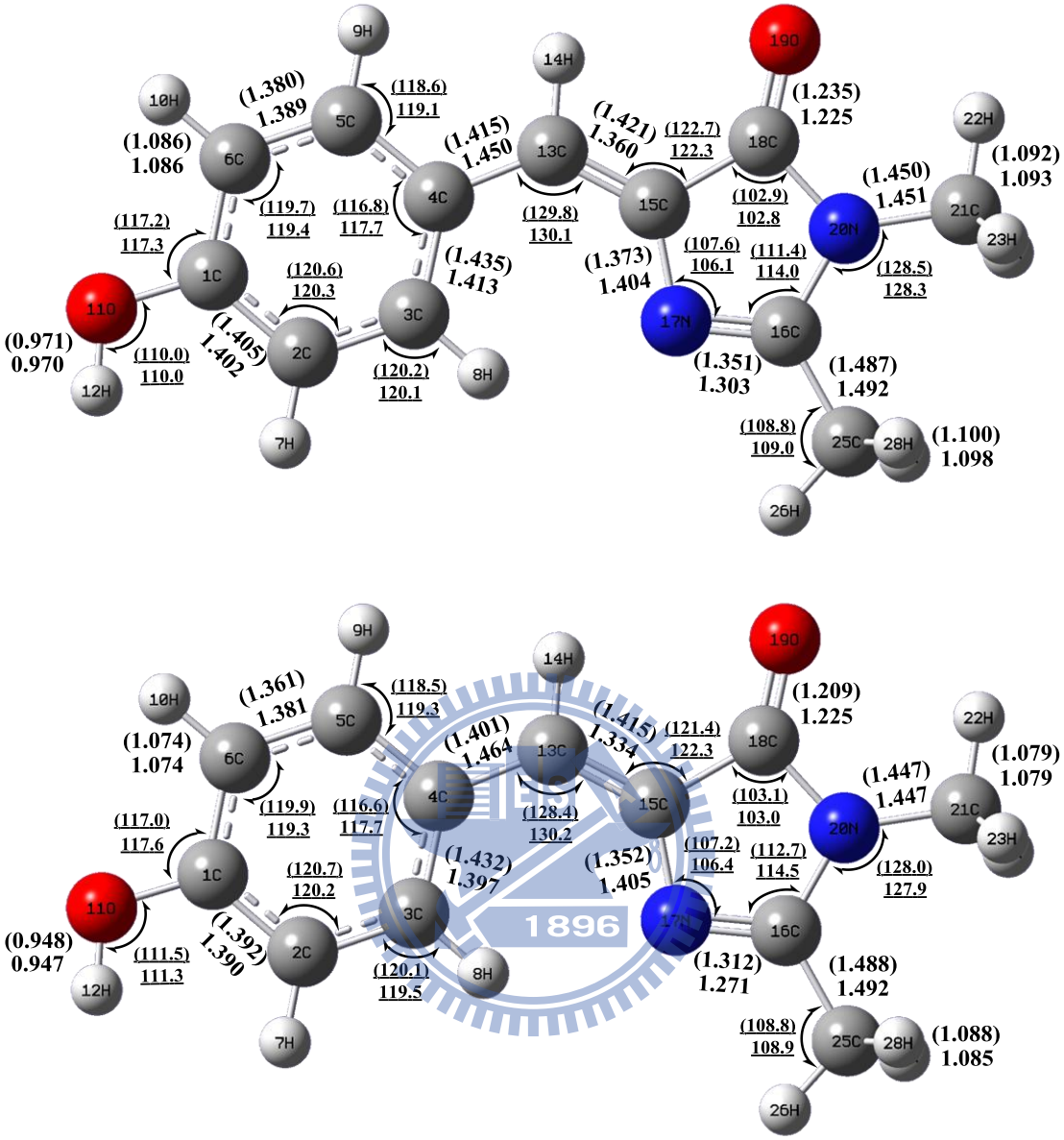

Fig. 5 Optimized geometries in gas phase of the C_s symmetry S_0 and S_1 states for **HBDI**. (Top) from B3LYP/6-31+G(d) and TD-B3LYP/6-31+G(d) calculations, (Bottom) from HF/6-31+G(d) and CIS/6-31+G(d) calculations. The bond lengths (bold, in angstrom) and angles (underline, in degree) of S_1 are provided in the brackets.

4.1.2 Vibrational Frequencies of HBDI for C_S Symmetry

From Ref. [23], the solid **HBDI** sample was ground with potassium bromide (KBr) and then pressed the mixture into a pellet by applying high pressure. KBr was chosen because it was transparent to infrared radiation. Therefore, the completely infrared spectrum of **HBDI** in 500 cm^{-1} ~ 1800 cm^{-1} region was shown in **Fig. 6(a)**. To facilitate description and contrast between the experiment and calculations, we only present the relative stick line for IR spectra.

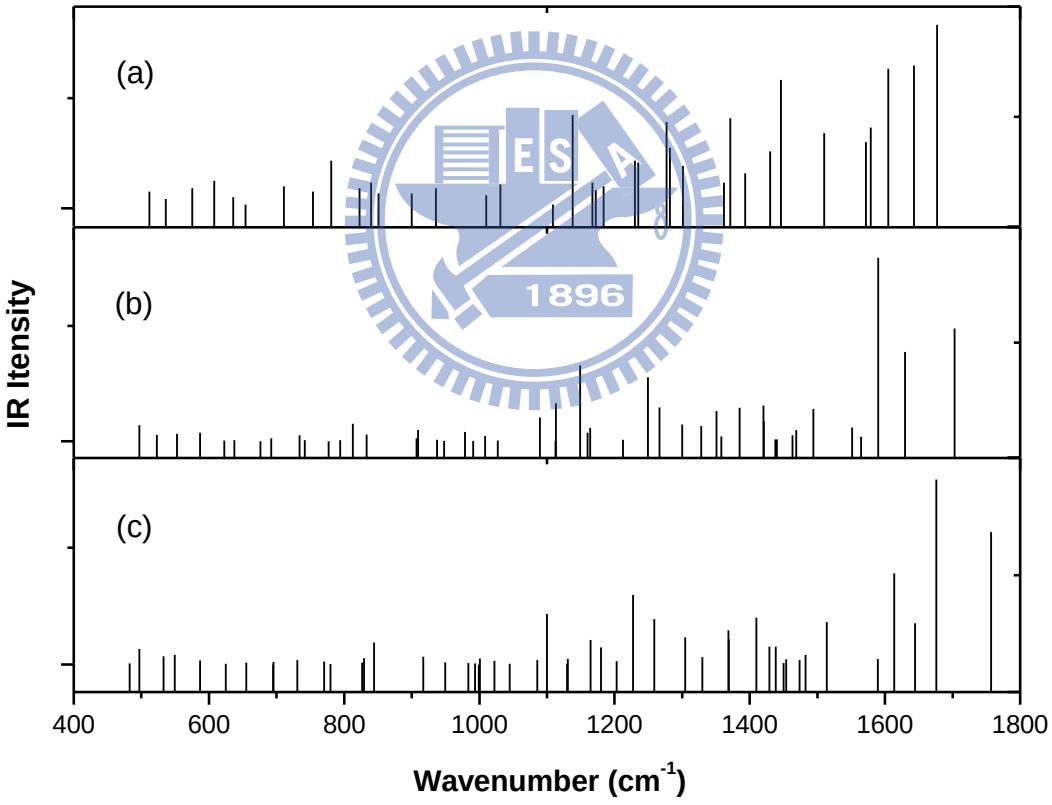

Fig. 6 Infrared spectra of **HBDI**. (a) experimental spectrum from Ref. [23], (b) B3LYP/6-31+G(d) calculation for C_S symmetry of the ground state, (c) HF/6-31+G(d) calculation for C_S symmetry of the ground state. The frequencies multiplied by scaling factor 0.9614 for B3LYP/6-31+G(d) method and 0.8970 for HF/6-31+G(d) method, respectively.

Comparison of **Fig. 6(a)** and **Fig. 6(b)** does not match very well. But several of the frequencies (1676, 1644, 1514, 1449, 1429, 1369, 1368, 1227 and so on) in HF calculation (**Fig. 6(c)**) are in agreement with the experimental frequencies (1677, 1643, 1510, 1446, 1430, 1371, 1227 and so on).

All 78 calculated vibrational frequencies of S_0 and S_1 states and its corresponding Huang-Rhys factors are listed in **Table 1** and **2.** The smallest vibrational mode (mode 78) shows one imaginary frequency (-62 cm^{-1}) for the equilibrium S_1 geometry in TD-B3LYP calculation but all 78 vibrational frequencies are positive in HF/CIS which means that S_0 and S_1 are exactly the local minima.

Table 1 Unscaled calculated vibrational frequencies of S_0 (ω_j, cm^{-1}) and S_1 (ω'_j, cm^{-1}) states with C_s symmetry using B3LYP/TD-B3LYP method. The corresponding Huang-Rhys factors (S^{HF}, dimensionless) are also shown.

Mode	ω_j	ω'_j	S^{HF}	Mode	ω_j	ω'_j	S^{HF}
1	3747	3739	0.95469	**40**	1049	1022	0.45854
2	3236	3232	0.16072	**41**	1030	1010	0.11546
3	3216	3212	0.34995	**42**	1018	963	1.38147
4	3186	3185	0.25431	**43**	986	962	0.00000
5	3169	3172	0.01968	**44**	975	948	0.00000
6	3167	3160	0.31834	**45**	946	884	0.17057
7	3162	3159	1.06606	**46**	943	858	0.00000
8	3155	3150	1.26823	**47**	867	824	0.14246
9	3109	3108	0.00000	**48**	846	812	0.00000
10	3094	3049	0.00000	**49**	826	796	0.00000
11	3051	3048	0.02744	**50**	808	792	0.26125
12	3045	3015	0.00151	**51**	772	759	0.00000
13	1771	1693	0.06125	**52**	764	715	0.18687
14	1695	1642	0.51706	**53**	720	702	2.70928
15	1654	1568	0.01402	**54**	703	679	0.00000
16	1627	1547	0.30278	**55**	663	638	0.00000
17	1614	1524	0.12235	**56**	648	590	0.33733
18	1554	1517	0.04000	**57**	610	557	0.00006
19	1528	1514	0.15366	**58**	575	509	1.54901
20	1522	1509	0.00000	**59**	544	499	0.00000
21	1498	1497	0.00000	**60**	517	497	0.82539
22	1496	1490	0.14501	**61**	495	419	0.00000
23	1478	1468	0.69057	**62**	418	412	0.00000
24	1477	1452	0.31373	**63**	417	377	0.00000
25	1441	1424	0.39645	**64**	374	338	0.00000
26	1412	1415	0.11362	**65**	360	326	0.00000
27	1405	1396	0.27239	**66**	336	308	1.96561
28	1382	1385	0.01140	**67**	276	269	0.02302
29	1352	1350	0.15225	**68**	247	242	0.07923
30	1318	1300	1.24547	**69**	233	221	0.00000
31	1300	1278	0.00176	**70**	205	206	0.25215
32	1261	1239	0.00026	**71**	203	189	0.00000
33	1211	1210	0.27173	**72**	171	127	0.00000
34	1206	1196	0.19168	**73**	143	116	0.00000
35	1195	1187	0.16189	**74**	107	79	0.00000
36	1158	1147	0.18563	**75**	94	74	0.00000
37	1158	1142	0.00000	**76**	79	70	0.29066
38	1133	1125	0.09344	**77**	52	46	0.00000
39	1068	1048	0.00000	**78**	46	-62	0.00000

Table 2 Unscaled calculated vibrational frequencies of S_0 (ω_j, cm^{-1}) and S_1 states (ω'_j, cm^{-1}) with C_s symmetry using HF/CIS method. The corresponding Huang-Rhys factors (S^{HF}, dimensionless) are also shown.

Mode	ω_j	ω'_j	S^{HF}	Mode	ω_j	ω'_j	S^{HF}
1	4110	4096	2.40735	**40**	1140	1116	-0.00175
2	3429	3430	1.35293	**41**	1116	1097	0.00265
3	3393	3393	-1.19557	**42**	1114	1090	0.00000
4	3366	3374	-0.82584	**43**	1108	1078	0.00229
5	3358	3366	-0.23372	**44**	1097	1055	0.00000
6	3344	3344	1.30622	**45**	1059	1010	0.00000
7	3343	3339	-1.07601	**46**	1023	948	0.00029
8	3330	3317	1.06513	**47**	941	898	0.00000
9	3283	3284	0.00000	**48**	925	886	0.00533
10	3267	3227	0.00000	**49**	921	877	0.00000
11	3225	3225	-0.67768	**50**	869	863	0.00037
12	3214	3186	0.64507	**51**	859	816	0.00000
13	1958	1883	0.14465	**52**	815	803	0.00178
14	1869	1797	-0.04141	**53**	775	776	-0.00175
15	1833	1712	-0.07836	**54**	775	742	0.00000
16	1799	1688	-0.02430	**55**	730	681	0.00000
17	1772	1667	-0.00664	**56**	696	667	0.00000
18	1688	1648	-0.00142	**57**	654	648	0.00182
19	1653	1641	-0.02354	**58**	612	625	-0.00033
20	1643	1634	0.00000	**59**	594	545	0.00000
21	1621	1627	0.00538	**60**	554	539	0.00015
22	1616	1609	0.00000	**61**	538	448	0.00000
23	1603	1595	0.00776	**62**	453	436	0.00000
24	1593	1576	0.00112	**63**	452	383	-0.00036
25	1572	1573	0.01325	**64**	398	374	0.00000
26	1526	1545	-0.00236	**65**	365	359	0.00033
27	1525	1531	-0.00116	**66**	340	334	0.00000
28	1483	1476	0.00103	**67**	304	297	-0.00026
29	1454	1436	0.00701	**68**	265	266	0.00000
30	1403	1426	-0.03297	**69**	247	262	0.00000
31	1369	1406	0.01219	**70**	220	212	-0.00005
32	1341	1365	0.00556	**71**	210	211	0.00000
33	1316	1316	0.00207	**72**	192	159	0.00000
34	1298	1285	0.00235	**73**	157	130	0.00000
35	1261	1273	0.00347	**74**	112	106	0.00000
36	1260	1257	0.00000	**75**	95	88	0.00000
37	1226	1256	0.00526	**76**	85	87	0.00000
38	1211	1217	0.00008	**77**	54	50	0.00000
39	1165	1146	0.00000	**78**	36	7	0.00000

4.1.3 Absorption Spectra of HBDI for C_S Symmetry

According to Ref. [42], the methanol, acetonitrile, and various methanol−water solutions at different pHs were used for the experiment at room temperature. In **Fig. 7(a)**, the absorption spectrum of *p*-**HBDI** from Ref. [42] exhibits an absorption maximum at 370 nm in methanol-water (1/1 vol). And the absorption spectra recorded in acetonitrile and methanol solvents are similar to those obtained for the neutral species in methanol−water solution. The similar results are also shown in Ref. [43] and the absorption maximum for *p*-**HBDI** varied between 365 nm and 378 nm in various solvents. Base on the references [42, 43], acetonitrile and methanol were considered for the simulation of absorption spestra with PCM method. The acetonitrile and methanol solvent are treated with a dielectric constant of 35.69 and 32.61, respectively.

The full width at half maximum (FWHM, Γ) are shown in **Fig. 7** for the experiment and calculations, respectively. The experimental maximum of absorption spectrum is at 370 nm (3.35eV) and the band's FWHM is about 4500 cm^{-1}. The homogeneous parameter, r_{ba}, are chosen as a small value in order to find out the Huang-Rhys factors. However, FWHM in **Fig. 7(b)** and **Fig. 7(c)** is quite four to six times larger than the experimental result in **Fig. 7(a)**.

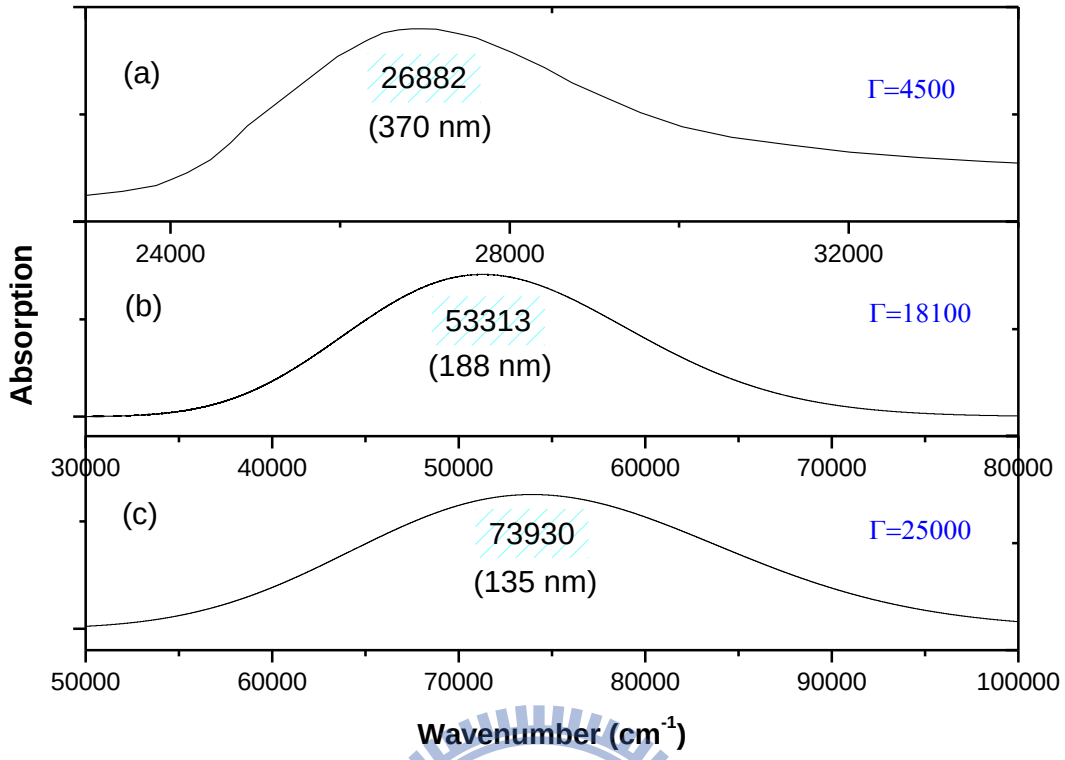

Fig. 7 Absorption spectra of **HBDI** at 298K. (a) experiment spectrum from Ref. [42], (b) simulated spectrum for r_{ba} = 0.1 cm^{-1} from B3LYP/TD-B3LYP calculation, (c) simulated spectrum for r_{ba} = 1 cm^{-1} from HF/CIS calculation.

Based on the displaced harmonic oscillator approximation, the absorption and fluorescence spectra will show the mirror image relation. So we do not need to simulate the fluorescence spectra. The most likely explanation for the broad width of the absorption spectra is that the equilibrium geometries of S_0 and S_1 states are not exactly correct. The results of C_S symmetry demonstrate that the geometries of S_0 and S_1 states must belong to the lower symmetry (also the lowest one) – C_1 point group.

4.1.4 Geometries of HBDI for C_1 Symmetry

After changing the point group into the C_1 symmetry, all the geometries were reoptimized using three different DFT exchange-correlation functionals (B3LYP/TD-B3LYP, B3LYP-35/TD-B3LYP-35, and BHandHLYP/TD-BHandHLYP), and HF/CIS methods with the same basis set. In this case, we also take the solvent effects into account by using B3LYP/TD-B3LYP with PCM method and inhomogeneous broadening approach in order to improve the simulated spectra.

First, comparison of **Fig. 8** (Top) and **Fig. 8** (Bottom) with results of C_S symmetry gives the surprising consequence of small changes for the bond lengths and angles. In fact, the larger differences between C_S and C_1 symmetry are the bridge angles, and the key point – dihedral angle of the two methyl groups connected to the imidazolidinone ring. The bridge angle 4C−13C−15C reduces from 130.1˚ to 128.3˚ for B3LYP/TD-B3LYP calculation but it is exactly the same value for HF/CIS calculation.

From **Table 3**, the dihedral angles of the two methyl groups are shown. 180.0000 and 0.0000 degree are exact for the ground and first singlet excited states of C_S symmetry. However, 22H-21C-20N-16C, 21C-20N-16C-25C, and 20N-16C-25C-26H no longer belong to horizontal mirror plane for B3LYP/TD-B3LYP and HF/CIS calculations. 0.0001 to 0.0037 differences of dihedral angles between C_S and C_1 symmetry seem very small but these slight changes are sufficient to cause not only the stable first singlet excited state but also the huge FWHM absorption spectra.

In TD-B3LYP calculation, the **HBDI** geometry is constrained by C_S symmetry that cause one imaginary frequency (-61.89 cm^{-1}) in the first singlet excited state but the same vibrational mode is not an imaginary frequency (30.81 cm^{-1}) anymore. Although

there is no imaginary frequency in CIS calculation, the corresponding mode is getting more stable from C_S (6.67 cm^{-1}) to C_1 (15.79 cm^{-1}) symmetry.

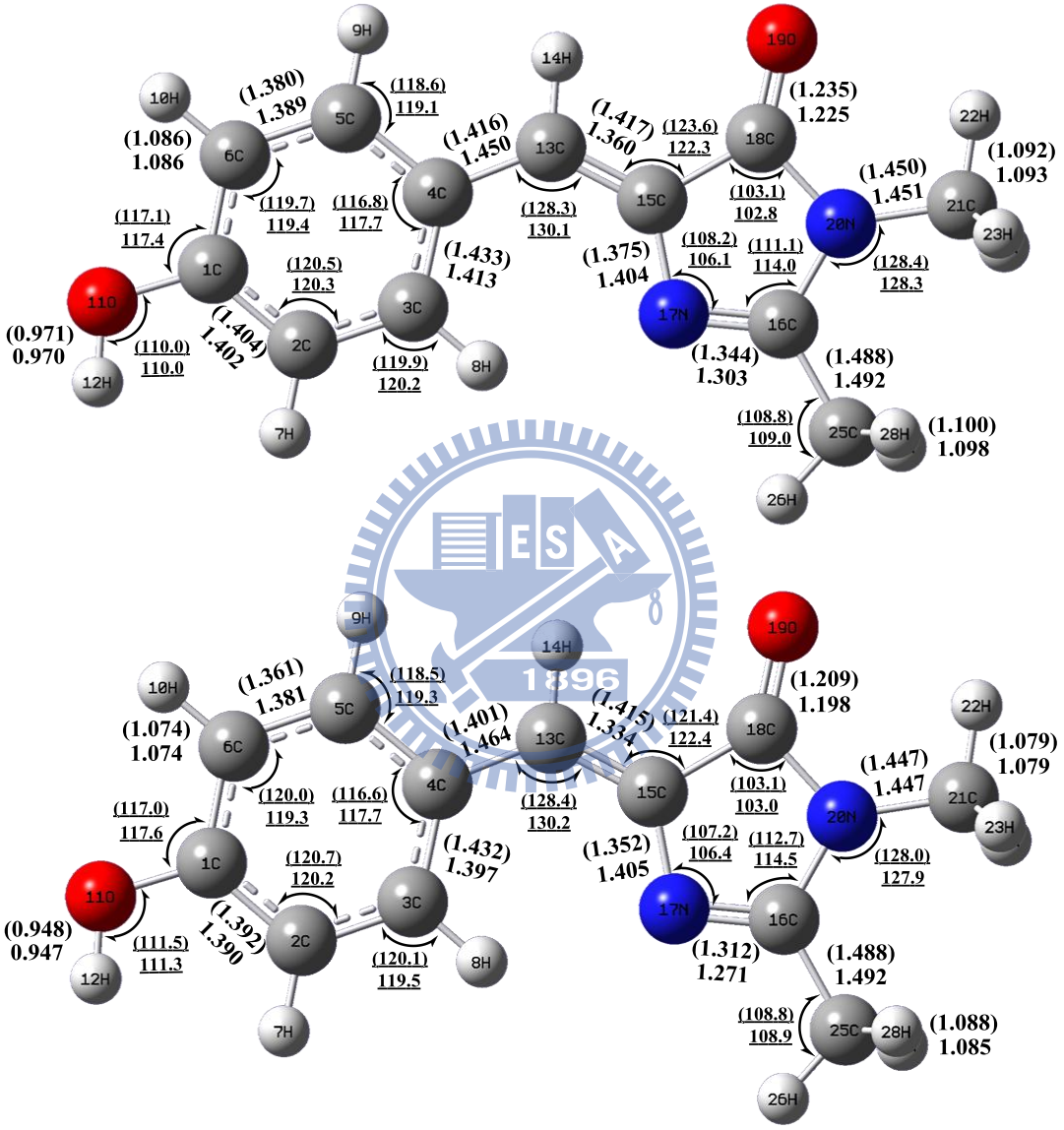

Fig. 8 Optimized geometries of the S_0 and S_1 states for **HBDI**. (Top) B3LYP/6-31+G(d) and TD-B3LYP/6-31+G(d) calculation (Bottom) HF/6-31+G(d) and CIS/6-31+G(d) calculation. The bond lengths (bold, in angstrom) and angles (underline, in degree) of S_1 are provided in the brackets.

Table 3 Important dihedral angles (in degree) of ground and first singlet excited states for C_S and C_1 symmetry.

	C_S[a]		C_1[b]		C_1[c]	
	S_0	**S_1**	**S_0**	**S_1**	**S_0**	**S_1**
22H-21C-20N-16C	180.0000	180.0000	180.0001	179.9998	179.9997	179.9974
21C-20N-16C-25C	0.0000	0.0000	0.0002	0.0002	0.0006	0.0037
20N-16C-25C-26H	180.0000	180.0000	180.0000	180.0000	179.9998	179.9990

[a]Both of B3LYP/TD-B3LYP and HF/CIS calculations.

[b]From B3LYP/TD-B3LYP calculation.

[c]From HF/CIS calculation.

Optimized geometries of the S_0 and S_1 states for **HBDI** in **Fig. 9** (Top), (Middle) and (Bottom) are considered H-bonding (methanol) and non H-bonding (acetonitrile and THF) solvents for PCM calculation. From the results of optimized geometry, all the structures are similar to each other in various solvent calculations.

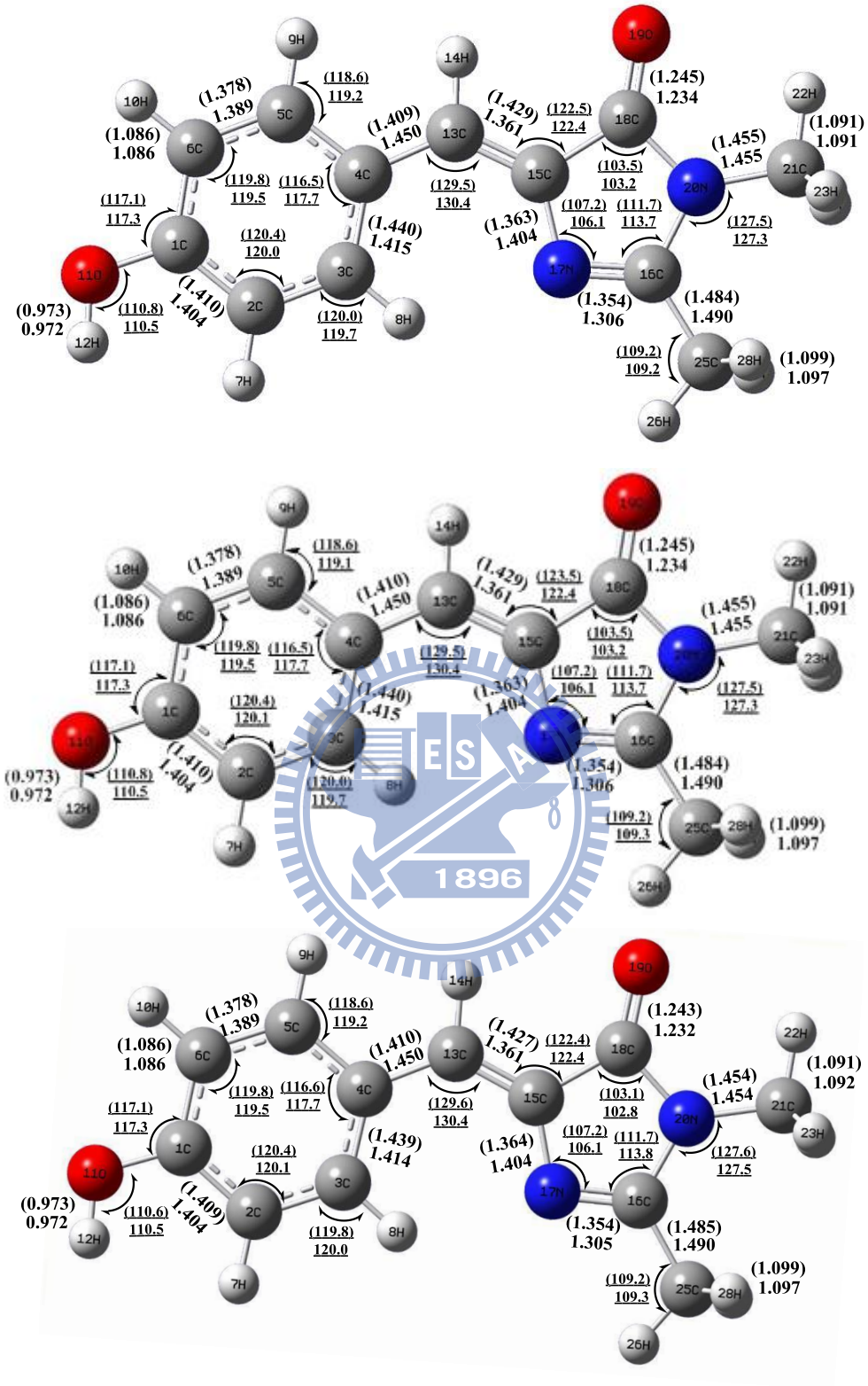

Fig. 9 B3LYP/6-31+G(d) and TD-B3LYP/6-31+G(d) optimized geometries of the S_0 and S_1 states for **HBDI**. (Top) acetonitrile solvent, (Middle) methanol solvent, and (Bottom) THF solvent for PCM calculations. The bond lengths (bold, in angstrom) and angles (underline, in degree) of S_1 are provided in the brackets.

The changes in gas phase calculation are consistent with other results reported by Helms et al and Polyakov et al [44, 45]. Actually, the C_S symmetry geometries also have similar values in the bond lengths and angles. But the quite larger divergence between the C_S and C_1 symmetry of the absorption or fluorescence spectra implies that C_S symmetry is not the correct point group, especially for the excited state. For comparison, the X-ray crystal structure determination of chromophore $C_{11}H_{10}N_2 \cdot H_2O$ (Scheme 2) is also shown in **Table 4**.

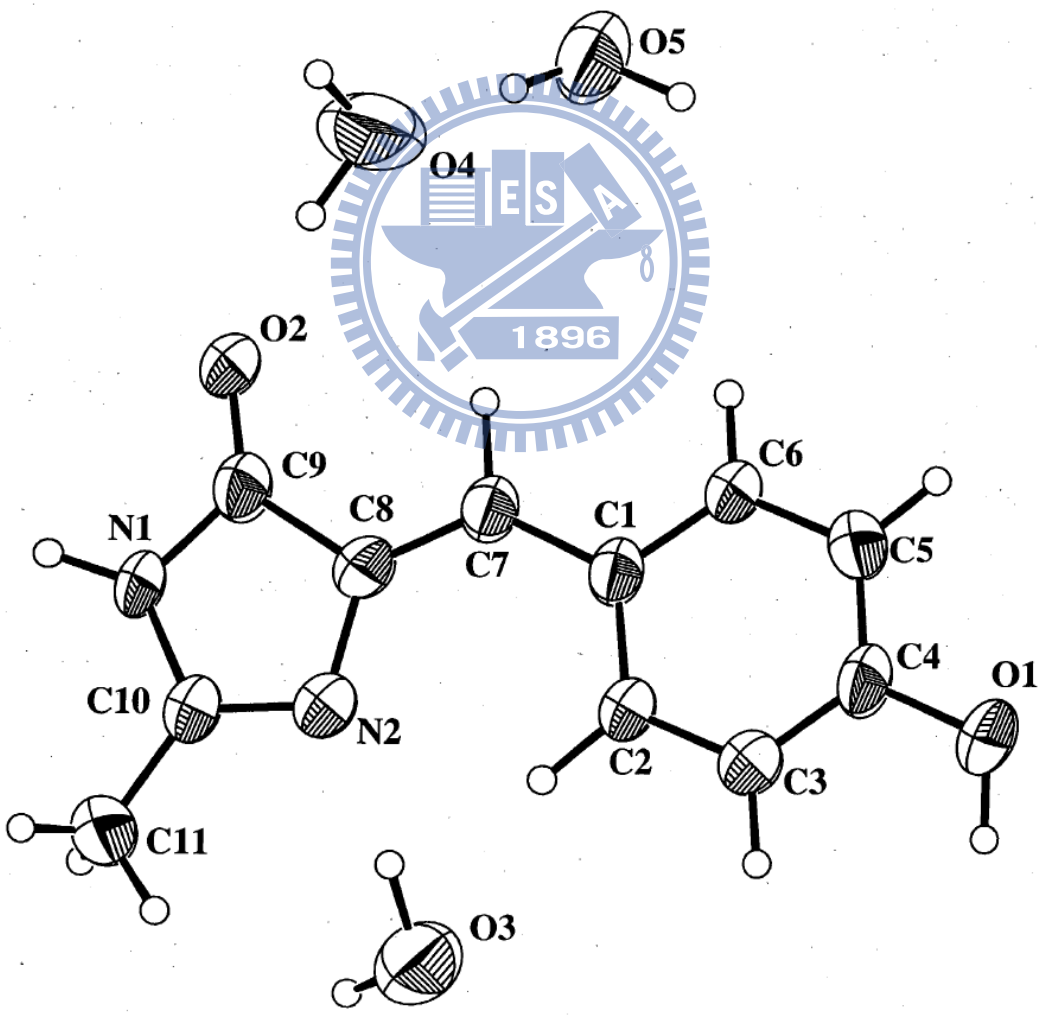

Scheme 2

Table 4 X-ray crystal structure from Ref. [46].

Bond (angstrom)		**Angle (degree)**		**Dihedral Angle (degree)**	
1C-2C	1.374	**2C-1C-6C**	120.8	**6C-1C-2C-3C**	0.7
1C-6C	1.379	**2C-1C-11O**	118.9	**11O-1C-2C-3C**	179.4
1C-11O	1.385	**6C-1C-11O**	120.2	**2C-1C-6C-5C**	-1.0
2C-3C	1.385	**1C-2C-3C**	120.2	**11O-1C-6C-5C**	-179.7
2C-7H	1.011	**1C-2C-7H**	120.3	**1C-2C-3C-4C**	0.3
3C-4C	1.394	**3C-2C-7H**	119.4	**2C-3C-4C-5C**	-1.0
3C-8H	1.088	**2C-3C-4C**	120.7	**2C-3C-4C-13C**	179.8
4C-5C	1.401	**2C-3C-8H**	117.3	**3C-4C5C-6C**	0.7
4C-13C	1.457	**4C-3C-8H**	121.8	**13C-4C-5C-6C**	179.9
5C-6C	1.375	**3C-4C-5C**	117.6	**3C-4C-13C-15C**	-2.7
5C-9H	0.999	**3C-4C-13C**	123.4	**5C-4C-13C-15C**	178.0
6C-10H	0.998	**5C-4C-13C**	119.0	**4C-5C-6C-1C**	0.3
11O-12H	1.010	**4C-5C-6C**	121.9	**4C-13C-15C-17N**	-1.2
13C-14H	1.080	**4C-5C-9H**	118.6	**4C-13C-15C-18C**	177.5
13C-15C	1.366	**6C-5C-9H**	119.5	**13C-15C-17N-16C**	177.6
15C-17N	1.418	**1C-6C-5C**	118.8	**18C-15C-17N-16C**	-1.2
15C-18C	1.476	**1C-6C-10H**	123.8	**13C-15C-18C-19O**	1.6
16C-17N	1.315	**5C-6C-10H**	117.4	**13C-15C-18C-20N**	-177.4
16C-20N	1.369	**1C-11O-12H**	109.5	**17N-15C-18C-19O**	-179.4
16C-25C	1.470	**4C-13C-14H**	121.4	**17N-15C-18C-20N**	1.5
18C-19O	1.227	**4C-13C-15C**	129.3	**20N-16C-17N-15C**	0.4
18C-20N	1.380	**14H-13C-15C**	109.3	**25C-16C-17N-15C**	179.7
25C-26H	0.975	**13C-15C-17N**	128.7	**17N-16C-20N-18C**	0.5
25C-27H	1.096	**13C-15C-18C**	122.5	**25C-16C-20N-18C**	-178.7
25C-28H	1.058	**17N-15C-18C**	108.8	**15C-18C-20N-16C**	-1.3
		17N-16C-20N	113.1	**19O-18C-20N-16C**	179.6
		17N-16C-25C	126.3		
		20N-16C-25C	120.6		
		15C-17N-16C	105.5		
		15C-18C-19O	131.0		
		15C-18C-20N	102.8		
		19O-18C-20N	126.1		
		16C-20N-18C	109.8		
		16C-25C-26H	111.1		
		16C-25C-27H	108.2		
		16C-25C-28H	100.7		
		26H-25C-27H	100.7		
		26H-25C-28H	102.0		
		27H-25C-28H	117.3		

4.1.5 Vibrational Frequencies of HBDI for C_1 Symmetry

IR spectra of three different DFT exchange-correction functionals and HF calculations are shown in **Fig. 10 (b)**, **(c)**, **(d)**, and **(e)**. Comparison each other to experimental IR spectrum, several of the frequencies (1676, 1644, 1514, 1450, 1438, 1368, 1228 and so on) in HF calculation (**Fig. 10(e)**) are still in agreement with the experimental frequencies (1677, 1643, 1510, 1446, 1430, 1371, 1227 and so on).

In general, DFT calculations only show the tendency toward the experimental IR spectrum. Frequencies (1702, 1630, 1494, 1384, and so on) in B3LYP calculation (**Fig. 10(b)**), frequencies (1716, 1640, 1495, 1386, and so on) in B3LYP-35 calculation (**Fig. 10(c)**), and frequencies (1722, 1644, 1493, 1384, and so on) in BHandHLYP calculation (**Fig. 10(d)**).

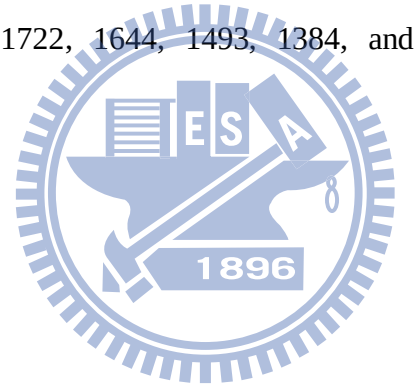

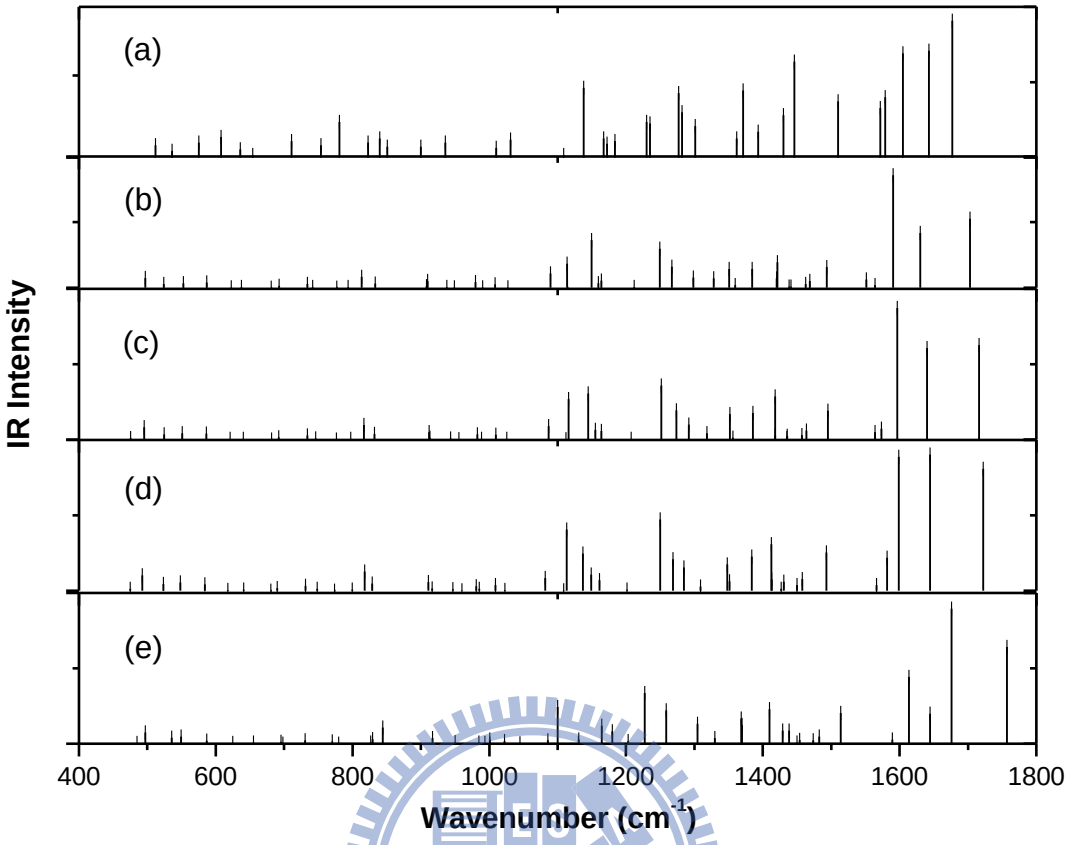

Fig. 10 Infrared spectra of **HBDI**. (a) experimental spectrum from Ref. [23], (b) B3LYP/6-31+G(d) method for C_1 symmetry of the ground state, (c) B3LYP-35/6-31+G(d) method for C_1 symmetry of the ground state, (d) BHandHLYP/6-31+G(d) method for C_1 symmetry of the ground state, (e) HF/6-31+G(d) method for C_1 symmetry of the ground state. The frequencies multiplied by scaling factor 0.9614 for B3LYP/6-31+G(d) method, 0.94 for B3LYP-35/6-31+G(d) method, 0.92 for B3LYP/6-31+G(d) method, and 0.8970 for HF/6-31+G(d) method, respectively.

In general, the frequencies of translation and rotation modes should be close to zero. But for methods which use numerical integration such as TD-DFT, the frequencies should be less than a few tens of wavenumbers. Take the positive vibrational frequency (30.8143 cm^{-1}) in **Table 5** for example, the first row of low frequencies is both translation and rotation modes and the second row of low frequencies is calculated after projecting out the translational and rotational modes (only show the least 3 of 78 modes here). If their corresponding frequencies in both places are not the same (30.8143 versus 30.8595), then this indicates that these modes are contaminated by the translational and rotational modes. And so is the imaginary mode. The energies of these two S_1 states are -724.37551705 hartree for S_1 with no imaginary frequency and -724.37513776 hartree for S_1 with one imaginary frequency. Its difference of energy is only 0.01 eV (83 cm^{-1}). Maybe changing the integration to ultrafine grid would modifies the calculation.

Table 5 Calculated low frequencies of translation and rotation modes for mode 78 by TD-B3LYP method.

Mode 78	**Low frequencies (cm^{-1})**					
30.8143	-7.6106	-1.1971	-0.1883	1.2035	2.5038	6.8283
	30.8595	46.5764	71.2027			
-63.0308	-63.0438	-1.5862	-0.3242	-0.0761	4.4524	4.9323
	9.9950	47.1977	66.4881			

All 78 calculated vibrational frequencies of S_0 and S_1 states and its corresponding Huang-Rhys factors are listed in **Table 6**, **7, 8, 9** and **10**. The smallest vibrational mode (mode 78) shows one imaginary frequency (-62 cm^{-1}) for the equilibrium S_1 geometry in TD-B3LYP calculation but all 78 vibrational frequencies are positive in B3LYP-35/TD-B3LYP-35, BHandHLYP/TD- BHandHLYP, and HF/CIS which means that S_0 and S_1 are exactly the local minima. Actually, there is one local minimum in TD-B3LYP calculation but the Huang-Rhys factors are a little too larger to simulate an agreeable absorption and fluorescence spectra. The followings serve as an example: S_j = 1.4312 for mode 9 (3109 cm^{-1}), S_j = 1.4092 for mode 10 (3093 cm^{-1}), S_j = 1.4434 for mode 16 (1627 cm^{-1}), S_j = 6.4333 for mode 49 (826 cm^{-1}), S_j = 1.5903 for mode 53 (720 cm^{-1}), S_j = 3.9507 for mode 77 (54 cm^{-1}). The simulations of the absorption and fluorescence spectra are given at next section.

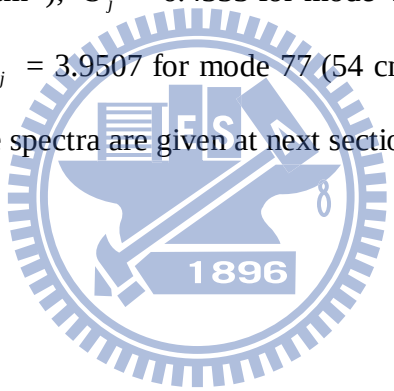

Table 6 Unscaled calculated vibrational frequencies of S_0 (ω_j, cm^{-1}) and S_1 (ω'_j, cm^{-1}) with C_1 symmetry using B3LYP/TD-B3LYP method. The corresponding Huang-Rhys factors (S^{HF}, dimensionless) and the 3rd derivative of S_0 potential energy surface (K_{j3}, Hartree*amu$^{-3/2}$*Bohr^{-3}) are also shown.

Mode	ω_j	ω'_j	S^{HF}	K_{j3}	Mode	ω_j	ω'_j	S^{HF}	K_{j3}
1	3748	3742	0.2147	-2.04537	**40**	1049	1011	0.2073	-0.00159
2	3237	3230	0.0298	-1.24536	**41**	1030	1010	0.0414	-0.00094
3	3216	3212	0.0176	1.12980	**42**	1019	964	1.0120	0.00368
4	3187	3186	0.0003	1.03862	**43**	987	962	0.3047	0.00000
5	3170	3171	0.2191	1.18020	**44**	975	934	0.6593	0.00000
6	3165	3160	0.0735	-1.20062	**45**	946	873	0.0065	-0.00015
7	3162	3160	0.2785	-1.00511	**46**	945	849	0.5149	0.00000
8	3154	3151	0.1630	0.92709	**47**	867	835	0.1118	-0.00491
9	3109	3113	1.4312	0.00000	**48**	846	801	0.0146	0.00000
10	3093	3055	1.4092	0.00009	**49**	826	799	6.4333	-0.00074
11	3051	3050	0.0286	0.60851	**50**	808	790	0.0114	0.00000
12	3044	3017	0.1153	-0.59719	**51**	771	758	0.0193	0.00204
13	1771	1672	0.0263	-0.12040	**52**	764	713	0.0081	0.00158
14	1696	1642	0.0082	-0.04534	**53**	720	697	1.5903	0.00000
15	1654	1574	0.2939	0.02405	**54**	708	685	0.9156	0.00000
16	1627	1537	1.4434	0.01737	**55**	663	640	0.2297	-0.00005
17	1614	1526	0.2785	-0.04384	**56**	648	595	0.4362	-0.00175
18	1554	1519	0.0223	-0.00171	**57**	610	573	0.0552	-0.00034
19	1527	1512	0.0063	0.02071	**58**	575	543	0.5403	0.00000
20	1521	1508	0.1561	0.00000	**59**	545	511	0.0154	0.00017
21	1499	1496	0.4949	0.00000	**60**	517	497	0.8508	0.00000
22	1496	1491	0.0372	0.00670	**61**	494	423	0.0555	0.00000
23	1478	1460	0.1794	0.00861	**62**	421	413	0.0253	0.00030
24	1478	1453	0.0031	0.00177	**63**	418	376	0.1096	0.00000
25	1440	1425	0.0204	-0.01455	**64**	375	372	0.1059	0.00000
26	1414	1405	0.0002	-0.00177	**65**	360	333	0.6610	0.00025
27	1405	1401	0.0153	0.00023	**66**	337	314	0.7588	0.00010
28	1382	1384	0.3049	0.00287	**67**	277	274	0.0188	0.00004
29	1351	1348	1.1624	0.00483	**68**	248	259	0.0039	0.00000
30	1318	1299	0.3249	-0.00867	**69**	234	240	1.0505	-0.00005
31	1300	1271	0.2182	-0.02845	**70**	206	215	0.0127	0.00000
32	1261	1227	0.3598	0.00674	**71**	203	186	0.2361	0.00000
33	1210	1199	0.0411	0.00056	**72**	170	148	0.6007	0.00000
34	1206	1188	0.0006	0.00144	**73**	145	115	0.1760	0.00000
35	1196	1181	0.3825	0.01233	**74**	107	107	0.4545	0.00000
36	1159	1147	1.1059	-0.00063	**75**	87	90	0.0272	0.00000
37	1159	1140	0.3246	-0.00290	**76**	80	71	0.9457	0.00000
38	1133	1121	0.0017	-0.00288	**77**	54	47	3.9507	0.00000
39	1069	1052	0.2143	0.00000	**78**	47	31	0.3744	0.00000

Table 7 Unscaled calculated vibrational frequencies of S_0 (ω_j, cm^{-1}) and S_1 (ω'_j, cm^{-1}) states with C_1 symmetry using B3LYP/TD-B3LYP method. The corresponding Huang-Rhys factors (S^{HF}, dimensionless) and the 3rd derivative of S_0 potential energy surface (K_{j3}, Hartree*amu$^{-3/2}$*Bohr^{-3}) are also shown. (One imaginary frequency!)

Mode	ω_j	ω'_j	S^{HF}	K_{j3}	Mode	ω_j	ω'_j	S^{HF}	K_{j3}
1	3748	3740	0.0660	-2.04537	**40**	1049	1023	0.1940	-0.00159
2	3237	3233	0.0000	-1.24536	**41**	1030	1010	0.0000	-0.00094
3	3216	3212	0.0072	1.12980	**42**	1019	962	0.1725	0.00368
4	3187	3186	0.0032	1.03862	**43**	987	962	0.0000	0.00000
5	3170	3173	0.0393	1.18020	**44**	975	948	0.0000	0.00000
6	3165	3158	0.0008	-1.20062	**45**	946	884	0.0449	-0.00015
7	3162	3158	0.0195	-1.00511	**46**	945	859	0.0000	0.00000
8	3154	3151	0.0007	0.92709	**47**	867	824	0.0035	-0.00491
9	3109	3108	0.0000	0.00000	**48**	846	813	0.0000	0.00000
10	3093	3049	0.0000	0.00009	**49**	826	795	0.0000	-0.00074
11	3051	3047	0.0016	0.60851	**50**	808	792	0.0006	0.00000
12	3044	3014	0.0012	-0.59719	**51**	771	759	0.0000	0.00204
13	1771	1694	0.0034	-0.12040	**52**	764	715	0.0002	0.00158
14	1696	1642	0.0069	-0.04534	**53**	720	702	0.4103	0.00000
15	1654	1568	0.0025	0.02405	**54**	708	679	0.0000	0.00000
16	1627	1548	0.2353	0.01737	**55**	663	639	0.0000	-0.00005
17	1614	1524	0.0579	-0.04384	**56**	648	591	0.0313	-0.00175
18	1554	1517	0.0133	-0.00171	**57**	610	557	0.0554	-0.00034
19	1527	1513	0.0030	0.02071	**58**	575	510	0.0510	0.00000
20	1521	1509	0.0000	0.00000	**59**	545	499	0.0000	0.00017
21	1499	1498	0.0000	0.00000	**60**	517	498	0.2034	0.00000
22	1496	1490	0.0001	0.00670	**61**	494	418	0.0000	0.00000
23	1478	1467	0.0048	0.00861	**62**	421	412	0.0000	0.00030
24	1478	1452	0.0218	0.00177	**63**	418	377	0.0308	0.00000
25	1440	1424	0.0609	-0.01455	**64**	375	337	0.0000	0.00000
26	1414	1415	0.0013	-0.00177	**65**	360	327	0.0000	0.00025
27	1405	1396	0.0332	0.00023	**66**	337	308	0.1240	0.00010
28	1382	1385	0.0646	0.00287	**67**	277	269	0.0709	0.00004
29	1351	1349	0.1352	0.00483	**68**	248	242	0.0001	0.00000
30	1318	1300	0.0007	-0.00867	**69**	234	222	0.0000	-0.00005
31	1300	1278	0.0002	-0.02845	**70**	206	205	0.0000	0.00000
32	1261	1239	0.1197	0.00674	**71**	203	190	0.0000	0.00000
33	1210	1210	0.0003	0.00056	**72**	170	122	0.0000	0.00000
34	1206	1195	0.0216	0.00144	**73**	145	110	0.0000	0.00000
35	1196	1188	0.0165	0.01233	**74**	107	80	0.0000	0.00000
36	1159	1147	0.0000	-0.00063	**75**	87	80	0.0000	0.00000
37	1159	1143	0.0555	-0.00290	**76**	80	66	0.0679	0.00000
38	1133	1125	0.0002	-0.00288	**77**	54	47	0.0000	0.00000
39	1069	1049	0.0000	0.00000	**78**	47	-63	0.0000	0.00000

Table 8 Unscaled calculated vibrational frequencies of S_0 (ω_j, cm^{-1}) and S_1 (ω'_j, cm^{-1}) states with C_1 symmetry using B3LYP-35/TD-B3LYP-35 method. The corresponding Huang-Rhys factors (S^{HF}, dimensionless) and the 3rd derivative of S_0 potential energy surface (K_{j3}, Hartree*$amu^{-3/2}$*$Bohr^{-3}$) are also shown.

Mode	ω_j	ω'_j	S^{HF}	K_{j3}	Mode	ω_j	ω'_j	S^{HF}	K_{j3}
1	3848	3838	0.1045	-2.14370	**40**	1074	1046	0.1390	-0.00150
2	3295	3289	0.0015	1.27860	**41**	1052	1029	0.0392	-0.00083
3	3272	3269	0.0068	-1.16007	**42**	1045	998	0.1994	-0.00283
4	3244	3245	0.0137	1.05377	**43**	1016	993	0.0000	0.00000
5	3228	3236	0.0585	1.19536	**44**	1003	975	0.0000	0.00000
6	3222	3216	0.0000	-1.23527	**45**	972	945	0.0000	0.00000
7	3218	3216	0.0305	-1.01939	**46**	970	875	0.0435	0.00008
8	3213	3205	0.0044	0.95400	**47**	885	852	0.0078	-0.00506
9	3166	3168	0.0000	0.00000	**48**	869	832	0.0000	0.00000
10	3151	3105	0.0000	0.00000	**49**	848	813	0.0000	0.00000
11	3105	3103	0.0009	-0.62520	**50**	826	813	0.0000	-0.00056
12	3099	3067	0.0000	0.60972	**51**	794	779	0.0000	0.00000
13	1826	1741	0.0006	-0.12762	**52**	781	733	0.0010	0.00207
14	1745	1685	0.0466	0.04715	**53**	736	730	0.3780	0.00151
15	1698	1602	0.0050	-0.02664	**54**	725	697	0.0000	0.00000
16	1674	1584	0.0037	0.03505	**55**	681	649	0.0000	0.00000
17	1664	1557	0.6718	-0.01832	**56**	661	609	0.0393	0.00000
18	1591	1551	0.0029	0.00198	**57**	624	592	0.0146	-0.00177
19	1557	1546	0.0016	-0.02138	**58**	586	567	0.0403	0.00035
20	1550	1545	0.0000	0.00000	**59**	558	519	0.0000	0.00000
21	1527	1533	0.0001	-0.00491	**60**	527	511	0.2400	-0.00017
22	1526	1517	0.0000	0.00000	**61**	506	425	0.0000	0.00000
23	1509	1498	0.0076	-0.00171	**62**	430	421	0.0000	0.00000
24	1509	1487	0.0070	-0.00815	**63**	427	386	0.0471	0.00032
25	1474	1468	0.0320	-0.01213	**64**	373	348	0.0000	0.00000
26	1443	1455	0.0143	-0.00116	**65**	365	336	0.0000	0.00000
27	1438	1448	0.0079	-0.00220	**66**	344	320	0.1547	-0.00026
28	1402	1410	0.1236	-0.00257	**67**	283	275	0.0594	0.00012
29	1374	1377	0.0484	0.00346	**68**	252	252	0.0000	-0.00004
30	1355	1336	0.2770	0.00717	**69**	238	247	0.0000	0.00000
31	1332	1309	0.0002	0.03085	**70**	210	207	0.0218	0.00005
32	1285	1284	0.1701	-0.00705	**71**	206	196	0.0000	0.00000
33	1238	1241	0.0147	-0.00015	**72**	175	144	0.0000	0.00000
34	1229	1218	0.0143	-0.00210	**73**	148	112	0.0000	0.00000
35	1218	1210	0.0774	-0.01422	**74**	108	92	0.0000	0.00000
36	1187	1192	0.0393	-0.00286	**75**	87	82	0.0000	0.00000
37	1183	1175	0.0000	0.00000	**76**	82	78	0.1356	0.00000
38	1156	1153	0.0011	0.00304	**77**	54	49	0.0000	0.00000
39	1091	1070	0.0000	0.00000	**78**	46	18	0.0000	0.00000

Table 9 Unscaled calculated vibrational frequencies of S_0 (ω_j, cm^{-1}) and S_1 (ω'_j, cm^{-1}) states with C_1 symmetry using BHandHLYP/TD-BHandHLYP method. The corresponding Huang-Rhys factors (S^{HF}, dimensionless) and the 3rd derivative of S_0 potential energy surface (K_{j3}, Hartree*$amu^{-3/2}$*$Bohr^{-3}$) are also shown.

Mode	ω_j	ω'_j	S^{HF}	K_{j3}	Mode	ω_j	ω'_j	S^{HF}	K_{j3}
1	3931	3919	0.1732	-2.22784	**40**	1097	1068	0.0461	-0.00157
2	3344	3339	0.1265	1.30722	**41**	1071	1046	0.0038	-0.00051
3	3320	3317	0.0681	-1.18377	**42**	1066	1033	0.0430	-0.00214
4	3291	3294	0.2019	1.05418	**43**	1043	1020	0.0000	0.00000
5	3277	3287	0.0569	1.19286	**44**	1029	1000	0.0000	0.00000
6	3270	3265	0.0321	-1.26500	**45**	996	975	0.0000	0.00000
7	3264	3264	0.1461	-1.02704	**46**	990	894	0.0176	0.00016
8	3261	3251	0.0005	0.97233	**47**	901	869	0.1357	-0.00518
9	3213	3216	0.0000	-0.00010	**48**	889	851	0.0000	0.00000
10	3198	3152	0.0000	0.00000	**49**	869	831	0.0000	0.00000
11	3151	3152	0.0007	0.64221	**50**	841	831	0.0388	-0.00042
12	3144	3113	0.0034	0.62510	**51**	813	794	0.0000	0.00000
13	1872	1787	0.0029	-0.13325	**52**	795	751	0.0561	0.00209
14	1787	1721	0.0214	0.04797	**53**	750	747	0.5598	0.00145
15	1738	1632	0.1357	0.03255	**54**	740	712	0.0000	0.00000
16	1719	1625	0.0128	0.02820	**55**	696	659	0.0000	0.00000
17	1703	1587	0.4736	-0.00283	**56**	672	625	0.7725	0.00000
18	1623	1583	0.0001	0.00208	**57**	635	606	0.0639	-0.00179
19	1584	1577	0.0006	0.02192	**58**	596	605	0.1214	0.00036
20	1576	1572	0.0000	0.00000	**59**	569	527	0.0000	0.00000
21	1555	1563	0.0041	-0.00301	**60**	535	522	0.2184	-0.00017
22	1551	1542	0.0000	0.00000	**61**	516	433	0.0000	0.00000
23	1536	1526	0.0033	-0.00171	**62**	439	429	0.0000	0.00000
24	1535	1518	0.0004	-0.00830	**63**	434	389	0.0013	0.00034
25	1504	1505	0.1351	-0.01137	**64**	380	361	0.0000	0.00000
26	1469	1489	0.2073	0.00383	**65**	361	343	0.0000	0.00000
27	1465	1473	0.0180	0.00164	**66**	349	326	0.0048	-0.00027
28	1422	1430	0.0343	-0.00241	**67**	288	280	0.0000	0.00014
29	1396	1403	0.2359	-0.00273	**68**	256	262	0.0180	-0.00004
30	1379	1366	0.0247	0.00462	**69**	242	251	0.0000	0.00000
31	1358	1344	0.0004	0.03227	**70**	213	208	0.0008	0.00005
32	1306	1318	0.0361	-0.00683	**71**	207	200	0.0000	0.00000
33	1262	1265	0.0111	0.00000	**72**	179	152	0.0000	0.00000
34	1249	1238	0.0980	-0.00224	**73**	151	115	0.0000	0.00000
35	1236	1228	0.0496	-0.01445	**74**	110	98	0.0000	0.00000
36	1210	1224	0.1093	-0.00234	**75**	89	85	0.0000	0.00000
37	1205	1199	0.0000	0.00000	**76**	83	79	0.0000	0.00000
38	1176	1174	0.0020	0.00319	**77**	54	51	0.0000	0.00000
39	1112	1090	0.0000	0.00000	**78**	45	23	0.0000	0.00000

Table 10 Unscaled calculated vibrational frequencies of the S_0 (ω_j, cm^{-1}) and S_1 (ω'_j, cm^{-1}) states with C_1 symmetry using HF/CIS method. The corresponding Huang-Rhys factors (S^{HF}, dimensionless) and the 3rd derivative of S_0 potential energy surface (K_{j3}, Hartree*amu$^{-3/2}$*Bohr^{-3}) are also shown.

Mode	ω_j	ω'_j	S^{HF}	K_{j3}	Mode	ω_j	ω'_j	S^{HF}	K_{j3}
1	4110	4096	0.1608	-2.40741	**40**	1140	1116	0.1029	0.00175
2	3430	3430	0.0136	1.35309	**41**	1116	1097	0.1354	-0.00265
3	3393	3393	0.0058	-1.19402	**42**	1115	1091	0.0000	0.00000
4	3366	3374	0.0955	0.82380	**43**	1108	1078	0.0529	-0.00229
5	3358	3366	0.0196	0.25561	**44**	1098	1057	0.0000	0.00000
6	3344	3344	0.0001	-1.30635	**45**	1059	1010	0.0000	0.00000
7	3343	3339	0.0038	1.07640	**46**	1023	951	0.0434	-0.00029
8	3330	3317	0.0560	-1.06513	**47**	941	899	0.0000	0.00000
9	3283	3284	0.0000	0.00000	**48**	925	886	0.0211	-0.00533
10	3267	3227	0.0000	0.00000	**49**	921	879	0.0000	0.00000
11	3225	3225	0.0000	0.67842	**50**	869	863	0.0107	-0.00037
12	3214	3186	0.0026	0.64612	**51**	859	816	0.0000	0.00000
13	1958	1883	0.0041	-0.14468	**52**	814	804	0.0002	-0.00178
14	1869	1797	0.1294	0.04134	**53**	778	776	0.0000	0.00000
15	1833	1712	0.0071	0.07833	**54**	775	747	0.3168	0.00175
16	1799	1688	0.0236	0.02430	**55**	731	682	0.0000	0.00000
17	1772	1667	1.2981	0.00661	**56**	696	668	0.0685	0.00000
18	1688	1648	0.0050	0.00142	**57**	654	648	0.0005	-0.00182
19	1653	1641	0.0006	0.02353	**58**	612	625	0.0306	0.00033
20	1643	1634	0.0000	0.00000	**59**	597	545	0.0000	0.00000
21	1621	1627	0.0006	-0.00536	**60**	554	544	0.3082	-0.00015
22	1616	1609	0.0000	0.00000	**61**	540	450	0.0000	0.00000
23	1603	1595	0.0106	-0.00777	**62**	459	448	0.0000	0.00000
24	1593	1576	0.0126	-0.00112	**63**	452	383	0.0720	0.00036
25	1572	1573	0.0165	-0.01324	**64**	398	382	0.0000	0.00000
26	1527	1545	0.0028	0.00236	**65**	365	359	0.1634	-0.00034
27	1525	1531	0.0000	0.00118	**66**	339	336	0.0000	0.00000
28	1483	1476	0.2727	-0.00103	**67**	305	297	0.0445	0.00026
29	1454	1436	0.0902	-0.00701	**68**	265	268	0.0010	0.00000
30	1403	1426	0.0131	0.03296	**69**	249	262	0.0000	0.00000
31	1369	1406	0.2106	-0.01218	**70**	220	215	0.1296	0.00005
32	1341	1365	0.3156	-0.00554	**71**	211	211	0.0000	0.00000
33	1316	1316	0.0932	-0.00207	**72**	192	162	0.0000	0.00000
34	1298	1285	0.0203	0.00235	**73**	157	130	0.0000	0.00000
35	1261	1273	0.3848	-0.00349	**74**	112	107	0.0000	0.00000
36	1260	1258	0.0000	0.00000	**75**	96	88	0.0000	0.00000
37	1226	1256	0.0219	-0.00527	**76**	85	88	0.2494	0.00000
38	1211	1217	0.0003	-0.00007	**77**	55	51	0.0000	0.00000
39	1165	1146	0.0000	0.00000	**78**	39	16	0.0000	0.00000

4.1.6 Absorption and Fluorescence Spectra of HBDI for C_1 Symmetry

In order to completely describe the solvent effect, the inhomogeneous broadening, namely D_{ba}, is taken into account in the Franck-Condon simulations. From **Fig. 11(b)**, the maximum absorption with PCM (Methanol, 416 nm) is red shift about 3000 cm^{-1} compared to the experiment. But the maximum absorption for B3LYP/TD-B3LYP without PCM (375 nm) in **Fig. 11(c)** is different to **Fig. 11(b)** which is just red shift 259 cm^{-1}. Both of the simulations for B3LYP/TD-B3LYP and PCM (Methanol) calculations are shown in better agreement with the experiment although the FWHM is a little underestimated in B3LYP/TD-B3LYP calculation and a little overestimated in PCM (Methanol) calculation. Only the absorption spectrum for HF/CIS calculation shows disagreement with the experiment which is nearly 1.5 times the width and the FWHM of the absorption spectrum. The broad width can be attributed to the strong displacement between S_0 and S_1. These normal modes significantly contribute to the absorption and fluorescence spectra.

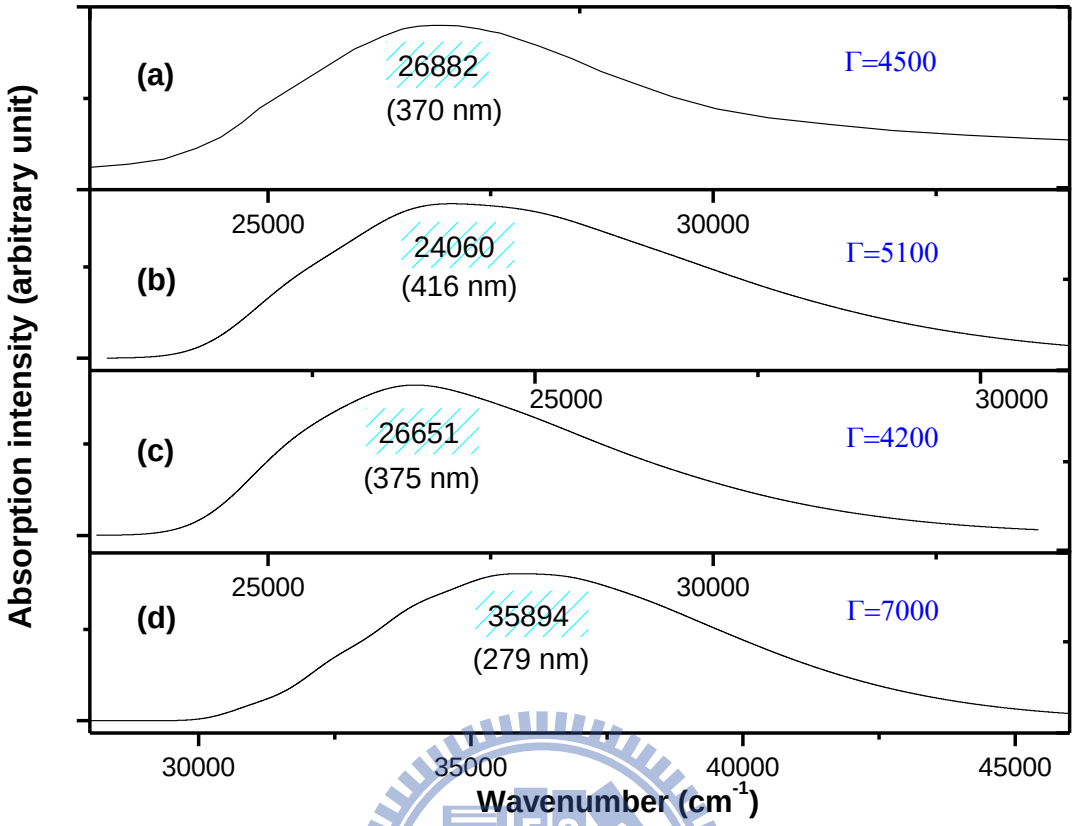

Fig. 11 Absorption spectra of **HBDI** at 298K. (a) Experimental spectrum from Ref. [42] , (b) simulated spectrum for r_{ba} = 10 cm^{-1} and D_{ba} = 800 cm^{-1} from B3LYP/TD-B3LYP with PCM (Methanol) method, (c) simulated spectrum for r_{ba} = 10 cm^{-1} and D_{ba} = 800 cm^{-1} from B3LYP/TD-B3LYP calculation, (d) simulated spectrum for r_{ba} = 10 cm^{-1} and D_{ba} = 800 cm^{-1} from HF/CIS calculation.

In **Fig. 12**, the simulations of the absorption spectra between the acetonitrile and methanol solvent are nearly close to each other. The factors of different H-bonding, non H-bonding, polar, and non-polar may cause the red or blue shift. The simulations in **Fig. 12** show the red shift spectra compared to the Ref. [43]. Only the sequence is the same as the experiment result which the absorption maxima are among 370 nm (27027 cm^{-1}) ~ 376 nm (26596 cm^{-1}) [43].

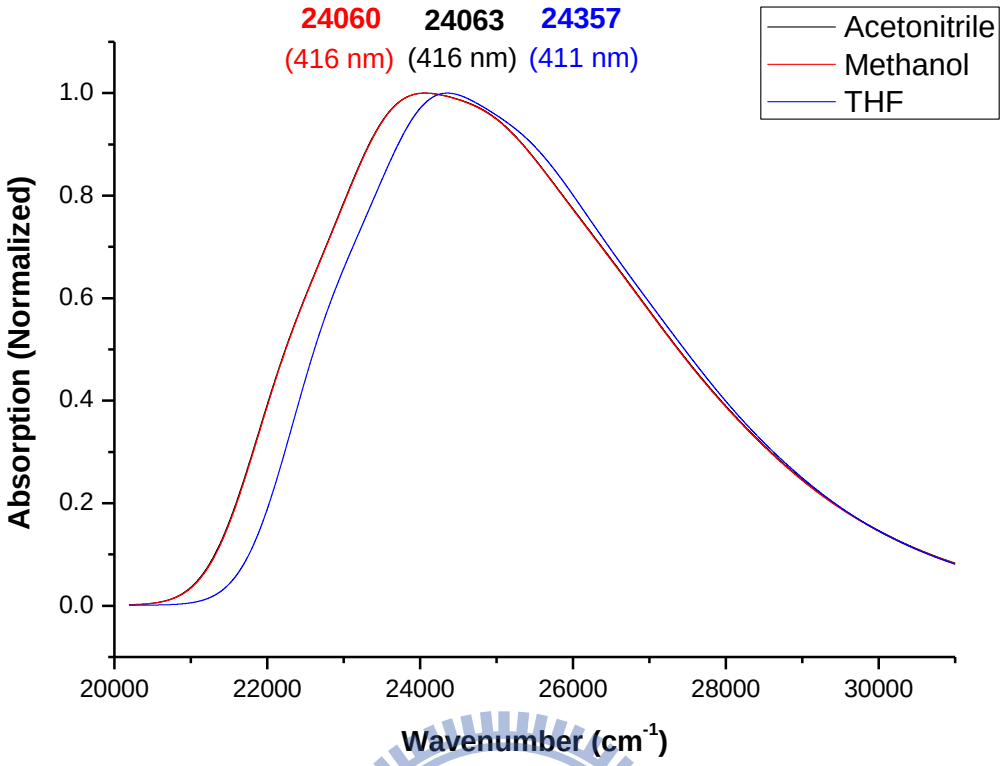

Fig. 12 Simulated absorption spectra of **HBDI** in various solvents at 298K. (a) acetonitrile, (b) methanol, (c) THF. All the spectra were simulated for r_{ba} = 10 cm^{-1} and D_{ba} = 800 cm^{-1}

The same experimental condition for the fluorescence spectrum is shown in **Fig. 13(a)**. The maxima show red shift about 2700 cm^{-1} for **Fig. 13(b)** and nearly the same (slightly 384 cm^{-1} blue shift) as the experimental maximum for **Fig. 13(c)**. Only the HF/CIS calculation still gives disagreement with the experiment result.

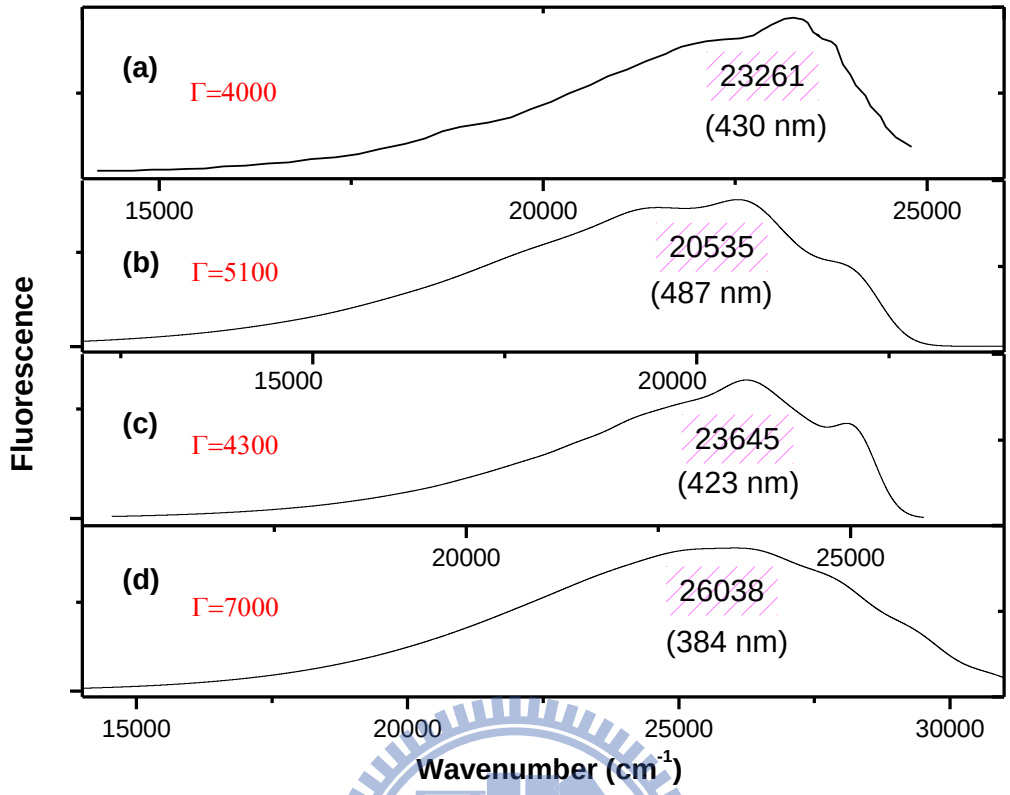

Fig. 13 Fluorescence spectra of **HBDI** at 298K (a) Experimental spectrum from Ref. [42], (b) simulated spectrum for r_{ba} = 10 cm^{-1} and D_{ba} = 500 cm^{-1} from B3LYP/TD-B3LYP with PCM (Methanol) calculation, (c) simulated spectrum for r_{ba} = 10 cm^{-1} and D_{ba} = 400 cm^{-1} from B3LYP/TD-B3LYP calculation, (d) simulated spectrum for r_{ba} = 10 cm^{-1} and D_{ba} = 700 cm^{-1} from HF/CIS calculation.

Fig. 14(a) shows the another experiment result for fluorescence spectrum of **HBDI** at 77K from Ref. [16] using non H-bonding 2-methyl THF glasses for solvent. In contrast to the previous H-bonding solvent (methanol), the vibronic structure in fluorescence is quite obvious that attribute to the degree of inhomogeneous broadening in the solvent. The experiment displays the FWHM which is equal to 5300 cm^{-1}. In this study, the treatment is using THF (ε = 7.43) solvent which the dielectric constant is similar 2-methyl THF (ε = 6.97) solvent in PCM method. The maximum fluorescent intensity is close to 434 nm (23062 cm^{-1}) compared to 474 nm (21092

cm^{-1}) for PCM (THF) calculation (see **Fig. 14(b)**), 423 nm (23645 cm^{-1}) for B3LYP/TD-B3LYP calculation (see **Fig. 14(c)**), and 379 nm (26414 cm^{-1}) for HF/CIS calculation (see **Fig. 14(d)**), respectively. As a result, it is red shift for PCM (THF) and HF/CIS results but a little blue shift for B3LYP/TD-B3LYP result compared to the experimental spectrum. The primary shoulder is also observed in better agreement with PCM (THF) and TD-DFT calculations but HF/CIS result shows in disagreement with the experimental spectrum. The values of FWHM demonstrate the agreement between PCM (THF, Γ=5200 cm^{-1}) or B3LYP/TD-B3LYP (Γ=4300 cm^{-1}) calculations with the experiment. The FWHM of HF/CIS (Γ=8000 cm^{-1}) almost two times larger than B3LYP/TD-B3LYP result.

Fig. 15 presents the absorption spectrum at 298K and fluorescence spectrum at 77K for different solvents which is well simulated by B3LYP/TD-B3LYP method. The stick spectrum represents the Frank-Condon factors which contain the Huang-Rhys factors (S^{HR}). **Fig. 15** also assigns the 0-0 lines and other important band lines for the main contributions.

This information could be obtained from the S^{HR} which are listed for larger than 0.1 among 78 normal-mode-frequencies in the **Table 11**. These normal modes significantly contribute to the absorption and fluorescence spectra. The results obtained with B3LYP/TD-B3LYP calculation show the maximum S^{HR} of the mode 53 (S^{HR} = 0.4103). But in the case of considering solvent effects which displayed the maximum S^{HR} of the mode 16 (S^{HR} =0.4082 in methanol and S^{HR} =0.3511 in THF). The previous mode 53 is no longer maximum for the PCM methods. Moreover, the mode 76 presents the slight geometrical changes which S^{HR} is only 0.0679 for B3LYP method but the corresponding mode in PCM method is mode 75. Mode 53 and mode 16 in B3LYP/TD-B3LYP calculation are shown in **Fig. 16**, to **Fig. 42.**

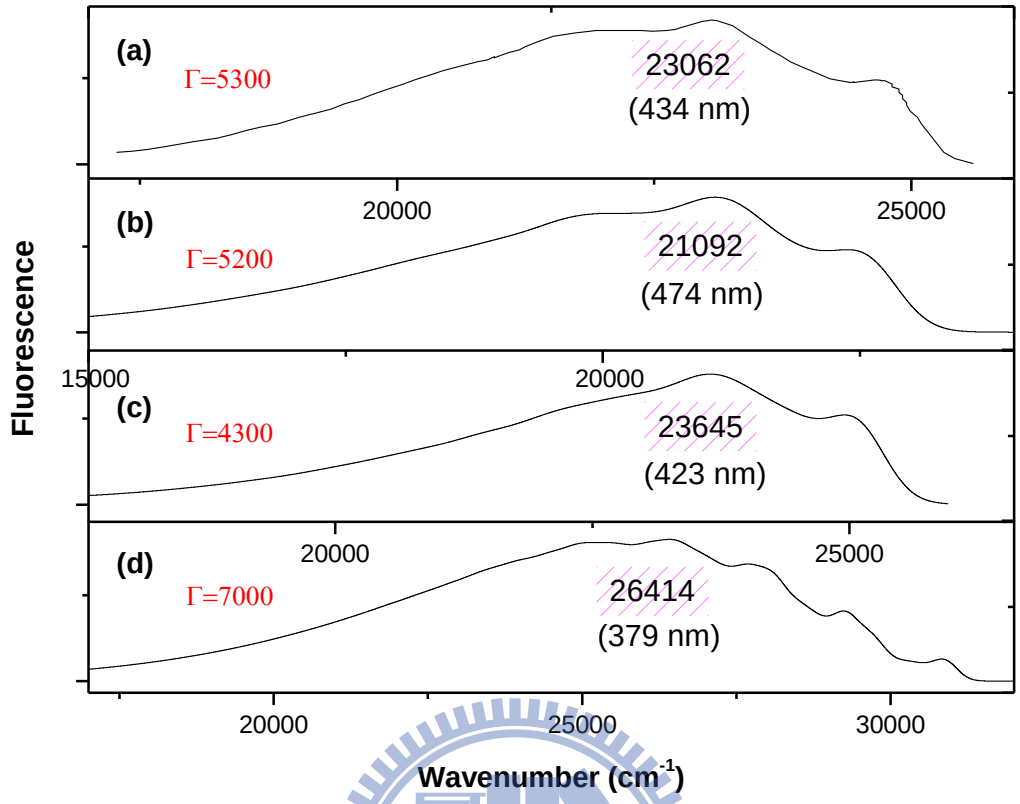

Fig. 14 Fluorescence spectra at 77K (a) Experimental spectrum from Ref. [16], (b) simulated spectrum for r_{ba} = 10 cm^{-1} and D_{ba} = 450 cm^{-1} from B3LYP/TD-B3LYP with PCM (THF) calculation, (c) simulated spectrum for r_{ba} = 10 cm^{-1} and D_{ba} = 400 cm^{-1} from B3LYP/TD-B3LYP calculation, (d) simulated spectrum for r_{ba} = 10 cm^{-1} and D_{ba} = 300 cm^{-1} from HF/CIS calculation.

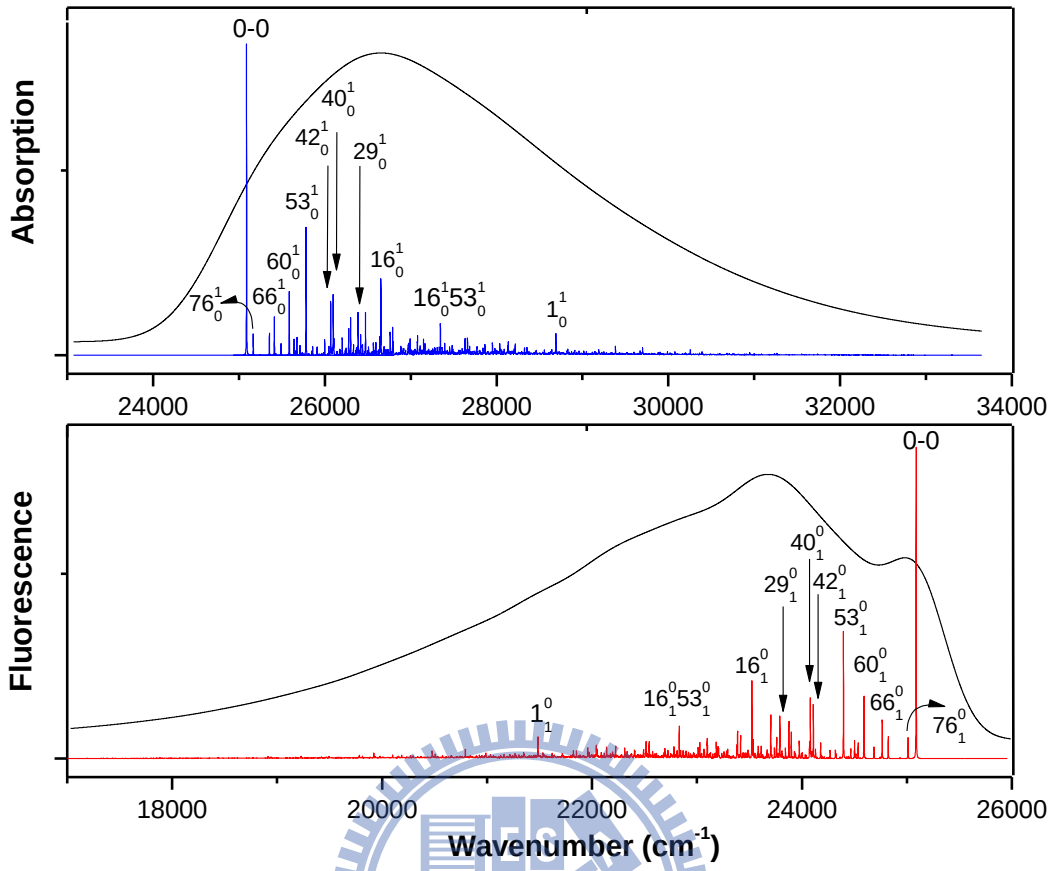

Fig. 15 Simulated absorption spectrum (Top, at 298K) and fluorescence spectrum (Bottom, at 77K) of **HBDI** using B3LYP/TD-B3LYP calculation. The stick spectrum represents the Frank-Condon factors and the important band lines are assigned for comparison. All the spectra were simulated for r_{ba} = 1 cm^{-1} and D_{ba} = 1 cm^{-1}.

Table 11 Calculated vibrational frequencies (cm^{-1}) for ground state and the corresponding Huang-Rhys factors (dimensionless). The frequencies multiplied by scaling factor (0.9614) are provided in the brackets.

	TD-B3LYP		PCM (Methanol)		PCM (THF)	
Mode	Freq	S^{HR}	Freq	S^{HR}	Freq	S^{HR}
ν_{16}	1627(1564)	0.24(0.23)	1621(1558)	0.41(0.39)	1622(1560)	0.35(0.34)
ν_{29}	1351(1299)	0.14(0.13)	1348(1296)	0.25(0.24)	1349(1297)	0.22(0.21)
ν_{32}	1261(1212)	0.12(0.12)	1261(1213)	0.17(0.16)	1262(1213)	0.15(0.15)
ν_{40}	1049(1009)	0.19(0.19)	1048(1007)	0.15(0.14)	1048(1008)	0.15(0.14)
ν_{42}	1019(980)	0.17(0.17)	1025(985)	0.15(0.15)	1024(985)	0.17(0.17)
ν_{53}	720(693)	0.41(0.39)	719(691)	0.36(0.35)	719(692)	0.34(0.33)
ν_{60}	517(497)	0.20(0.20)	516(496)	0.28(0.27)	516(496)	0.24(0.23)
ν_{66}	337(324)	0.12(0.12)	338(325)	0.18(0.18)	338(325)	0.16(0.15)
ν_{76}[a]	80(77)	0.07(0.07)	79(75)	0.12(0.12)	79(76)	0.10(0.10)

[a]This vibration mode is equal to number 75 in methanol and THF solvents.

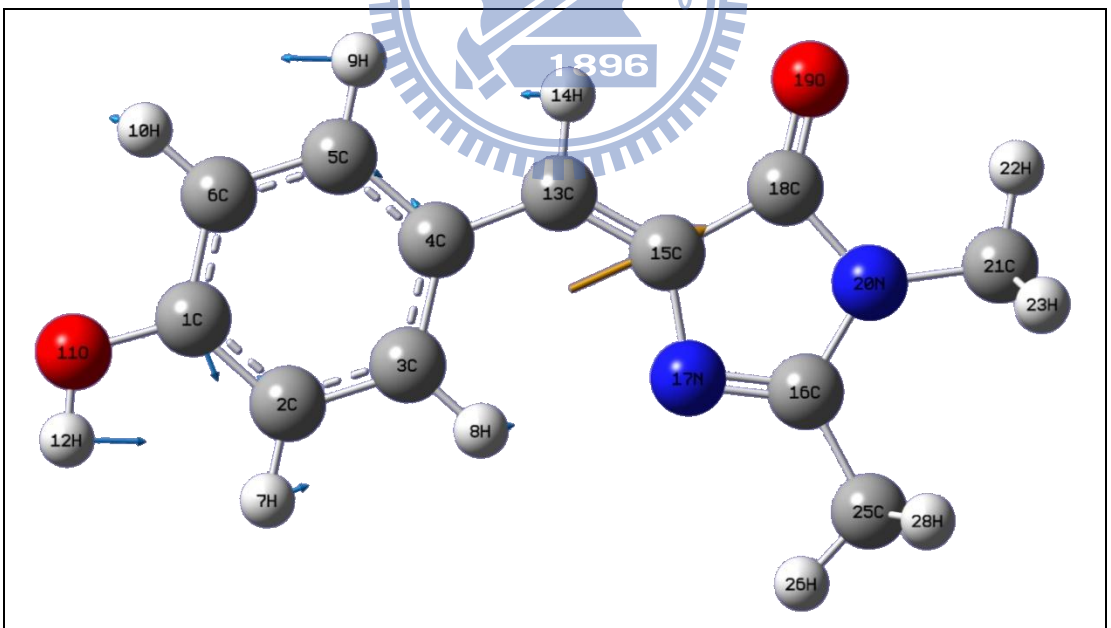

Mode 16 = 1627 cm^{-1}	**S^{HR}** = 0.2353

Fig. 16 Mode 16 of gas phase in B3LYP/TD-B3LYP calculation. The purple and orange arrows represent displacement vectors and dipole derivative vector, respectively.

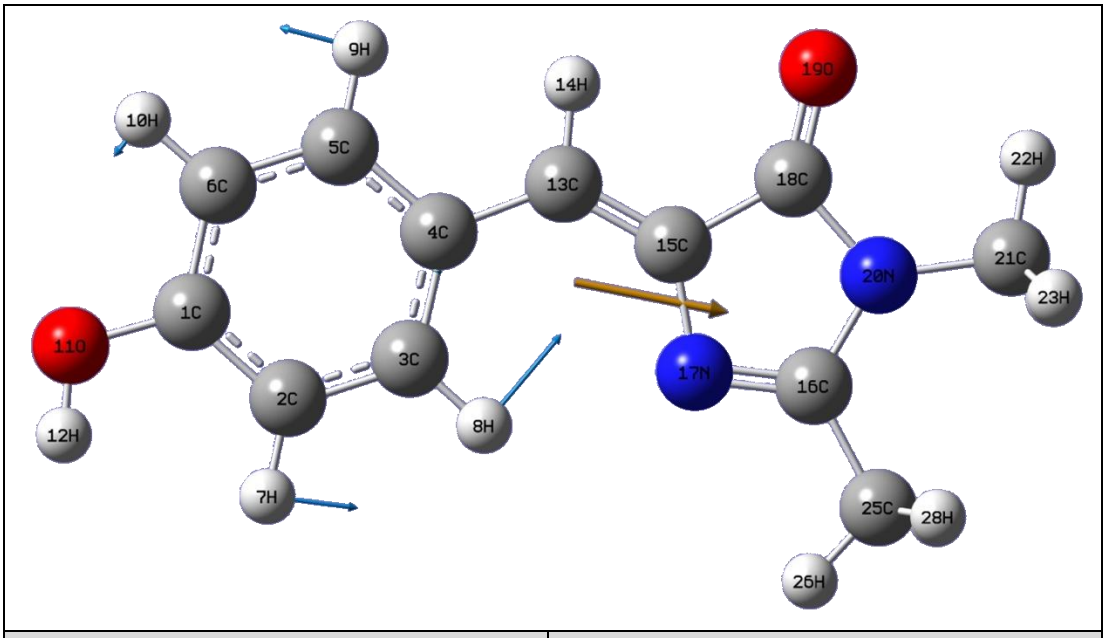

Mode 29 = 1351 cm^{-1}	$\mathbf{S^{HR}}$ = 0.1352

Fig. 17 Mode 29 of gas phase in B3LYP/TD-B3LYP calculation. The purple arrows represent the displacement vectors and the orange arrow represents dipole derivative vector.

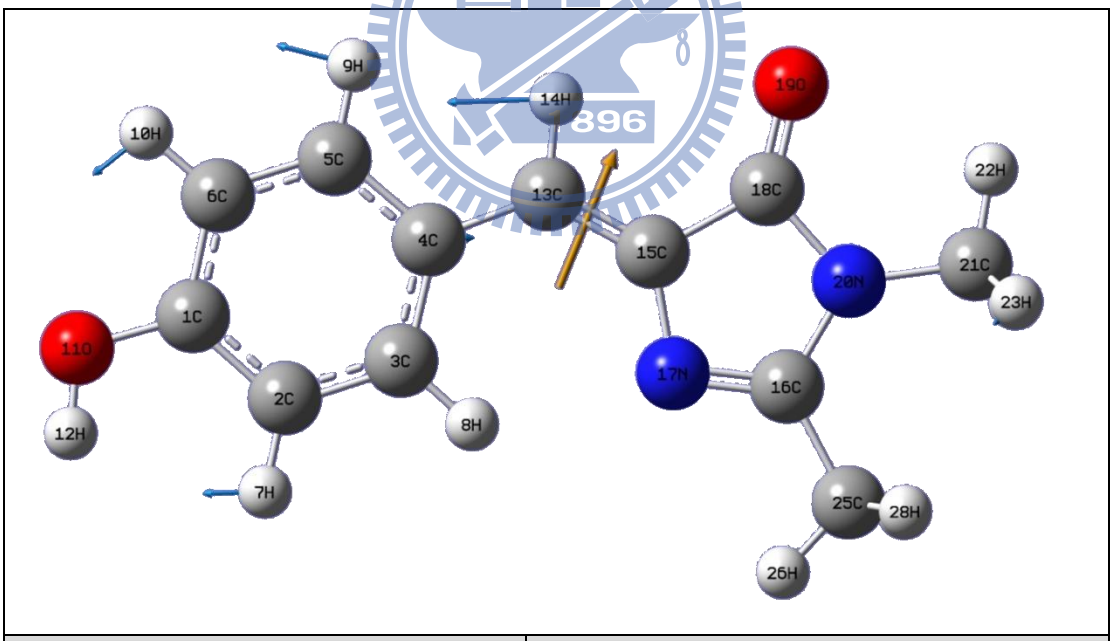

Mode 32 = 1261 cm^{-1}	$\mathbf{S^{HR}}$ = 0.1197

Fig. 18 Mode 32 of gas phase in B3LYP/TD-B3LYP calculation. The purple arrows represent the displacement vectors and the orange arrow represents dipole derivative vector.

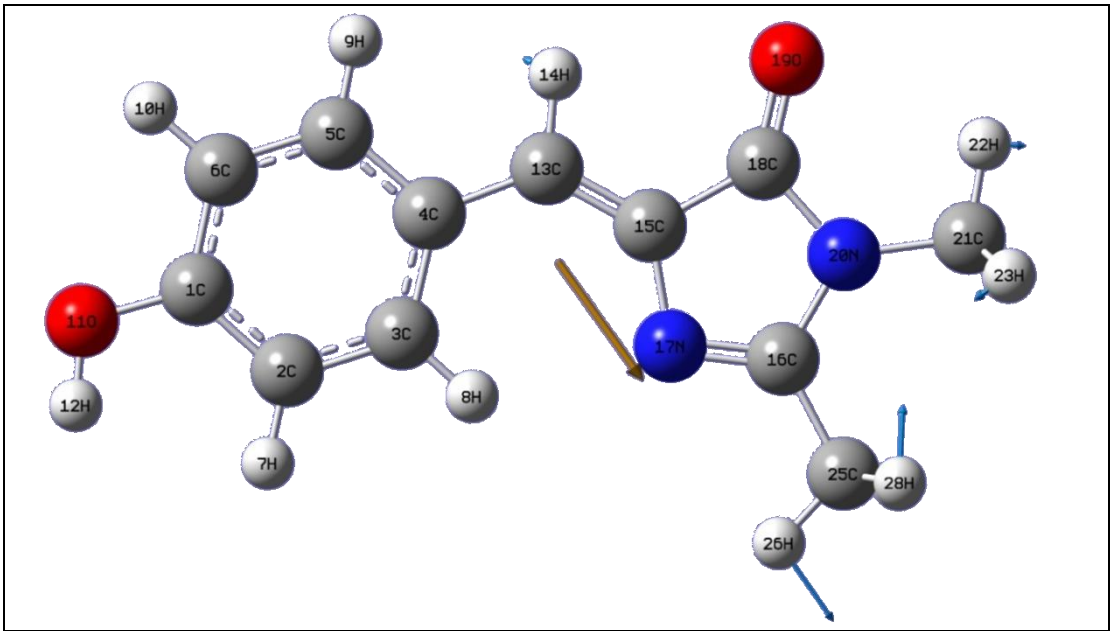

Mode 40 = 1049 cm^{-1}	$\mathbf{S^{HR}}$ = 0.1940

Fig. 19 Mode 40 of gas phase in B3LYP/TD-B3LYP calculation. The purple arrows represent the displacement vectors and the orange arrow represents dipole derivative vector.

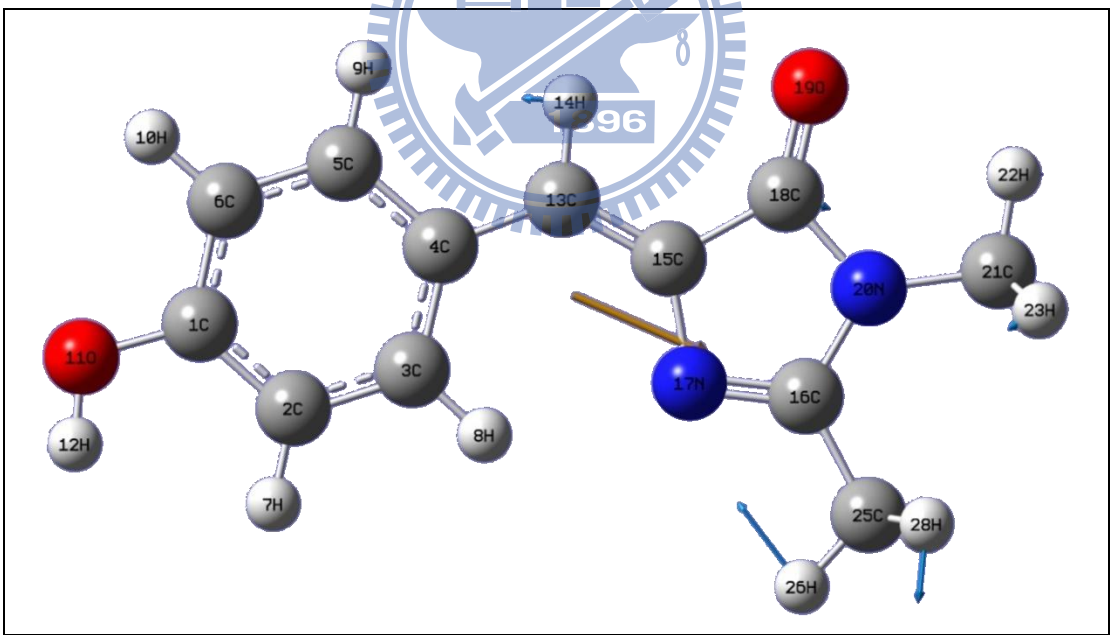

Mode 42 = 1019 cm^{-1}	$\mathbf{S^{HR}}$ = 0.1725

Fig. 20 Mode 42 of gas phase in B3LYP/TD-B3LYP calculation. The purple and orange arrows represent displacement vectors and dipole derivative vector, respectively.

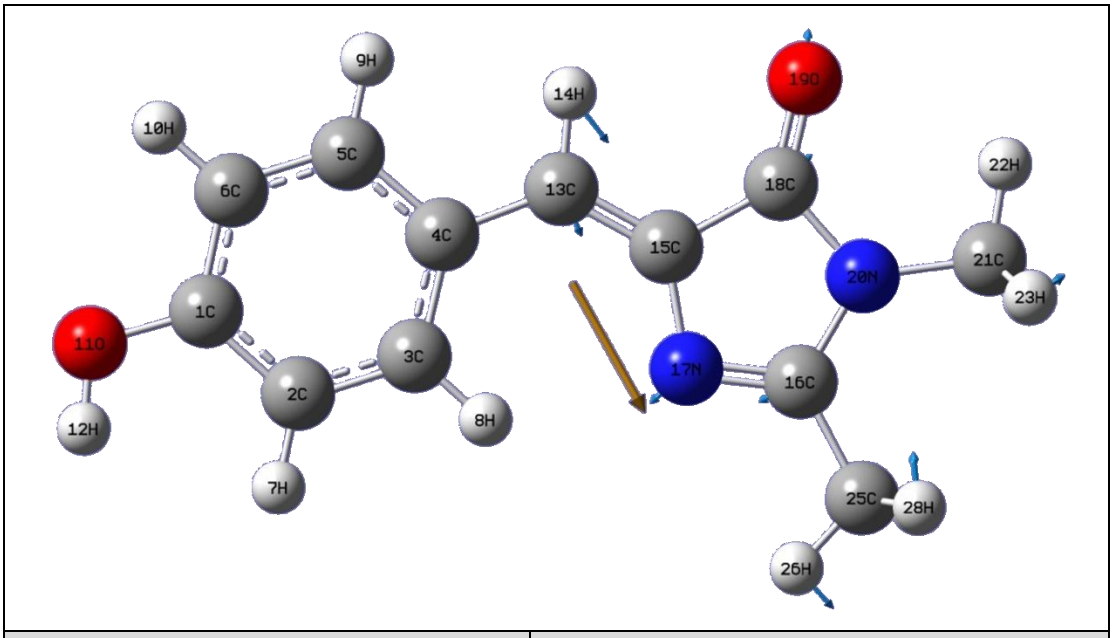

Mode 53 = 720 cm^{-1}	S^{HR} = 0.4103

Fig. 21 Mode 53 of gas phase in B3LYP/TD-B3LYP calculation. The purple and orange arrows represent displacement vectors and dipole derivative vector, respectively.

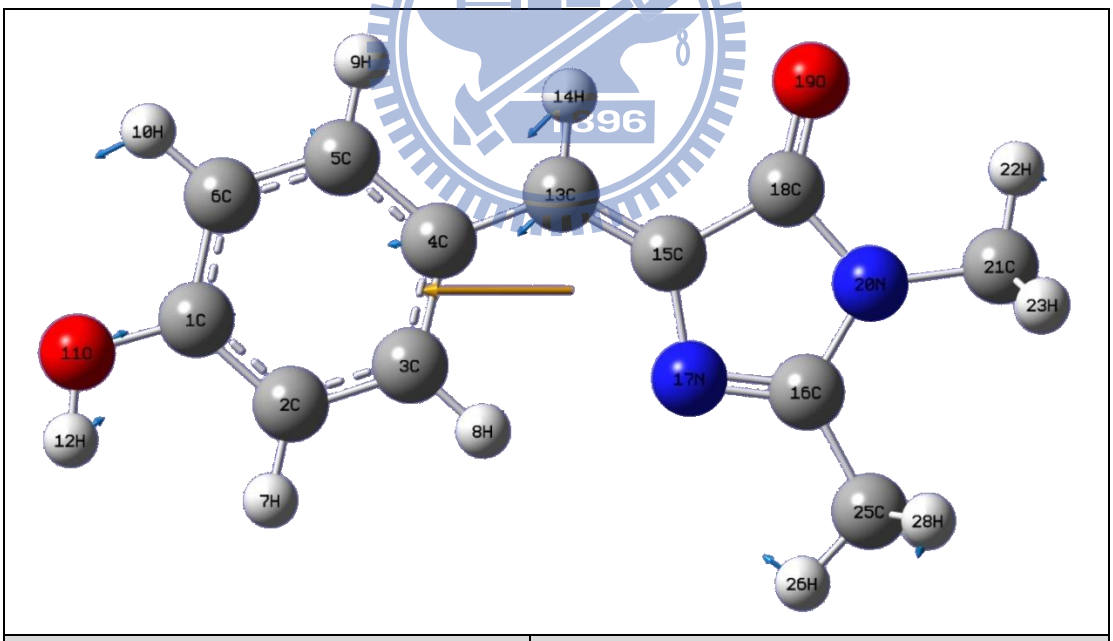

Mode 60 = 517 cm^{-1}	S^{HR} = 0.2034

Fig. 22 Mode 60 of gas phase in B3LYP/TD-B3LYP calculation. The purple and orange arrows represent displacement vectors and dipole derivative vector, respectively.

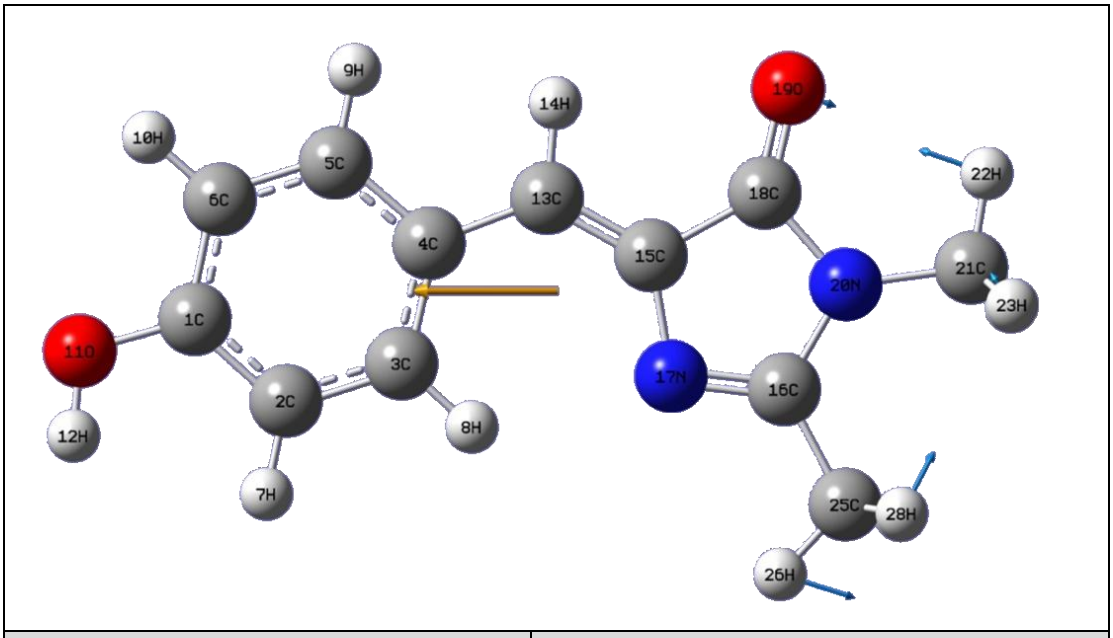

Mode 66 = 337 cm^{-1}	S^{HR} = 0.1240

Fig. 23 Mode 66 of gas phase in B3LYP/TD-B3LYP calculation. The purple and orange arrows represent displacement vectors and dipole derivative vector, respectively.

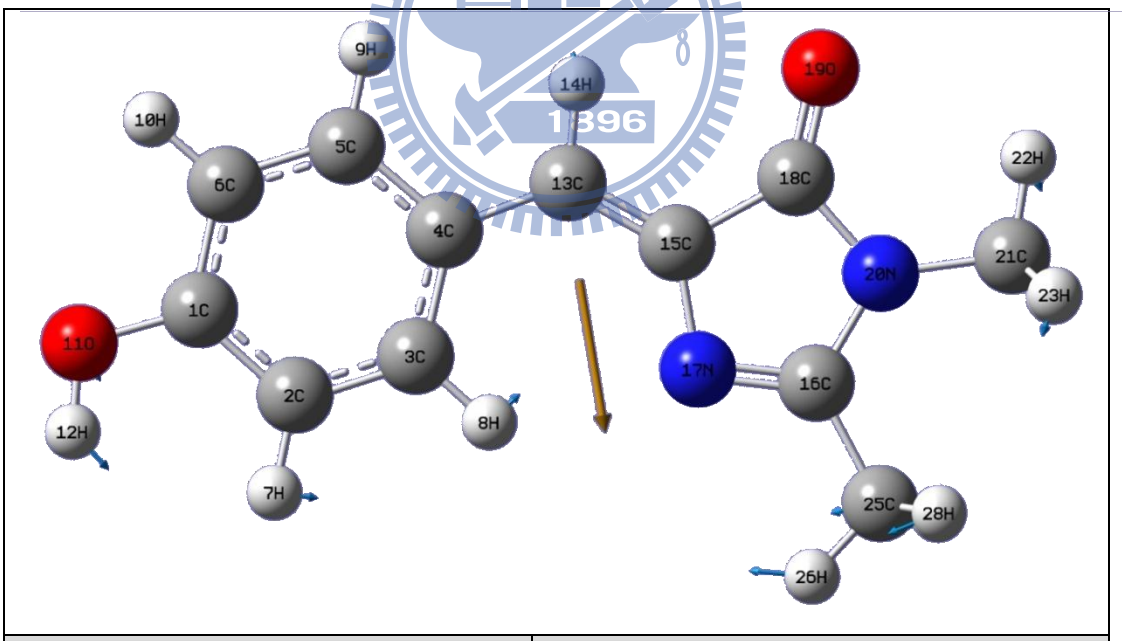

Mode 76 = 80 cm^{-1}	S^{HR} = 0.0679

Fig. 24 Mode 76 of gas phase in B3LYP/TD-B3LYP calculation. The purple and orange arrows represent displacement vectors and dipole derivative vector, respectively.

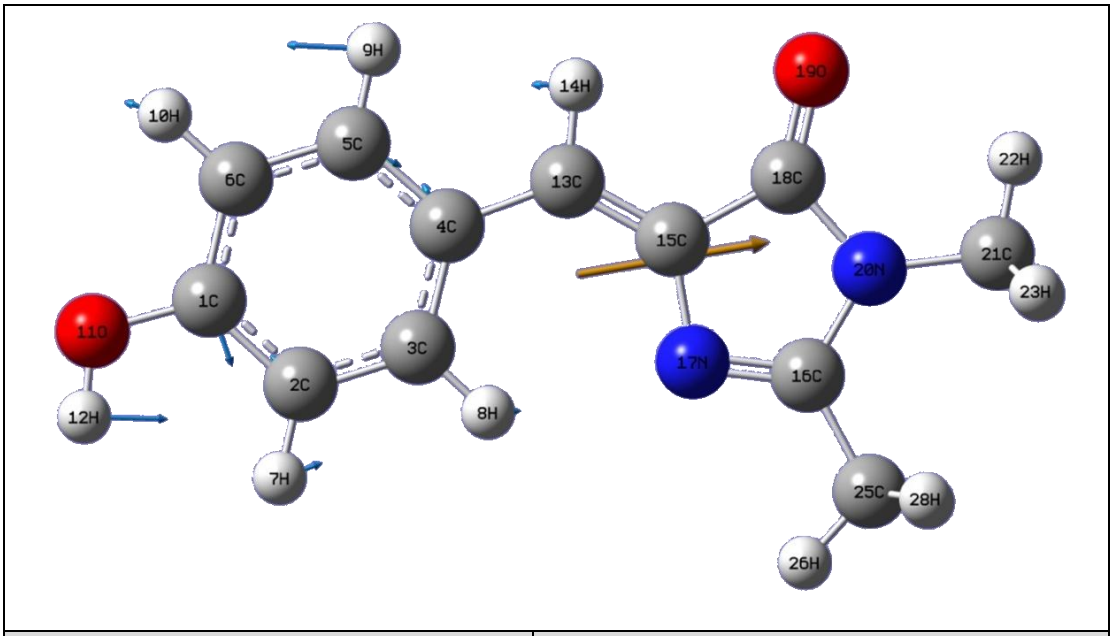

Mode 16 = 1621 cm^{-1}	S^{HR} = 0.4082

Fig. 25 Mode 16 in B3LYP/TD-B3LYP with PCM (methanol) calculation. The purple and orange arrows represent displacement vectors and dipole derivative vector, respectively.

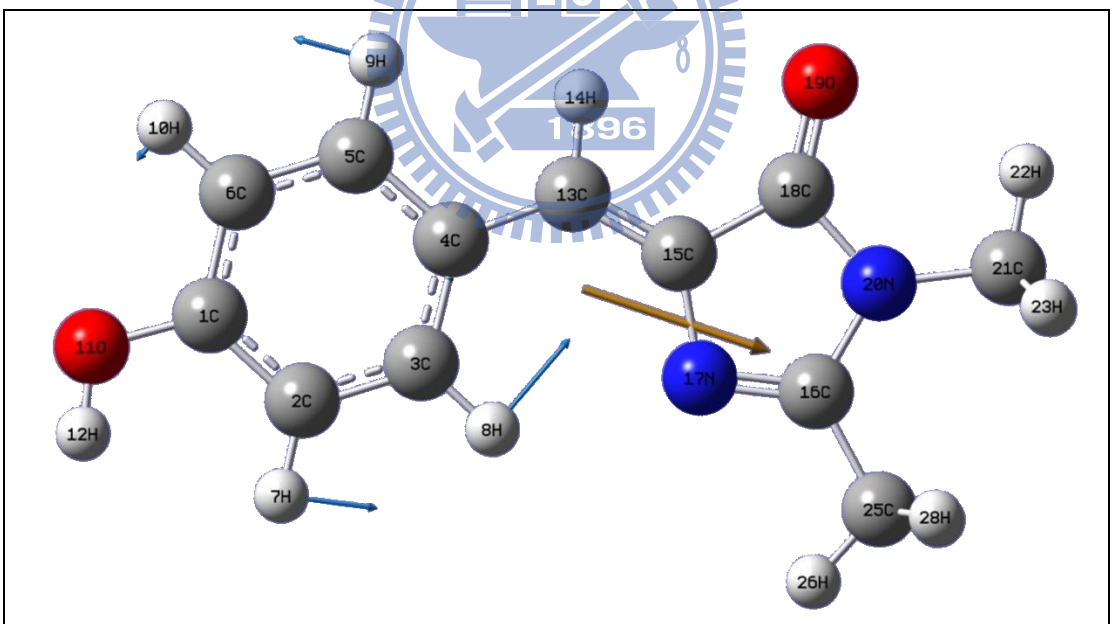

Mode 29 = 1348 cm^{-1}	S^{HR} = 0.2489

Fig. 26 Mode 29 in B3LYP/TD-B3LYP with PCM (methanol) calculation. The purple and orange arrows represent displacement vectors and dipole derivative vector, respectively.

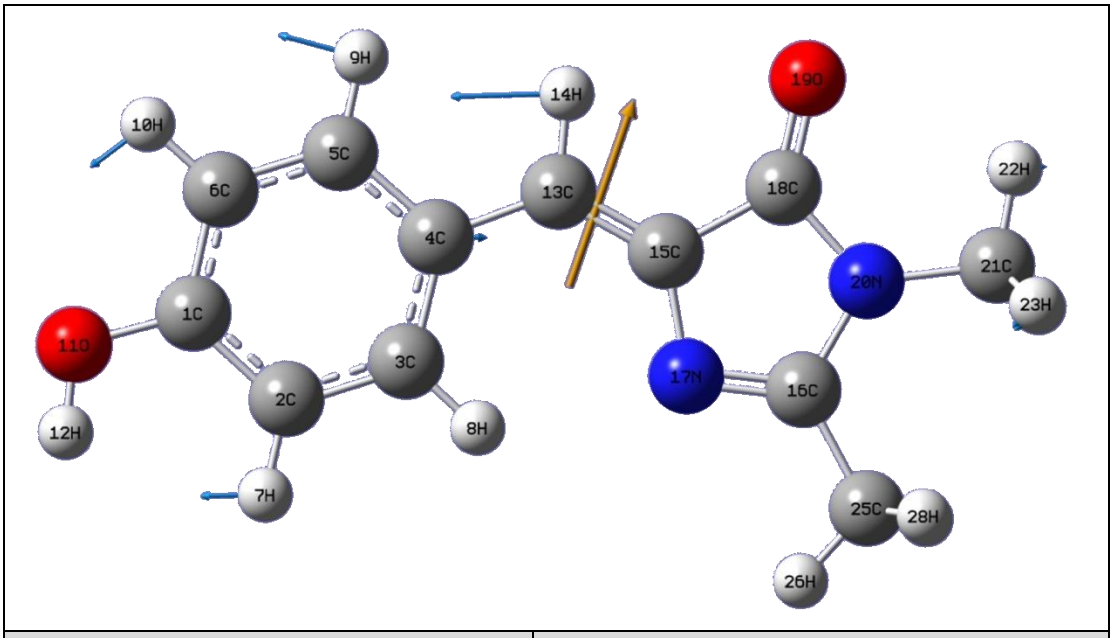

Mode 32 = 1261 cm^{-1}	$\mathbf{S^{HR}}$ = 0.1682

Fig. 27 Mode 32 in B3LYP/TD-B3LYP with PCM (methanol) calculation. The purple and orange arrows represent displacement vectors and dipole derivative vector, respectively.

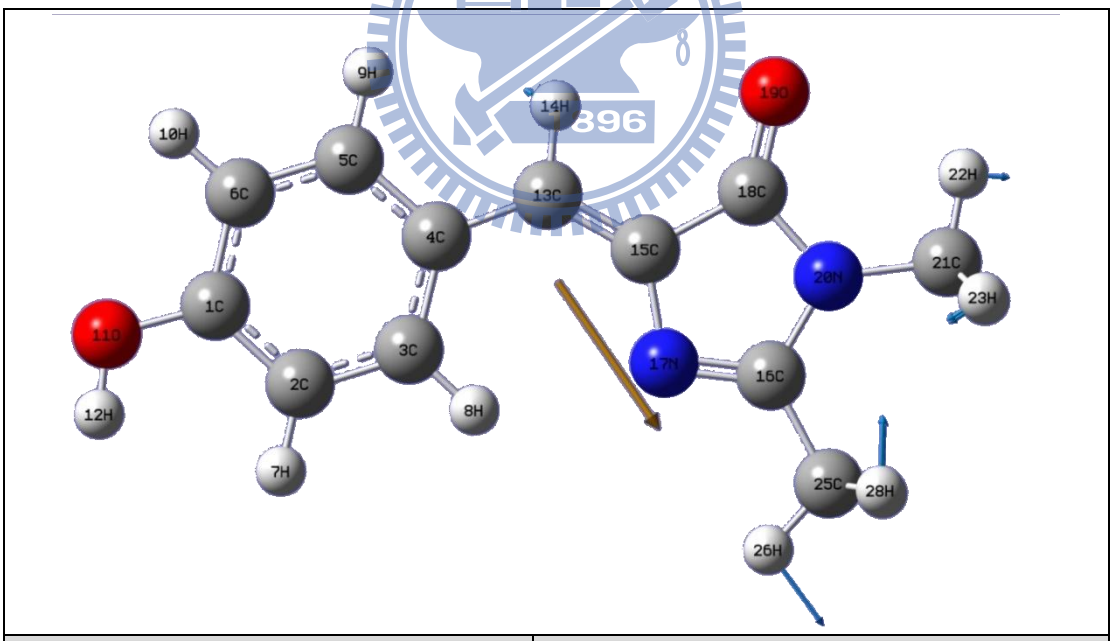

Mode 40 = 1048 cm^{-1}	$\mathbf{S^{HR}}$ = 0.1463

Fig. 28 Mode 40 in B3LYP/TD-B3LYP with PCM (methanol) calculation. The purple and orange arrows represent displacement vectors and dipole derivative vector, respectively.

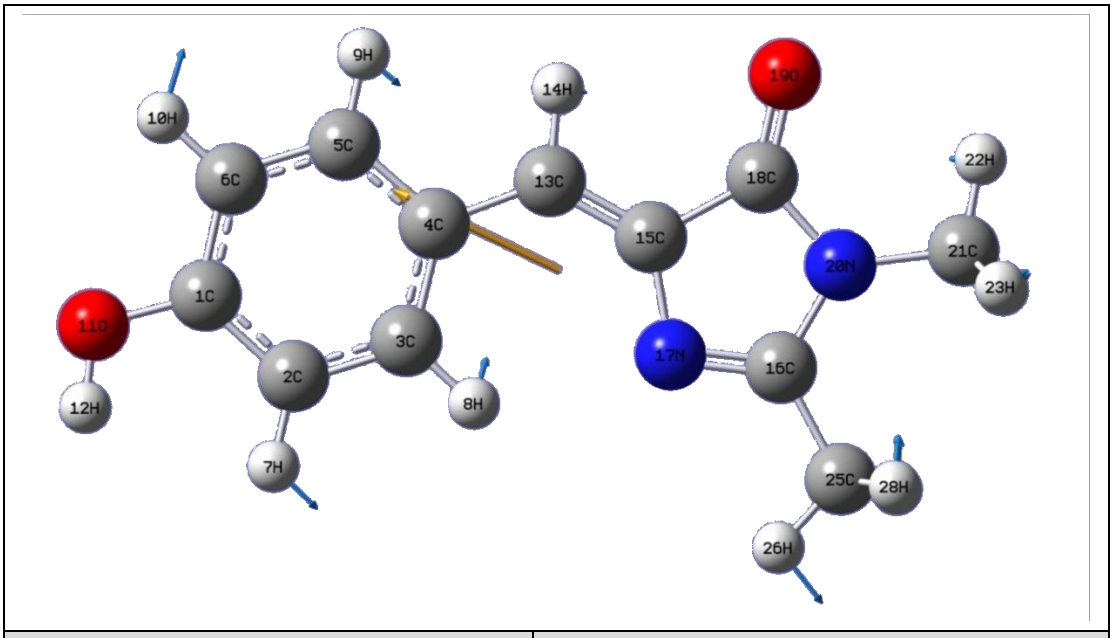

Mode 42 = 1025 cm^{-1}	S^{HR} = 0.1549

Fig. 29 Mode 42 in B3LYP/TD-B3LYP with PCM (methanol) calculation. The purple and orange arrows represent displacement vectors and dipole derivative vector, respectively.

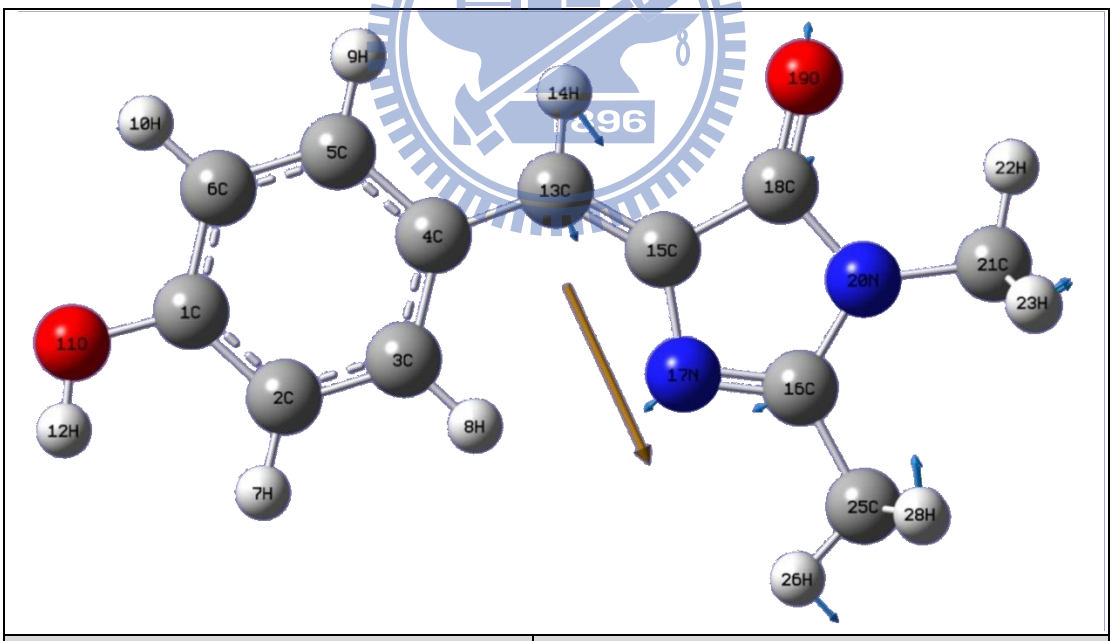

Mode 53 = 719 cm^{-1}	S^{HR} = 0.3590

Fig. 30 Mode 53 in B3LYP/TD-B3LYP with PCM (methanol) calculation. The purple and orange arrows represent displacement vectors and dipole derivative vector, respectively.

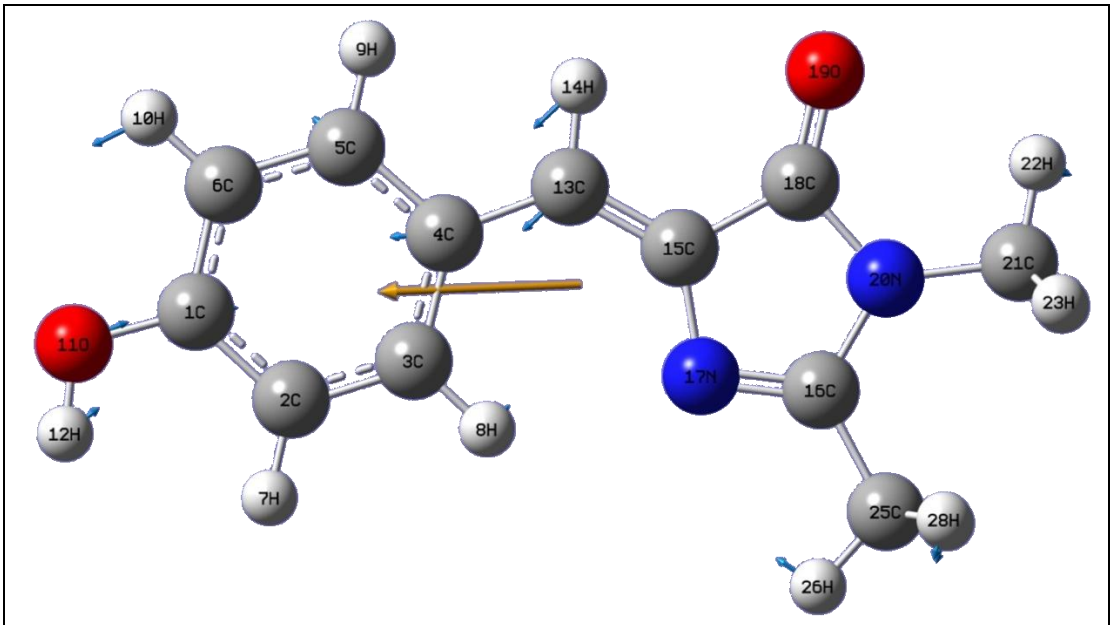

Mode 60 = 516 cm^{-1}	S^{HR} = 0.2794

Fig. 31 Mode 60 in B3LYP/TD-B3LYP with PCM (methanol) calculation. The purple and orange arrows represent displacement vectors and dipole derivative vector, respectively.

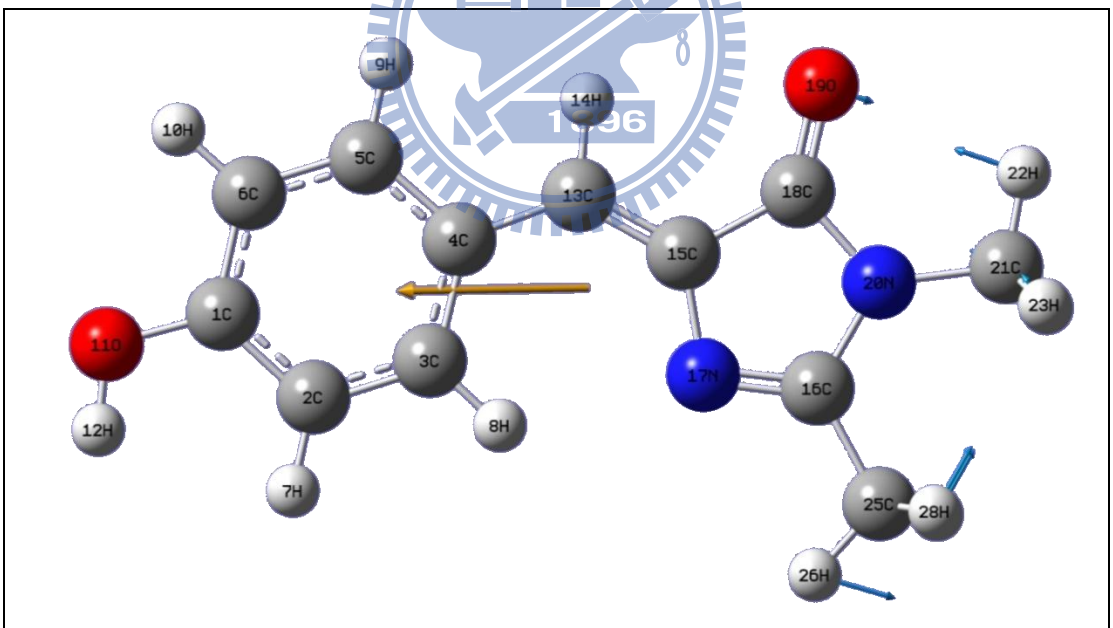

Mode 66 = 338 cm^{-1}	S^{HR} = 0.1823

Fig. 32 Mode 66 in B3LYP/TD-B3LYP with PCM (methanol) calculation. The purple and orange arrows represent displacement vectors and dipole derivative vector, respectively.

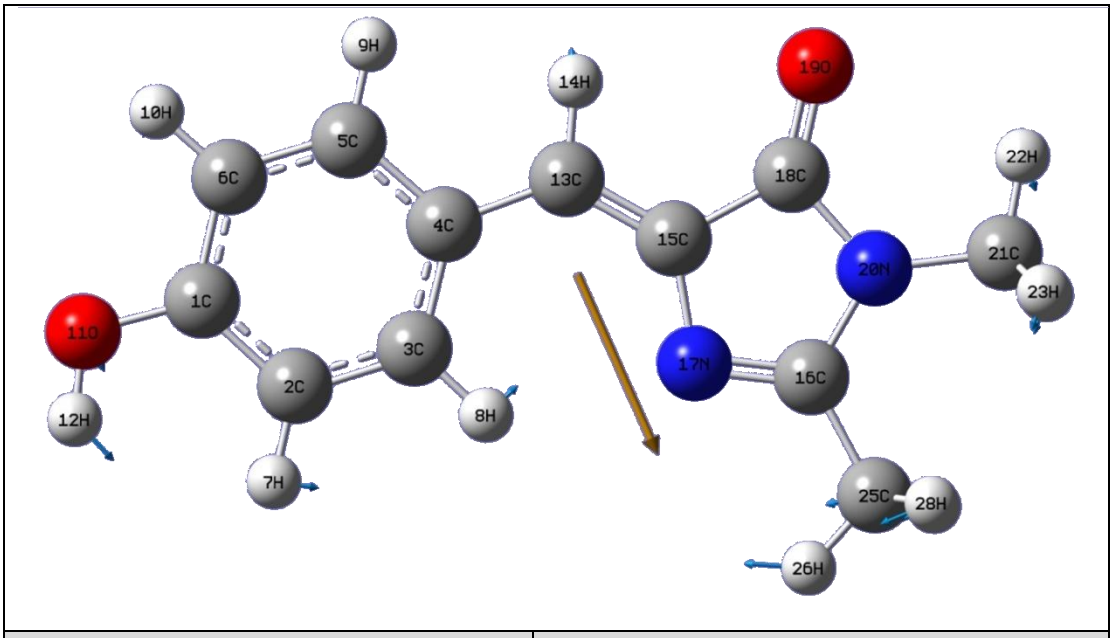

Mode 75 = 79 cm^{-1}	S^{HR} = 0.1198

Fig. 33 Mode 75 in B3LYP/TD-B3LYP with PCM (methanol) calculation. The purple and orange arrows represent displacement vectors and dipole derivative vector, respectively.

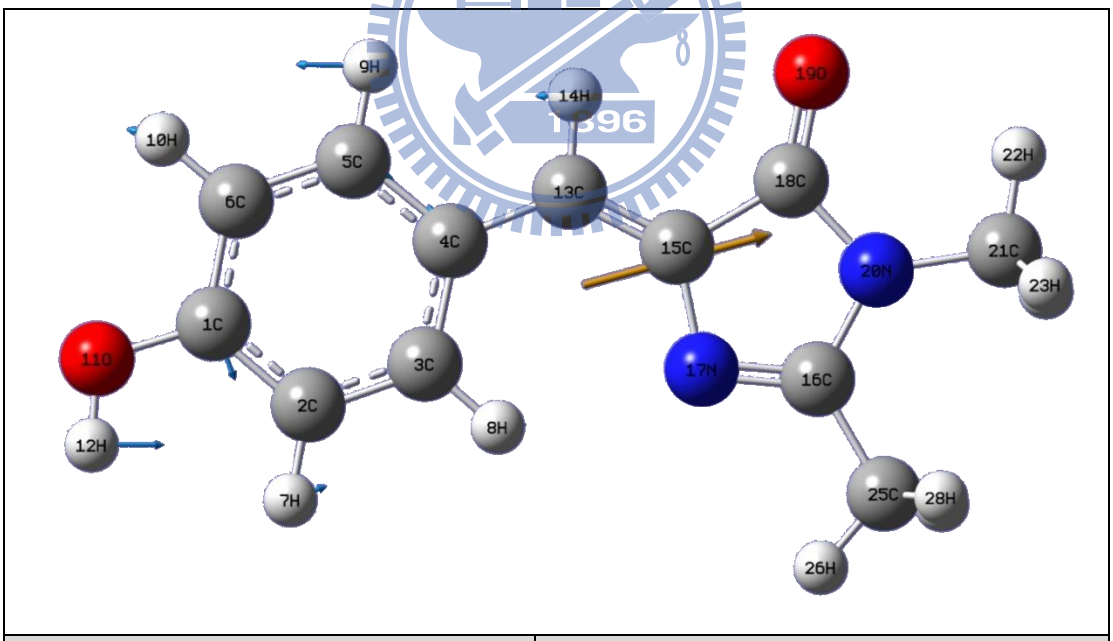

Mode 16 = 1622 cm^{-1}	S^{HR} = 0.3511

Fig. 34 Mode 16 in B3LYP/TD-B3LYP with PCM (THF) calculation. The purple and orange arrows represent displacement vectors and dipole derivative vector, respectively.

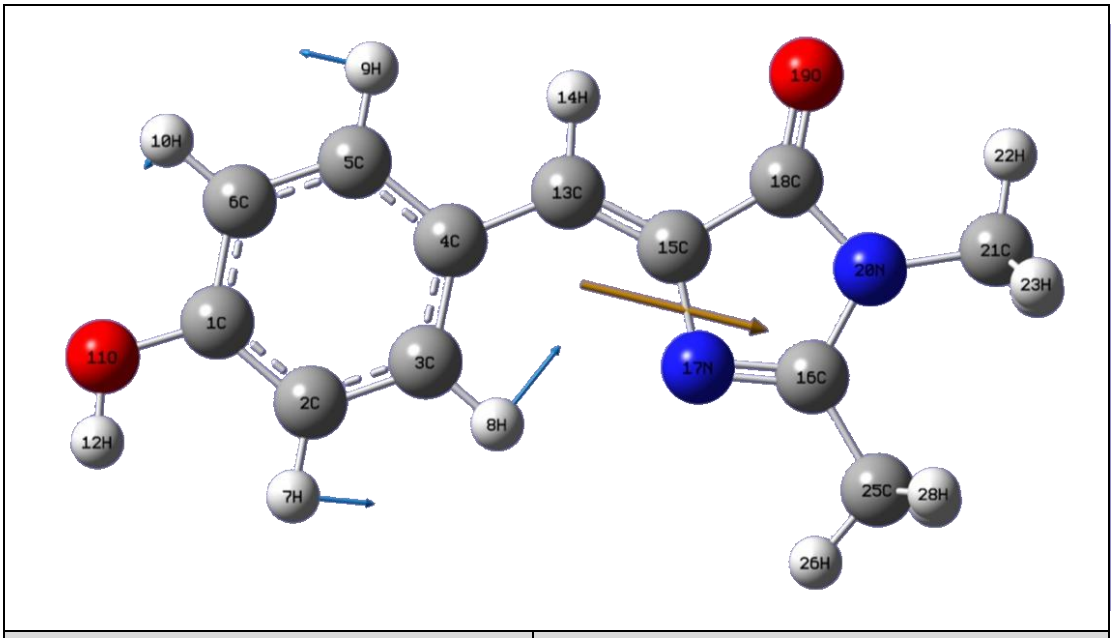

Mode 29 = 1349 cm^{-1}	S^{HR} = 0.2228

Fig. 35 Mode 29 in B3LYP/TD-B3LYP with PCM (THF) calculation. The purple and orange arrows represent displacement vectors and dipole derivative vector, respectively.

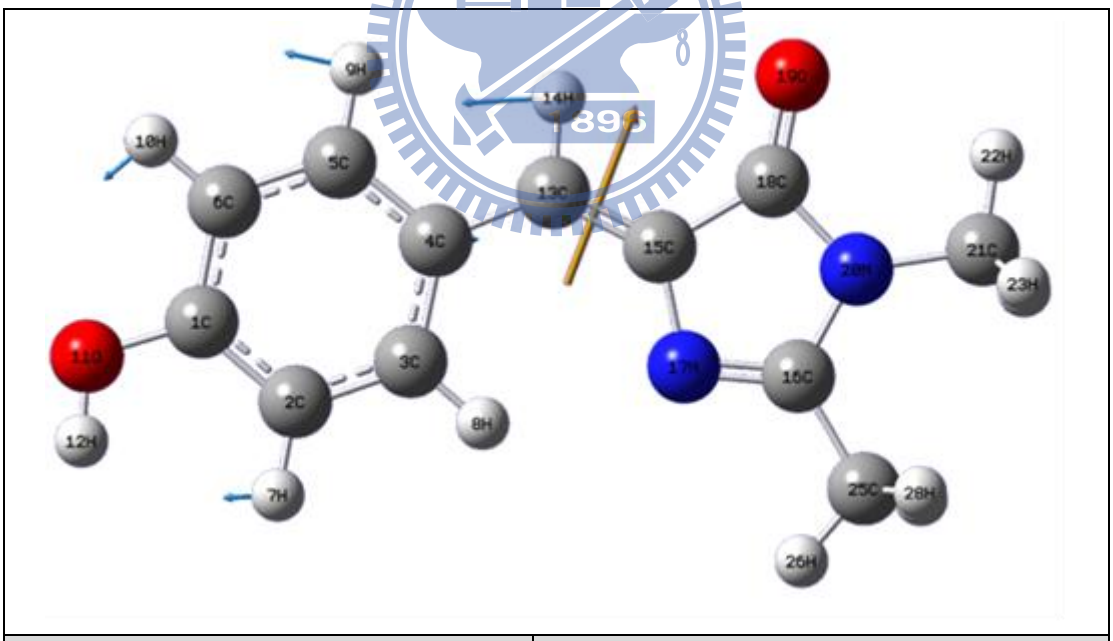

Mode 32 = 1262 cm^{-1}	S^{HR} = 0.1533

Fig. 36 Mode 32 in B3LYP/TD-B3LYP with PCM (THF) calculation. The purple and orange arrows represent displacement vectors and dipole derivative vector, respectively.

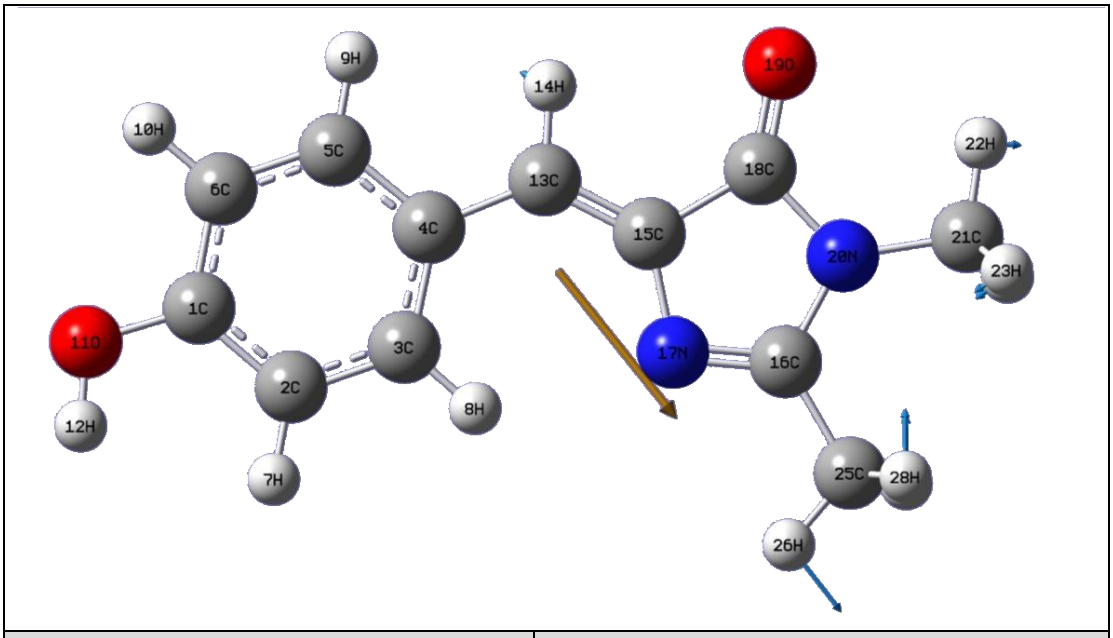

Mode 40 = 1048 cm^{-1}	S^{HR} = 0.1493

Fig. 37 Mode 40 in B3LYP/TD-B3LYP with PCM (THF) calculation. The purple and orange arrows represent displacement vectors and dipole derivative vector, respectively.

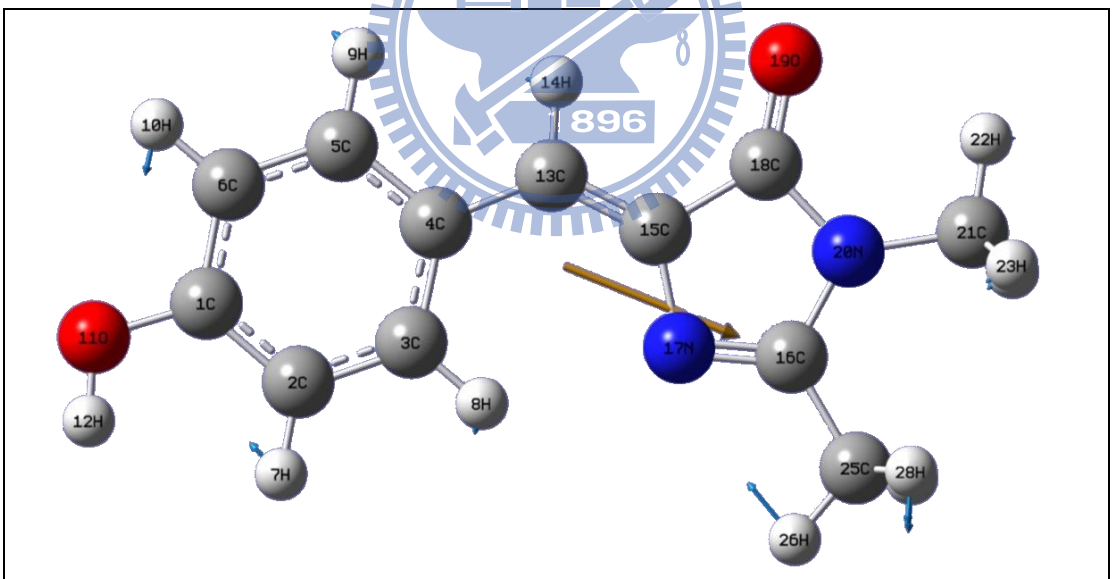

Mode 42 = 1024 cm^{-1}	S^{HR} = 0.1725

Fig. 38 Mode 42 in B3LYP/TD-B3LYP with PCM (THF) calculation. The purple and orange arrows represent displacement vectors and dipole derivative vector, respectively.

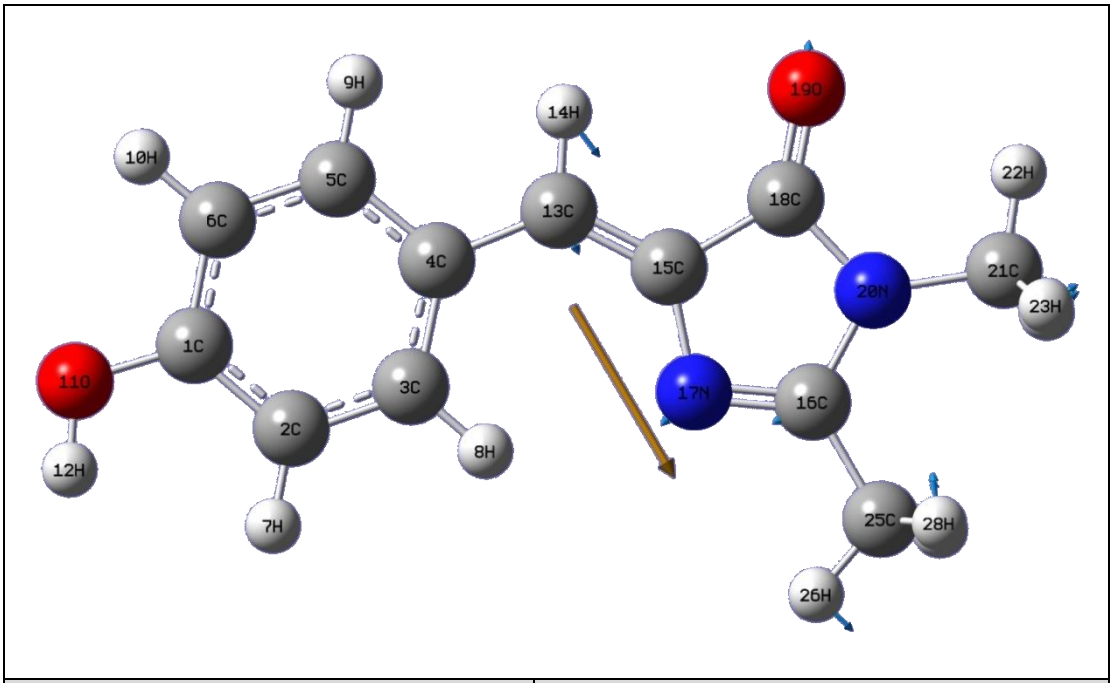

Mode 53 = 719 cm^{-1}	S^{HR} = 0.3441

Fig. 39 Mode 53 in B3LYP/TD-B3LYP with PCM (THF) calculation. The purple and orange arrows represent displacement vectors and dipole derivative vector, respectively.

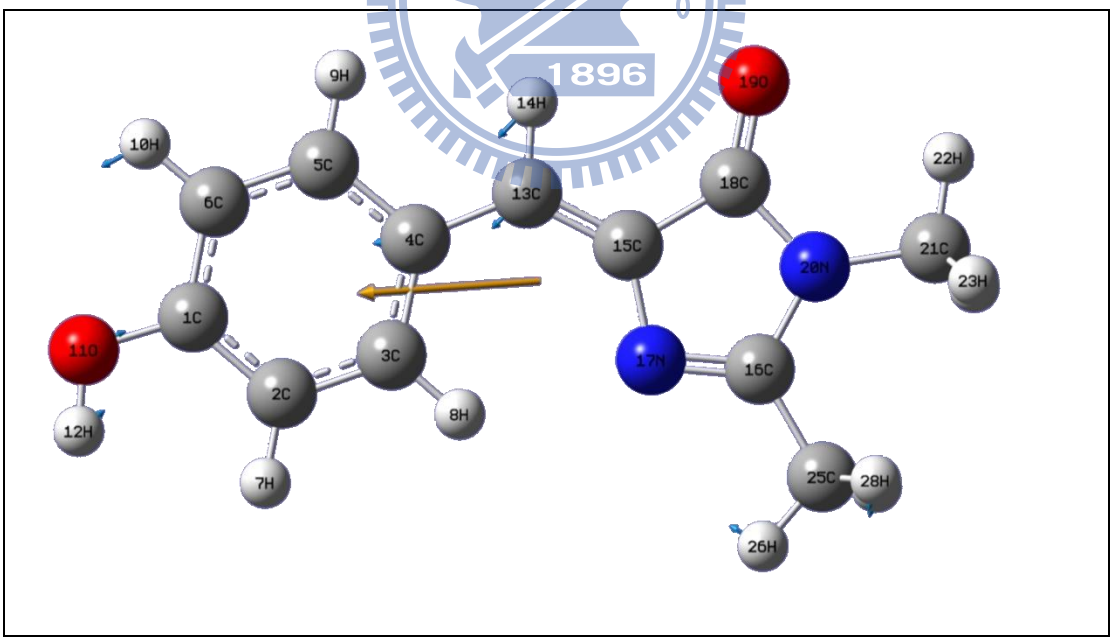

Mode 60 = 516 cm^{-1}	S^{HR} = 0.2355

Fig. 40 Mode 60 in B3LYP/TD-B3LYP with PCM (THF) calculation. The purple and orange arrows represent displacement vectors and dipole derivative vector, respectively.

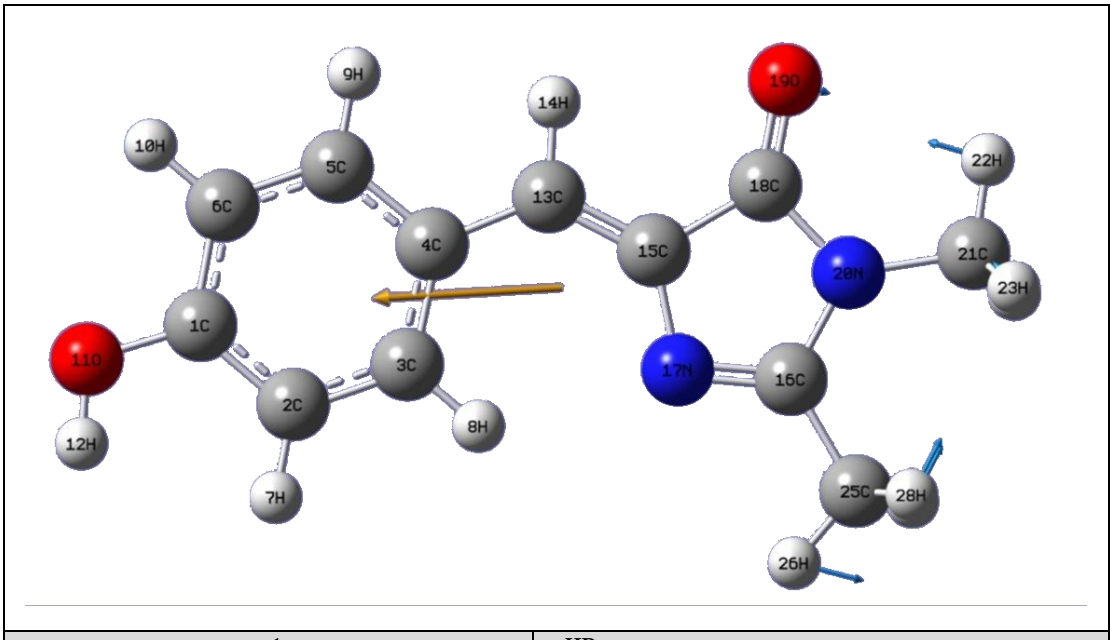

Mode 66 = 338 cm^{-1}	$\mathbf{S^{HR}}$ = 0.1577

Fig. 41 Mode 66 in B3LYP/TD-B3LYP with PCM (THF) calculation. The purple and orange arrows represent displacement vectors and dipole derivative vector, respectively.

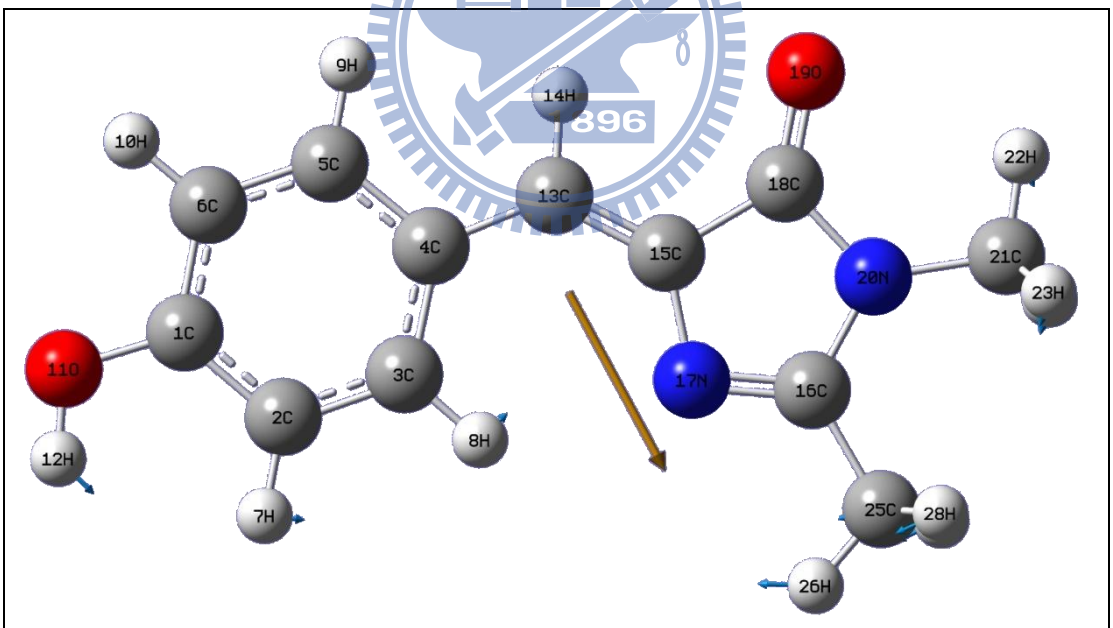

Mode 75 = 79 cm^{-1}	$\mathbf{S^{HR}}$ = 0.0977

Fig. 42 Mode 75 in B3LYP/TD-B3LYP with PCM (THF) calculation. The purple and orange arrows represent displacement vectors and dipole derivative vector, respectively.

Some important modes are listed in **Table 12** between one and no imaginary frequency for S_1. When the Huang-Rhys factor $S_j < 1$, it represents that this mode is a weak coupling. If $S_j >> 1$, this mode would be a strong coupling one. The corresponding modes are all larger than another result which exist one imaginary frequency of S_1. Previous section has mentioned that S_j = 6.4333 for mode 49 (826 cm^{-1}) and S_j = 3.9507 for mode 77 (54 cm^{-1}). We may, therefore, reasonably conclude that the strong coupling modes would be presented in the spectra for that no imaginary frequency in S_1. Its simulated absorption spectra are shown in **Fig. 43** which presents the broad width as the phenomenon in C_s symmetry (see **Fig. 7(b)**, **(c)**).

Table 12 Comparison of corresponding vibrational frequencies (cm^{-1}) modes with its Huang-Rhys factors (S^{HR}, dimensionless) between one and no imaginary frequency for S_1.

		TD-B3LYP (One imaginary frequency)	TD-B3LYP (No imaginary frequency)
Mode	Freq	S^{HR}	S^{HR}
ν_{16}	1627	0.2353	1.4434
ν_{29}	1351	0.1352	1.1624
ν_{32}	1261	0.1197	0.3598
ν_{40}	1049	0.1940	0.2073
ν_{42}	1019	0.1725	1.0120
ν_{53}	720	0.4103	1.5903
ν_{60}	517	0.2034	0.8508
ν_{66}	337	0.1240	0.7588
ν_{76}	80	0.0679	0.9457

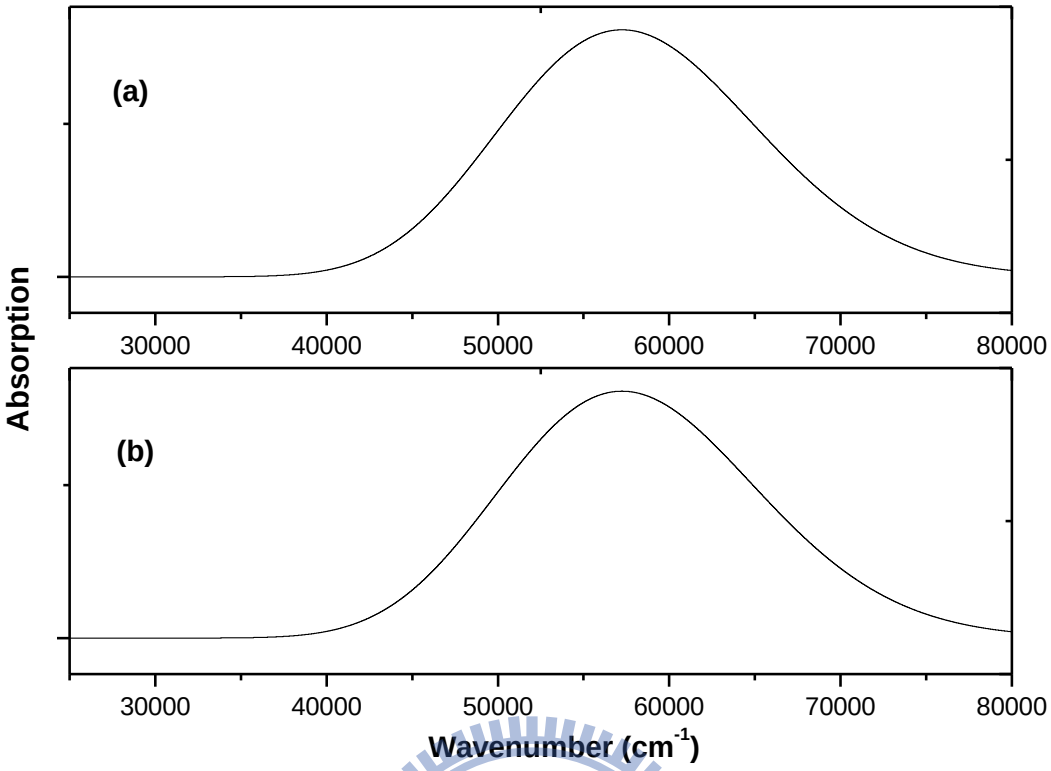

Fig. 43 **S**imulated absorption spectra of **HBDI** at 2K. (a) for r_{ba} = 5 cm^{-1} from B3LYP/TD-B3LYP calculation with no imaginary frequency, (b) for r_{ba} = 10 cm^{-1} from B3LYP/TD-B3LYP calculation with no imaginary frequency.

Without inhomogeneous broadening, a series of the simulated spectra in **Fig**. **44**, **45**, **46**, and **47** only shows the homogeneous broadening at low temperature (2K) which is chosen as 5 and 10 cm^{-1} without any scaling factors. No matter which the homogeneous parameter is chosen, the simulations still can't approach the experimental spectra. Detailed accounts of the simulation are given below.

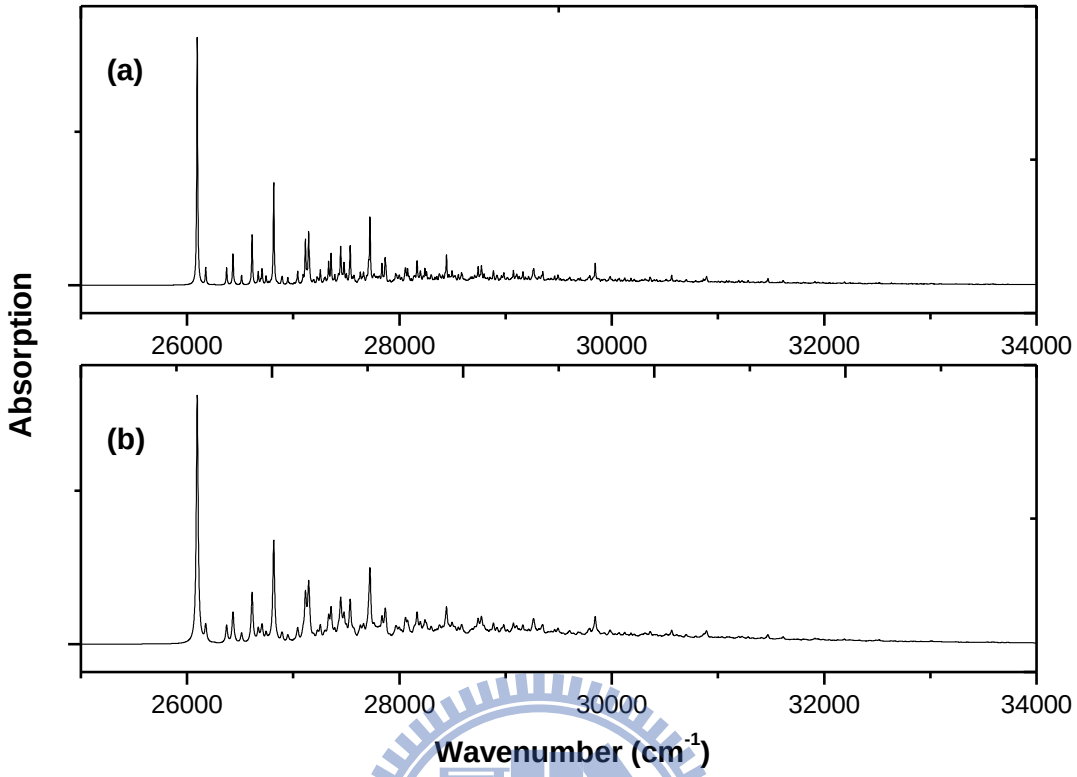

Fig. 44 **S**imulated absorption spectra of **HBDI** at 2K without scaling factor. (a) for r_{ba} = 5 cm^{-1} from B3LYP/TD-B3LYP calculation, (b) for r_{ba} = 10 cm^{-1} from B3LYP/TD-B3LYP calculation.

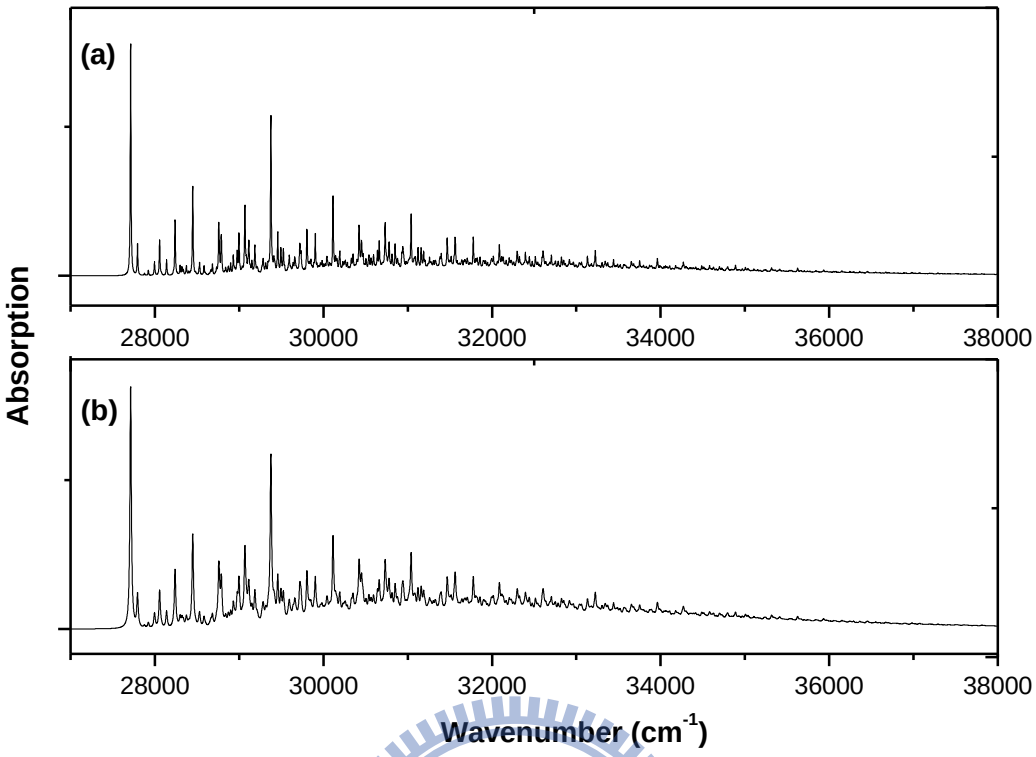

Fig. 45 **S**imulated absorption spectra of **HBDI** at 2K without scaling factor. (a) for r_{ba} = 5 cm^{-1} from B3LYP-35/TD-B3LYP-35 calculation, (b) for r_{ba} = 10 cm^{-1} from B3LYP-35/TD-B3LYP-35 calculation.

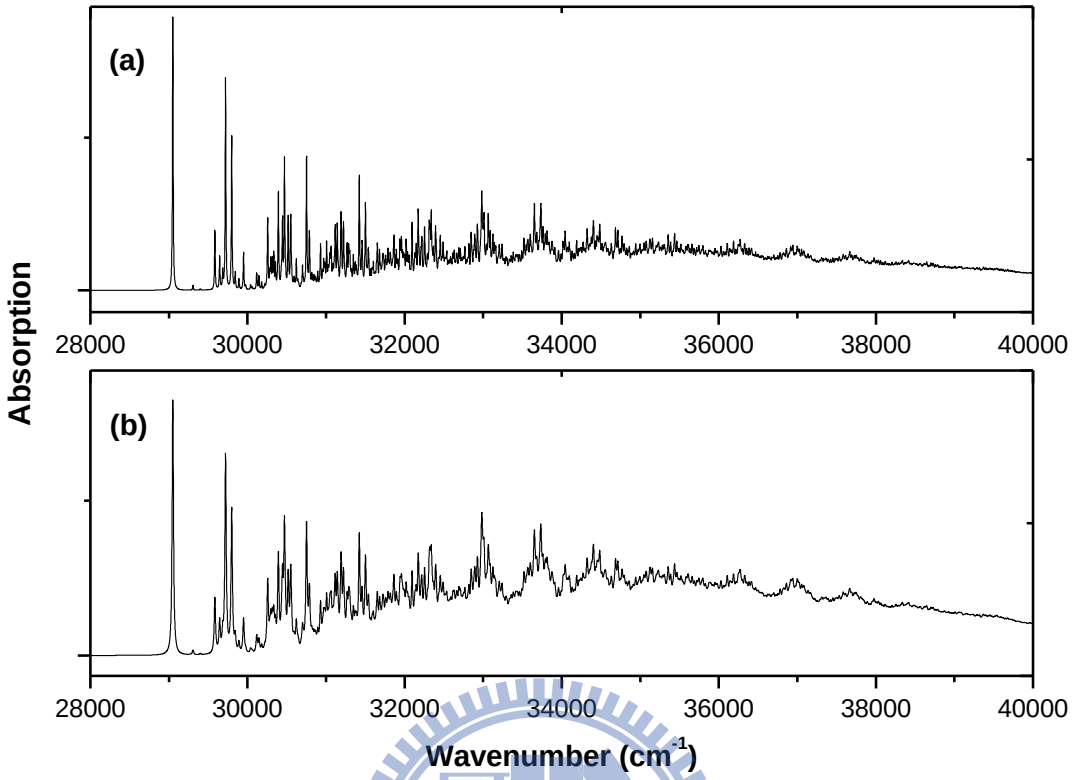

Fig. 46 **S**imulated absorption spectra of **HBDI** at 2K without scaling factor. (a) for r_{ba} = 5 cm^{-1} from BHandHLYP/TD-BHandHLYP calculation, (b) for r_{ba} = 10 cm^{-1} from BHandHLYP/TD-BHandHLYP calculation.

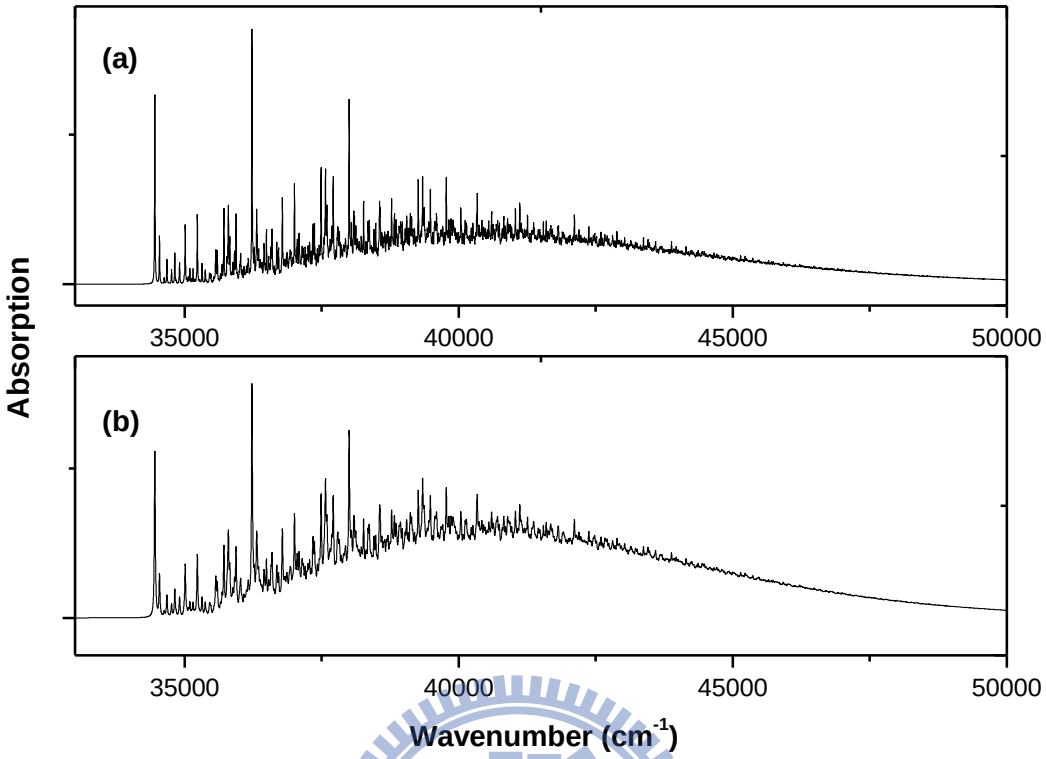

Fig. 47 **S**imulated absorption spectra of **HBDI** at 2K without scaling factor. (a) for r_{ba} = 5 cm^{-1} from HF/CIS calculation, (b) for r_{ba} = 10 cm^{-1} from HF/CIS calculation.

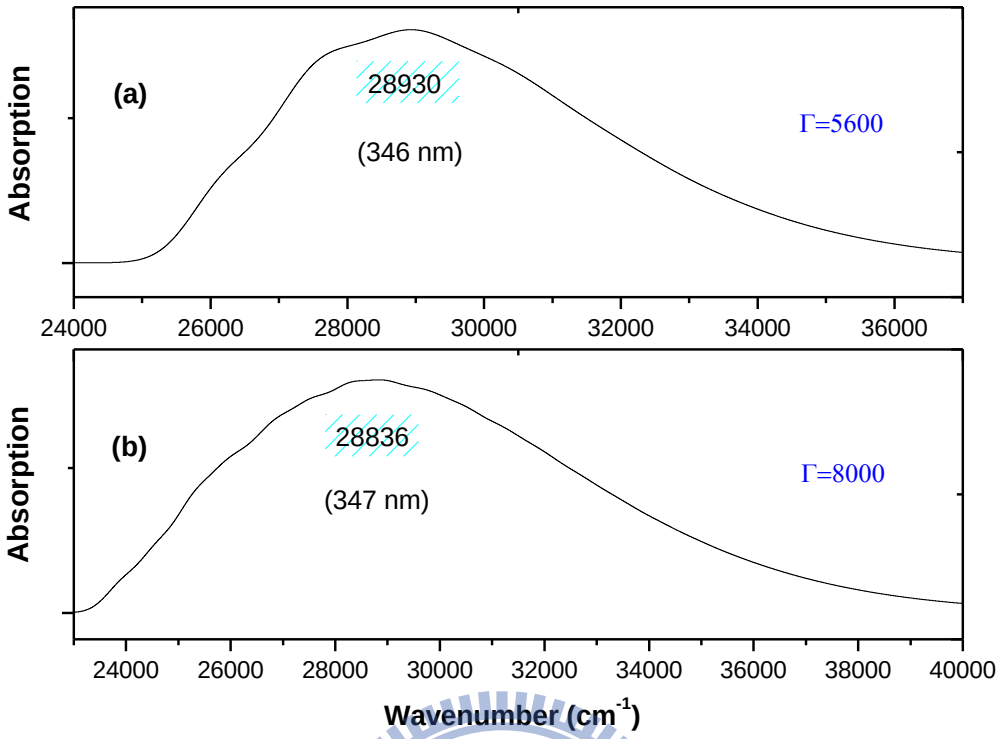

Fig. 48 Simulated absorption spectra of **HBDI** at 2K. (a) for r_{ba} = 5 cm^{-1}, and D_{ba} = 700 cm^{-1} from B3LYP-35/TD-B3LYP-35 calculation with scaling factor 0.94, (b) for r_{ba} = 10 cm^{-1}, and D_{ba} = 500 cm^{-1} from BHandHLYP/TD-BHandHLYP calculation with scaling factor 0.92.

Therefore, to sum up the findings from **Fig**. **44** to **47** are obtained as following: the more HF exchange is contained in DFT exchange-correlation functionals, the more blue shift is shown for the absorption spectra.

As **Fig. 48** indicates, absorption spectra of **HBDI** are **s**imulated at low temperature (2K) for homogeneous and inhomogeneous broadening simultaneously. Maximum absorption is at 28930 cm^{-1} (346 nm) for B3LYP-35/TD-B3LYP-35 calculation and 28836 cm^{-1} (347 nm) for BHandHLYP/TD-BHandHLYP calculation. Both of the absorption spectra for containing 35%, and 50% of HF exchange functionals are blue shift about 2000 cm^{-1} compared to the experimental spectrum in **Fig. 11(a)**.

4.1.7 Anharmonic Franck-Condon Simulation of Absorption and Fluorescence Spectra for C_1 Symmetry

As the early part mentioned above, harmonic Franck-Condon simulation of the absorption and fluorescence spectra have been shown. Hence, it follows from anharmonic Franck-Condon simulation which has been demonstrated for the first-order anharmonic correction to the wavefunction.

From **Fig. 49(b)**, the maximum absorption with PCM (Methanol, 410 nm) is still red shift about 2500 cm^{-1} compared to the experiment. But the maximum absorption for B3LYP/TD-B3LYP without PCM (372 nm) in **Fig. 11(c)** is almost the same as the experimental spectrum in **Fig. 49(a)** which is only red shift 35 cm^{-1}. For FWHM of these two simulations, the spectrum with PCM (Methanol) is nearly the same as the experimental spectrum but the spectrum for B3LYP/TD-B3LYP without PCM is smaller than the early harmonic Franck-Condon simulation (Γ = 4200).

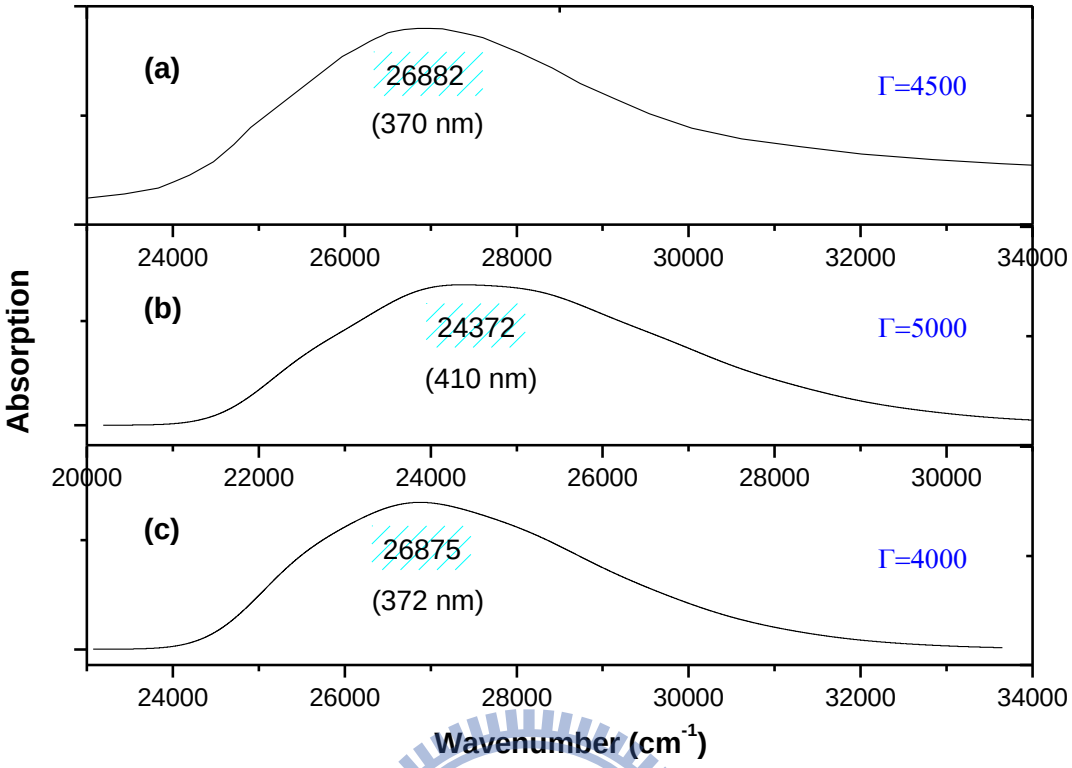

Fig. 49 **A**bsorption spectra of **HBDI** at 298K. (a) Experimental spectrum from Ref. [42], (b) anharmonic simulated spectrum for r_{ba} = 10 cm^{-1}, D_{ba} = 800 cm^{-1}, and the first-order anharmonic effect = 0.3 from B3LYP/TD-B3LYP with PCM (Methanol) calculation, (c) anharmonic simulated spectrum for r_{ba} = 10 cm^{-1}, D_{ba} = 800 cm^{-1}, and the first-order anharmonic effect = 0.3 from B3LYP/TD-B3LYP calculation,

All of the absorption spectra are blue shift because of considering the anharmonic Franck-Condon simulation. The spacing between anharmonic simulated absorption spectra of **HBDI** in methanol and acetonitrile solvents are increased slightly but the spacing of the absorption spectra in acetonitrile and THF solvents is getting closer (see **Fig. 50**).

However, maximum absorption of anharmonic spectrum changes from 24060 cm^{-1} to 24372 cm^{-1} for methanol solvent, from 24063 cm^{-1} to 24378 cm^{-1} for acetonitrile solvent, and from 24587 cm^{-1} to 24357 cm^{-1} for THF solvent. The spectral shift between harmonic and anharmonic Franck-Condon simulation for THF solvent is

only 230 cm^{-1} which is less than methanol and acetonitrile solvents. One of the factors may be the first-order anharmonic effect which is chosen as 0.3 for methanol and acetonitrile solvents but 0.25 for THF solvent.

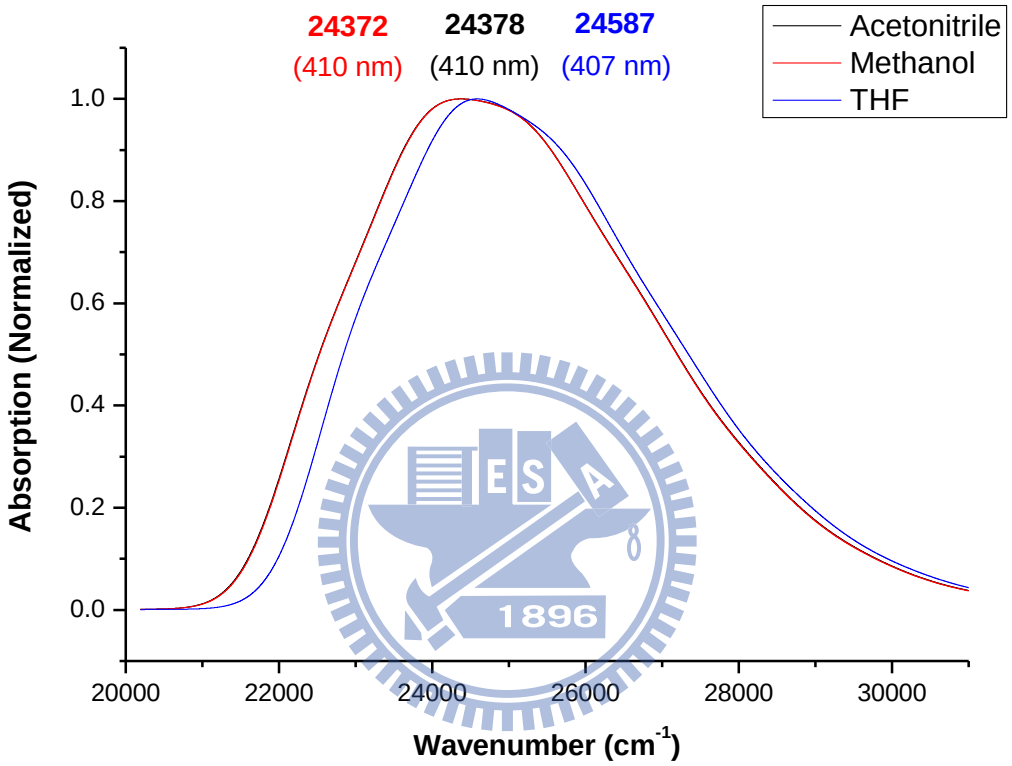

Fig. 50 Anharmonic simulated absorption spectra of **HBDI** in various solvents at 298K. (a) acetonitrile, (b) methanol, (c) THF. All the spectra were simulated for r_{ba} = 10 cm^{-1}, D_{ba} = 800 cm^{-1}, and the first-order anharmonic effect = 0.3 except THF (0.25).

Fig. 51(a) is the same experimental spectrum as **Fig. 13(a)**. Anharmonic Franck-Condon simulation of the fluorescence spectra shows the blue shift for all the spectra. So the red shift spectra compared to the experimental spectrum in harmonic Franck-Condon simulation may get the improvement but the blue shift ones won't.

Anharmonic Franck-Condon simulations of the fluorescence spectra with PCM (methanol) and without PCM for B3LYP/TD-B3LYP calculation are presented in **Fig. 51(b)** and **(c)**. The maximum fluorescence still shows blue shift ca. 2400 cm^{-1} which only improves 300 cm^{-1} compared to the harmonic Franck-Condon simulation for PCM (methanol). The previous blue shift one gives another 200 cm^{-1} blue shift for B3LYP/TD-B3LYP calculation. There is one other thing that is important for the spectra. The FWHM of PCM (methanol) and B3LYP/TD-B3LYP calculation are slightly larger than previous ones but the FWHM for B3LYP/TD-B3LYP calculation (Γ=4400 cm^{-1}) is still closer to the experimental spectrum.

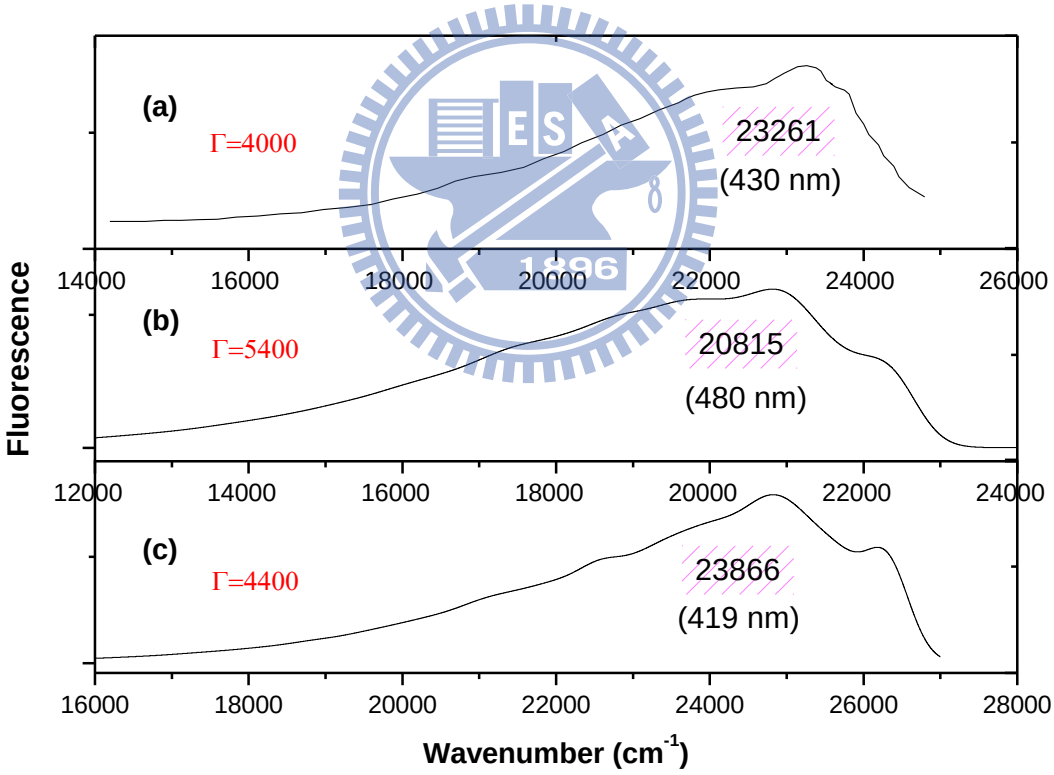

Fig. 51 Fluorescence spectra at 298K (a) Experimental spectrum from Ref. [42], (b) simulated spectrum for r_{ba} = 10 cm^{-1}, D_{ba} = 500 cm^{-1}, and the first-order anharmonic effect = 0.3 from B3LYP/TD-B3LYP with PCM (Methanol) calculation, (c) simulated spectrum for r_{ba} = 10 cm^{-1}, D_{ba} = 400 cm^{-1}, and the first-order anharmonic effect = 0.3 from B3LYP/TD-B3LYP calculation.

Another case of fluorescence is different experimental condition at 77K and its fluorescence spectrum is shown as **Fig. 52(a)** which is the same as **Fig. 14(a)**. The relative maxima are similar to the above case but the FWHM and the primary shoulder of PCM (THF, Γ=5300 cm^{-1}) are still in better agreement than B3LYP/TD-B3LYP without PCM calculation (Γ=4300 cm^{-1}).

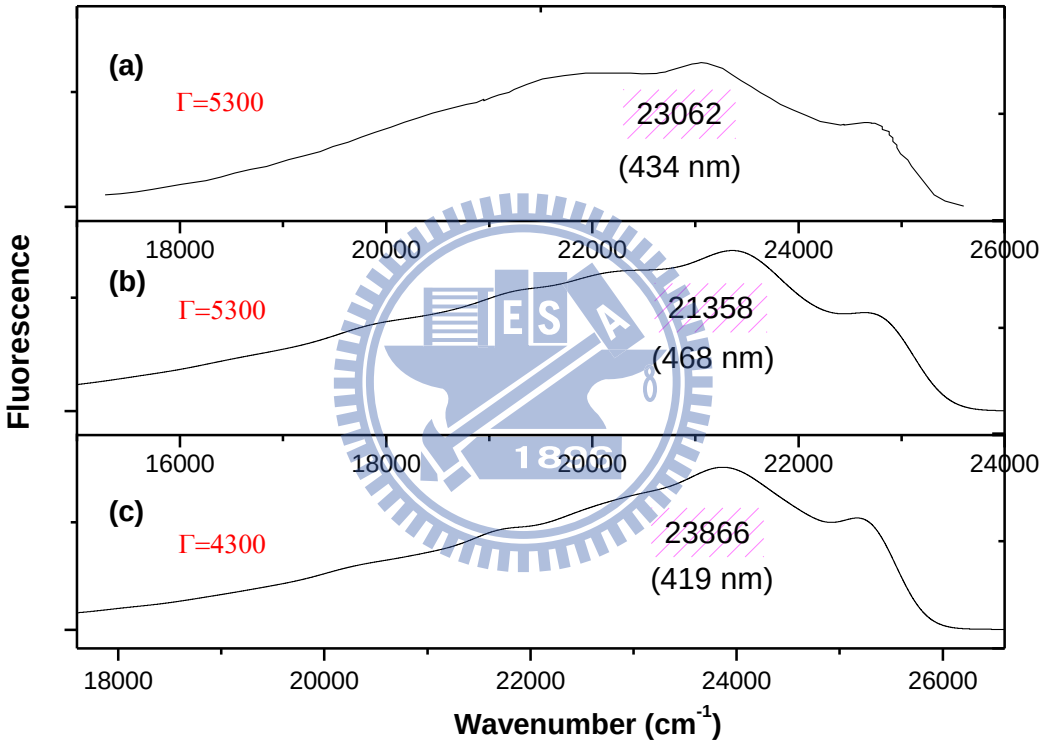

Fig. 52 Fluorescence spectra at 77K (a) Experimental spectrum from Ref. [16], (b) simulated spectrum for r_{ba} = 10 cm^{-1}, D_{ba} = 450 cm^{-1}, and the first-order anharmonic effect = 0.3 from B3LYP/TD-B3LYP with PCM (THF) calculation, (c) simulated spectrum for r_{ba} = 10 cm^{-1}, D_{ba} = 400 cm^{-1}, and the first-order anharmonic effect = 0.3 from B3LYP/TD-B3LYP calculation.

4.1.8 Excitation Energy and Oscillator Strength of HBDI for C_1 Symmetry

Both of the vertical and adiabatic excitation energies for TD-DFT and CIS calculations are shown in **Table 13** and TD-B3LYP with PCM (Acetonitrile, Methanol, and THF) results are also shown in **Table 14**. The vertical excitation energies from equilibrium S_0 to S_1 are larger than the adiabatic excitation energies from equilibrium S_0 to equilibrium S_1 vary from 0.21 eV to 0.43 eV. The more HF exchange is contained in DFT exchange-correlation functional, the higher the vertical and adiabatic excitation energies are. In other words, CIS method would get the highest value in these four methods not only the vertical excitation but also the adiabatic excitation.

For the different solvents of TD-B3LYP with PCM calculation in **Table 14**, nearly the same dielectric constants would obtain almost the same vertical and adiabatic excitation energies. Actually, all of the vertical and adiabatic excitation energies with PCM (Acetonitrile, Methanol, and THF) are lower than the values without PCM calculation. One explanation for this phenomenon may be that the solvent would stabilize the vibronic structures of S_0 and S_1.

Table 13 **V**ertical and adiabatic excitation energies (eV) for TD-B3LYP, TD-B3LYP-35, TD-BHandHLYP , and CIS calculations.

	Vertical energy	**Adiabatic energy**
TD-B3LYP	3.45	3.24 (26096 cm^{-1})
TD-B3LYP-35	3.70	3.44 (27713 cm^{-1})
TD-BHandHLYP	3.91	3.60 (29049 cm^{-1})
CIS	4.70	4.27 (34456 cm^{-1})

Table 14 **V**ertical and adiabatic excitation energies (eV) for TD- B3LYP with PCM (Acetonitrile, Methanol, and THF) calculations.

	Vertical energy	**Adiabatic energy**
PCM (Acetonitrile)	3.31	2.85 (22992 cm^{-1})
PCM (Methanol)	3.31	2.85 (23006 cm^{-1})
PCM (THF)	3.30	2.91 (23505 cm^{-1})

Table 15 presents the vertical excitation energies (eV) and oscillator strengths (*f*) for theoretical calculations in gas phase and various solvents. For the gas phase, the references report the transition of S_0 to S_1 was found at 359 nm (3.45eV) and 363 nm (3.42eV) [47, 48]. Another reference was reported 3.54 eV (*f* = 0.6975) and 3.46 eV (*f* = 0.6918) for the excitation energies in the gas phase with different basis set. And the PCM method for methanol solvent was considered which showed 3.35 eV (*f* = 0.8299) for excitation energy[49].

The vertical excitation energy for CIS calculation is 4.70 eV which is overestimated by 1.25 eV. But the results of TD-DFT show a better agreement with the previous studies (3.45 eV for TD-B3LYP//MP3 calculation and 3.42 eV for INDO/S-CIS calculation) especially for TD-B3LYP method (3.45 eV). In addition, semiempirical ZINDO approach validates the reliability with respect to quantum-mechanical DFT and HF methods.

When it is mentioned the results of ZINDO//B3LYP-35, BHandHLYP, and HF, the oscillator strengths are slightly different which are rather small to others. Because the energy level of the 1st and 2nd excited state are too close to each other. It means the geometry between the 1st and 2nd excited state only has a slight change. Actually, the better results in order of ZINDO// B3LYP-35, BHandHLYP, and HF are 3.49 eV (*f* = 0.9522), 3.54 eV (*f* = 0.9468), and 3.66 (*f* = 0.9365), respectively.

On the other hand, the vertical excitation energies and oscillator strengths do not

change too much compared with results of the gas phase among different solvents. As a matter of fact, all the vertical excitation energies with ZINDO method are generally smaller than TD-DFT and CIS method, but the oscillator strengths are opposite.

Table 15 Vertical excitation energies (eV) for previous studies, TD-DFT[a], CIS, and ZINDO methods. Oscillator strengths are provided in the brackets.

	Gas phase	**Solutions**		
		Acetonitrile	**Methanol**	**THF**
TD-B3LYP//MP3[b]	3.45			
INDO/S-CIS[c]	3.42			
TD-B3LYP	3.45 (0.6909)	3.31 (0.8069)	3.31 (0.8031)	3.30 (0.8214)
TD-B3LYP-35	3.70 (0.7646)	3.54 (0.8732)	3.55 (0.8696)	3.53 (0.8874)
TD-BHandHLYP	3.91 (0.8173)	3.76 (0.9223)	3.76 (0.9187)	3.75 (0.9363)
CIS[d]	4.70 (1.0785)	4.38 (1.2193)	4.39 (1.2152)	4.34 (1.2357)
ZINDO// B3LYP[e]	3.44 (0.9580)	3.02 (0.9598)	3.03 (0.9600)	2.99 (0.9628)
ZINDO// B3LYP-35[e]	3.48 (0.0010)	3.08 (0.9583)	3.10 (0.9583)	3.05 (0.9619)
ZINDO// BHandHLYP[e]	3.48 (0.0010)	3.14 (0.9565)	3.15 (0.9563)	3.11 (0.9608)
ZINDO// HF[e]	3.51 (0.0011)	3.27 (0.9565)	3.28 (0.9559)	3.24 (0.9629)

[a]TD-DFT calculation includes TD-B3LYP, TD-B3LYP-35, and TD-BHandHLYP functionals with 6-31+G(d) basis set.

[b]Calculation data is from Ref [48] with 6-311++G(d,p) basis set.

[c]Calculation data is from Ref. [47].

[d]CIS method with 6-31+G(d) basis set.

[e]ZINDO method for the S_0 optimized by B3LYP, B3LYP-35, BHandHLYP, and HF with 6-31+G(d) basis set.

4.2 HBI

4.2.1 Geometries of HBI for C_1 Symmetry

Previous case have demonstrated that simulate the geometries belonged to C_S symmetry may cause the broad width for the absorption and fluorescence spectra. For **HBI** case, we begin to discuss the influences C_1 symmetry on the absorption and fluorescence spectra.

By using the same methods previously with 6-31+G(d) basis set, optimized geometries are shown in **Fig. 53** For the calculation of gas phase, the bond lengths and angles in the S_0 phenol ring still seem to have similar values to the S_1 phenol ring. Both the bridge bonds 6C−12C and 12C−16C have single−double bond character between S_0 and S_1. But the bridge angle 6C−12C−16C reduces from 132.3˚ to 128.4˚. In the imidazolidinone ring, bond lengths and angles do not change too much as **HBDI** from S_0 to S_1. For the calculations of PCM (1,2-ethanediol, and water) method, the bridge bonds still have single−double bond character but the bridge angle reduces only 2.9˚. The changes in gas phase calculation are consistent with other results reported by Ref. [15].

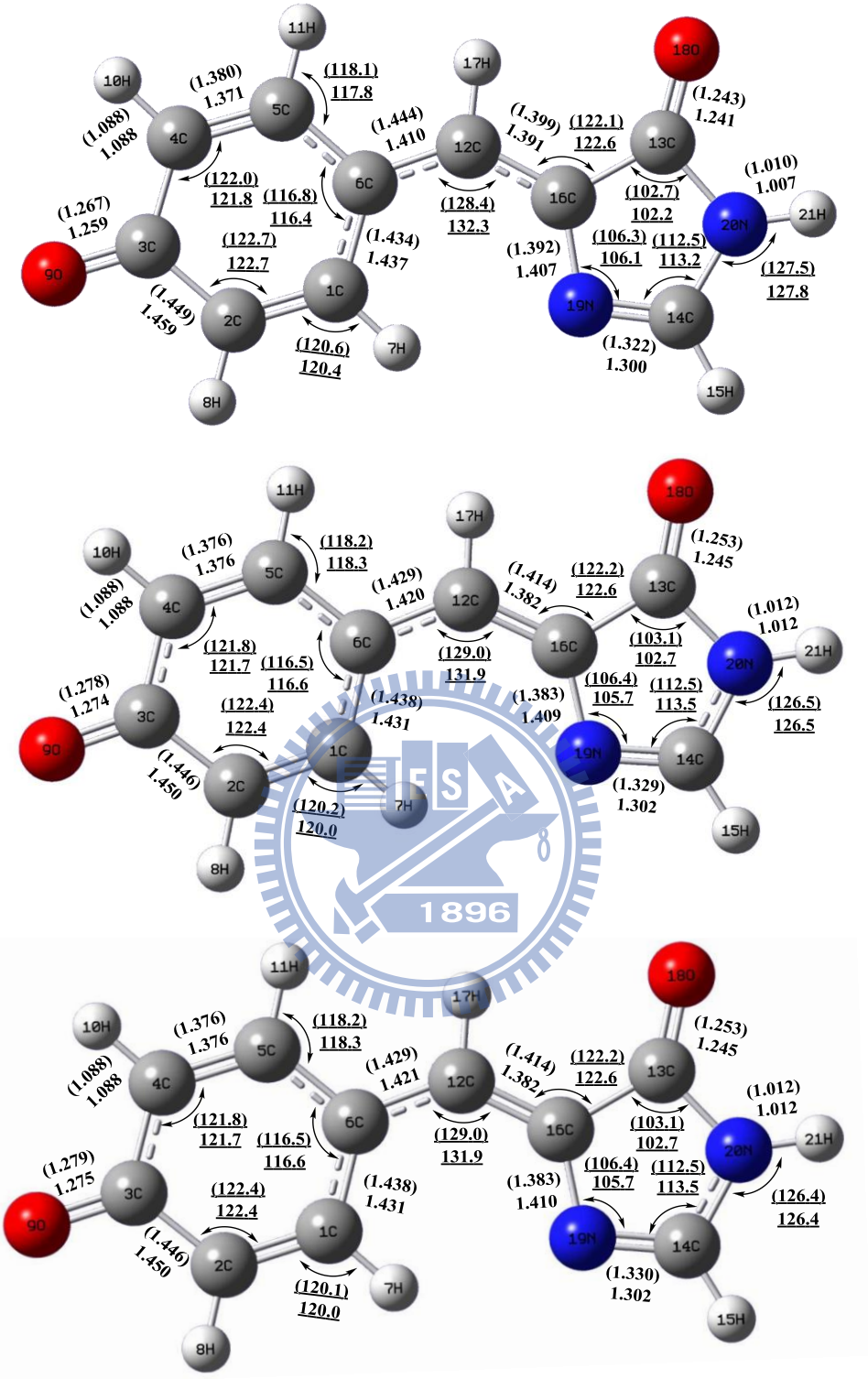

Fig. 53 B3LYP/6-31+G(d) and TD-B3LYP/6-31+G(d) optimized geometries of the S_0 and S_1 states for the anionic **HBI**. (Top) gas phase, (Middle) 1,2-ethanediol solvent for PCM calculation, and (Bottom) water solvent for PCM calculation. The bond lengths (bold, in angstrom) and angles (underline, in degree) of S_1 are provided in the brackets.

4.2.2 Vibrational Frequencies of HBI for C_1 Symmetry

The total number of vibrational modes is 57 in the anionic **HBI**. **Table 16** lists the corresponding vibrational modes between the experiment and calculations. The vibrational frequencies corresponding to hydrogen stretching modes are in the 2800−3700 cm^{-1} region such as C−H, N−H, and O−H stretching modes. The calculations of the present work are all overestimated for this region. In the 1000−2000 cm^{-1}, it is much more complex which is characterized by the modes of C−C, C−O, C−N bonds.

The calculated vibrational frequencies of S_0 and S_1 states and its corresponding Huang-Rhys factors are listed in **Table 17, 18, 19** and **20**. All 57 vibrational frequencies are shown no imaginary frequency in B3LYP/TD-B3LYP, B3LYP-35/TD-B3LYP-35, and BHandHLYP/TD-BHandHLYP calculations. Unfortunately, it is failed to calculate the vibrational frequencies of equilibrium S_1. But we still consider that it is also a displaced oscillator to simulate the spectra.

Table 16 Vibrational frequencies (cm^{-1}) in the region 1000−3600 cm^{-1} for experiment and calculations. The sacling factors are 0.9614 for B3LYP/6-31+G(d), 0.94 for B3LYP-35/6-31+G(d), 0.92 for BHandHLYP/6-31+G(d), and 0.8970 for HF/6-31+G(d), respectively.

CPMD[a]	Exp.[a]	B3LYP	B3LYP-35	BHandHLYP	HF
3445		3512	3507	3491	3513
3030		3096	3082	3063	3056
3015		3089	3075	3055	3053
3005		3055	3042	3023	3013
2985		3047	3035	3016	3005
2965		3023	3011	2993	2994
2945		3012	3001	2982	2973
1630	1630	1650	1659	1661	1630
1605	1577	1601	1608	1609	1609
1555	1556	1558	1560	1561	1583
1510	1535	1533	1544	1552	
1490	1501	1510	1513	1502	1491
1445	1439	1432	1435	1433	1435
1405		1401	1403	1401	1416
1330		1340	1340	1335	1341
1310	1315	1310	1306	1300	1309
1245	1263	1270	1273	1272	1258
	1229	1229	1228	1224	1231
1145	1172	1155	1158	1160	1178
1125		1140	1136	1128	1129
1060	1095	1071	1071	1068	1083
1020		1020	1027	1027	1034

[a]Results from Ref. [50] by using Car-Parrinello molecular dynamics simulation (CPMD).

Table 17 Unscaled calculated vibrational frequencies of S_0 (ω_j, cm^{-1}) and S_1 (ω'_j, cm^{-1}) with C_1 symmetry using B3LYP/TD-B3LYP method. The corresponding Huang-Rhys factors (S^{HF}, dimensionless) and the 3rd derivative of S_0 potential energy surface (K_{j3}, Hartree*amu$^{-3/2}$*Bohr^{-3}) are also shown.

Mode	ω_j	ω'_j	S^{HF}	K_{j3}	Mode	ω_j	ω'_j	S^{HF}	K_{j3}
1	3653	3649	0.0150	-1.79075	**30**	949	882	0.0000	0.00000
2	3220	3243	0.0001	1.26535	**31**	913	839	0.0182	-0.00584
3	3213	3213	0.0012	1.17775	**32**	862	832	0.0000	0.00000
4	3177	3180	0.0010	-1.09162	**33**	859	821	0.0148	0.00206
5	3169	3176	0.0021	1.10660	**34**	825	768	0.0120	-0.00504
6	3144	3171	0.2425	-1.06243	**35**	804	766	0.0056	0.00200
7	3133	3134	0.0044	-0.87561	**36**	799	762	0.0000	0.00000
8	1716	1683	0.2370	0.09059	**37**	786	720	0.0000	0.00000
9	1666	1591	0.0004	-0.03632	**38**	746	686	0.0000	0.00000
10	1620	1548	0.0001	0.00731	**39**	733	664	0.0000	0.00000
11	1595	1497	0.1321	-0.03592	**40**	689	615	0.0915	-0.00121
12	1571	1482	0.4598	-0.04288	**41**	661	613	0.0000	0.00000
13	1539	1449	0.1290	0.00282	**42**	622	568	0.0037	0.00000
14	1491	1428	0.3722	-0.00800	**43**	589	536	0.1656	-0.00038
15	1457	1399	0.0023	0.00552	**44**	521	502	0.0000	0.00000
16	1403	1390	0.0047	0.00030	**45**	483	472	0.1464	0.00007
17	1394	1338	0.1187	0.01455	**46**	479	448	0.0000	0.00000
18	1363	1305	0.2055	0.00107	**47**	457	435	0.4014	-0.00013
19	1322	1288	0.3203	-0.01054	**48**	429	381	0.0000	0.00000
20	1296	1262	0.0235	-0.00242	**49**	384	272	0.0000	0.00000
21	1279	1220	0.1929	0.00000	**50**	284	266	0.0138	0.00014
22	1201	1201	0.0062	0.00208	**51**	272	262	0.0000	0.00000
23	1186	1111	0.0045	-0.00114	**52**	214	204	0.0341	-0.00004
24	1114	1082	0.0003	-0.00199	**53**	205	187	0.0000	0.00000
25	1080	1069	0.0085	0.00806	**54**	136	122	0.0000	0.00000
26	1061	1007	0.1324	0.00692	**55**	98	103	0.5081	-0.00004
27	1003	966	0.0000	0.00000	**56**	67	49	0.0000	0.00000
28	990	945	0.0004	0.00030	**57**	59	37	0.0000	0.00000
29	976	919	0.0000	0.00000					

Table 18 Unscaled calculated vibrational frequencies of S_0 (ω_j, cm^{-1}) and S_1 (ω'_j, cm^{-1}) with C_1 symmetry using B3LYP-35/TD-B3LYP-35 method. The corresponding Huang-Rhys factors (S^{HF}, dimensionless) and the 3rd derivative of S_0 potential energy surface (K_{j3}, Hartree*amu$^{-3/2}$*Bohr^{-3}) are also shown.

Mode	ω_j	ω'_j	S^{HF}	K_{j3}	Mode	ω_j	ω'_j	S^{HF}	K_{j3}
1	3731	3728	0.0171	1.85049	**30**	979	910	0.0000	0.00000
2	3279	3302	0.0000	1.29961	**31**	934	862	0.0212	0.00608
3	3271	3274	0.0009	1.20777	**32**	882	862	0.0000	0.00000
4	3236	3238	0.0015	-1.12650	**33**	879	837	0.0193	-0.00222
5	3228	3236	0.0035	1.14054	**34**	841	800	0.0087	-0.00538
6	3203	3229	0.2752	-1.08580	**35**	825	796	0.0000	0.00000
7	3192	3195	0.0052	-0.89134	**36**	821	781	0.0098	0.00176
8	1765	1732	0.2956	0.09512	**37**	816	739	0.0000	0.00000
9	1711	1648	0.0010	0.03912	**38**	774	704	0.0000	0.00000
10	1660	1599	0.0065	0.00232	**39**	746	687	0.0000	0.00000
11	1643	1539	0.4738	0.04818	**40**	706	652	0.1037	-0.00118
12	1609	1520	0.3162	-0.01680	**41**	678	627	0.0000	0.00000
13	1576	1491	0.1504	-0.00082	**42**	634	588	0.0118	0.00000
14	1527	1465	0.5497	-0.00845	**43**	603	576	0.2227	0.00038
15	1493	1438	0.0027	-0.00496	**44**	530	510	0.0000	0.00000
16	1437	1426	0.0051	-0.00842	**45**	493	485	0.1368	-0.00005
17	1426	1379	0.1112	0.00625	**46**	491	459	0.0000	0.00000
18	1390	1331	0.2118	0.00105	**47**	467	458	0.4839	-0.00013
19	1354	1324	0.3932	0.00983	**48**	442	390	0.0000	0.00000
20	1326	1287	0.0386	0.00243	**49**	395	281	0.0000	0.00000
21	1307	1253	0.2630	0.00000	**50**	289	279	0.0222	0.00014
22	1233	1230	0.0128	-0.00172	**51**	276	268	0.0000	0.00000
23	1209	1138	0.0020	0.00273	**52**	218	210	0.0512	0.00005
24	1139	1110	0.0024	0.00213	**53**	212	197	0.0000	0.00000
25	1107	1107	0.0231	-0.00400	**54**	138	119	0.0000	0.00000
26	1092	1063	0.1016	-0.00139	**55**	100	106	0.6052	-0.00005
27	1031	991	0.0000	0.00000	**56**	68	49	0.0000	0.00000
28	1009	976	0.0001	0.00030	**57**	60	40	0.0000	0.00000
29	1007	971	0.0000	0.00000					

Table 19 Unscaled calculated vibrational frequencies of S_0 (ω_j, cm^{-1}) and S_1 (ω'_j, cm^{-1}) with C_1 symmetry using BHandHLYP/TD-BHandHLYP method. The corresponding Huang-Rhys factors (S^{HF}, dimensionless) and the 3rd derivative of S_0 potential energy surface (K_{j3}, Hartree*$amu^{-3/2}$*$Bohr^{-3}$) are also shown.

Mode	ω_j	ω'_j	S^{HF}	K_{j3}	Mode	ω_j	ω'_j	S^{HF}	K_{j3}
1	3796	3792	0.0192	-1.89954	**30**	1006	936	0.0000	0.00000
2	3329	3352	0.0000	1.32914	**31**	952	884	0.0226	-0.00633
3	3321	3326	0.0005	1.23316	**32**	899	882	0.0000	0.00000
4	3286	3288	0.0016	-1.15391	**33**	895	851	0.0231	0.00235
5	3278	3286	0.0044	1.16780	**34**	859	822	0.0000	0.00000
6	3253	3278	0.3023	-1.10703	**35**	854	815	0.0055	0.00571
7	3242	3245	0.0062	-0.90642	**36**	836	798	0.0132	0.00156
8	1805	1777	0.3119	0.09834	**37**	833	757	0.0000	0.00000
9	1749	1698	0.0019	-0.04296	**38**	797	718	0.0000	0.00000
10	1697	1642	0.0408	-0.00397	**39**	757	704	0.0000	0.00000
11	1687	1577	0.7267	-0.06340	**40**	720	686	0.1195	-0.00117
12	1633	1555	0.2335	0.00806	**41**	693	637	0.0000	0.00000
13	1606	1525	0.1353	-0.00266	**42**	644	603	0.0156	0.00000
14	1557	1495	0.7391	-0.00875	**43**	614	601	0.2695	-0.00039
15	1523	1475	0.0021	0.00485	**44**	538	516	0.0000	0.00000
16	1466	1455	0.0238	0.01353	**45**	501	495	0.1340	0.00004
17	1451	1417	0.1009	-0.00307	**46**	501	475	0.0000	0.00000
18	1413	1359	0.1899	0.00125	**47**	475	466	0.5375	-0.00014
19	1383	1355	0.4854	-0.00922	**48**	453	397	0.0000	0.00000
20	1352	1306	0.0480	-0.00228	**49**	403	286	0.0000	0.00000
21	1331	1284	0.3283	0.00000	**50**	294	284	0.0268	-0.00015
22	1261	1255	0.0222	0.00206	**51**	278	266	0.0000	0.00000
23	1226	1170	0.0006	-0.00336	**52**	221	215	0.0676	-0.00005
24	1161	1153	0.0055	-0.00236	**53**	217	202	0.0000	0.00000
25	1129	1131	0.0636	0.00181	**54**	140	114	0.0000	0.00000
26	1116	1107	0.0560	-0.01229	**55**	102	109	0.6881	-0.00005
27	1057	1009	0.0000	0.00000	**56**	69	49	0.0000	0.00000
28	1035	1005	0.0000	0.00000	**57**	61	39	0.0000	0.00000
29	1027	996	0.0000	0.00029					

Table 20 Unscaled calculated vibrational frequencies of S_0 (ω_j, cm^{-1}) and S_1 (ω'_j, cm^{-1}) with C_1 symmetry using HF/CIS method. The corresponding Huang-Rhys factors (S^{HF}, dimensionless) and the 3rd derivative of S_0 potential energy surface (K_{j3}, Hartree*amu$^{-3/2}$*Bohr^{-3}) are also shown.

Mode	ω_j	ω'_j	S^{HF}	K_{j3}	Mode	ω_j	ω'_j	S^{HF}	K_{j3}
1	3917		0.0221	-1.98118	**30**	1062		0.0001	0.00000
2	3407		0.0007	1.36032	**31**	981		0.0164	-0.00695
3	3404		0.0006	1.27875	**32**	958		0.0062	0.00000
4	3358		0.0028	-1.14777	**33**	936		0.0031	0.00000
5	3351		0.0075	1.21376	**34**	920		0.0507	0.00284
6	3338		0.3422	-1.21609	**35**	870		0.0047	0.00000
7	3315		0.0003	-1.02072	**36**	867		0.0014	-0.00550
8	1876		0.3553	0.10357	**37**	861		0.0236	0.00426
9	1817		0.0099	-0.05654	**38**	848		0.0291	0.00000
10	1794		1.0534	-0.10354	**39**	783		0.0220	0.00000
11	1765		0.0187	0.00425	**40**	749		0.1229	-0.00125
12	1663		0.1947	0.02402	**41**	721		0.0037	0.00000
13	1648		0.0346	-0.00692	**42**	665		0.0261	-0.00008
14	1599		0.8309	0.00254	**43**	636		0.3712	-0.00045
15	1579		0.0001	0.00424	**44**	552		0.0297	0.00000
16	1535		0.0655	0.01512	**45**	520		0.1051	0.00000
17	1495		0.0576	0.00589	**46**	518		0.0190	0.00000
18	1459		0.0152	-0.00382	**47**	496		0.6519	-0.00016
19	1441		1.0781	-0.00039	**48**	472		0.0012	0.00000
20	1402		0.0425	0.00052	**49**	418		0.0014	0.00000
21	1372		0.3320	0.00064	**50**	303		0.0228	-0.00015
22	1313		0.0212	0.00373	**51**	276		0.0064	0.00000
23	1258		0.0001	-0.00655	**52**	229		0.0719	-0.00006
24	1208		0.0133	-0.00257	**53**	223		0.0669	0.00000
25	1172		0.1338	0.00201	**54**	142		0.0465	0.00000
26	1153		0.0396	-0.02221	**55**	105		0.8061	-0.00005
27	1125		0.0021	0.00000	**56**	70		0.0025	0.00000
28	1112		0.0652	0.00000	**57**	61		0.0572	0.00000
29	1080		0.0076	0.00000					

4.2.3 Absorption Spectra of HBI for C_1 Symmetry

The absorption spectrum of anionic **wt-GFP** from Ref. [13] exhibits several weak vibronic structures in 50% glycerol/50% buffer (pH 6.5, 10 mM phosphate) at 77K in **Fig. 54(a)**. **Fig. 54(b), (c), (d),** and **(e)** present the simulations for B3LYP/TD-B3LYP, B3LYP-35/TD-B3LYP-35, BHandHLYP/TD-BHandHLYP, and HF/CIS calculations. Only B3LYP/TD-B3LYP method shows a better simulation with the experiment of all but the band width is about 1.5 times larger than the experimental spectrum. In the case of anionic **HBI**, we only try this method to consider the solvent effects by using PCM calculations. The solvents are acetonitrile (CH_3CN, $\mathcal{E}$ = 35.69), 1,2-ethanediol ($HOCH_2CH_2OH$, $\mathcal{E}$ = 40.245), and water (H_2O, $\mathcal{E}$ = 78.3553).

From **Fig. 55(b), (c),** and **(d)**, the results of the PCM simulation do not change too much compared with B3LYP/TD-B3LYP method. It is still disagreement with the experiment spectrum for different solvent simulation. So the strategy is trying to optimize the anionic **wt-GFP** geometry. We want to figure out why the simulations do not match with the experiment spectrum.

The procedures of the simulation are shown in **Fig. 56**. The homogeneous parameter r_{ba} is chosen as 5 cm^{-1} but the inhomogeneous parameter D_{ba} varies from 15 to 500 cm^{-1}. It is obvious that when inhomogeneous parameter becomes larger, the middle of the spectrum would grow higher which is far away to the experimental spectrum.

This problem which is failed to simulate an agreement with the experiment will be taken up in the next section. In the next section, the anionic **wt-GFP** would be attempted to the simulated spectra for the further discussion.

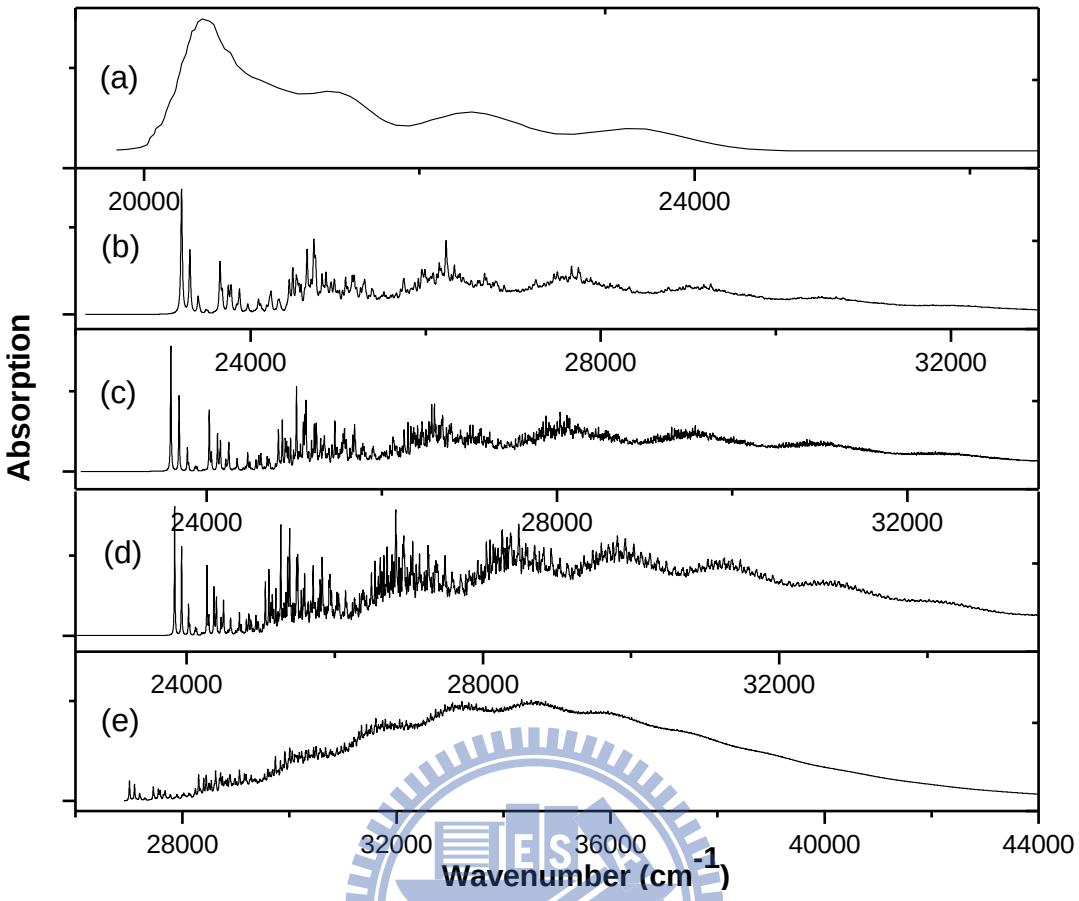

Fig. 54 Absorption spectra of the anionic **HBI** at 77K. (a) Experiment spectrum from Ref. [13], (b) simulated spectrum for r_{ba} = 10 cm^{-1} from B3LYP/TD-B3LYP calculation, (c) simulated spectrum for r_{ba} = 5 cm^{-1} from B3LYP-35/TD-B3LYP-35 calculation, (d) simulated spectrum for r_{ba} = 5 cm^{-1} from BHandHLYP/TD-BHandHLYP calculation, (E) simulated spectrum for r_{ba} = 5 cm^{-1} from HF/CIS calculation.

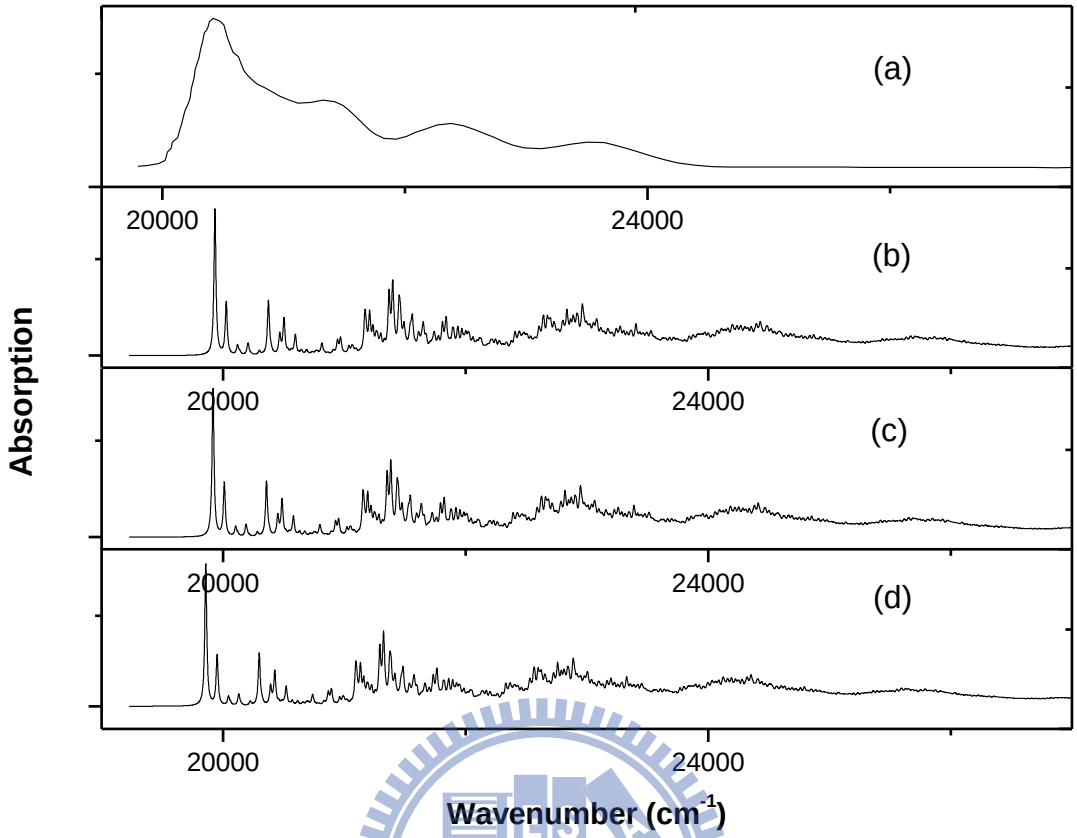

Fig. 55 Absorption spectra of the anionic **HBI** at 77K for PCM method. (a) Experiment spectrum from Ref. [13], (b) simulated spectrum for r_{ba} = 10 cm^{-1} from B3LYP/TD-B3LYP with PCM (acetonitrile) calculation, (c) simulated spectrum for r_{ba} = 10 cm^{-1} from B3LYP/TD-B3LYP with PCM (1,2-ethanediol) calculation, (d) simulated spectrum for r_{ba} = 10 cm^{-1} from B3LYP/TD-B3LYP with PCM (water) calculation.

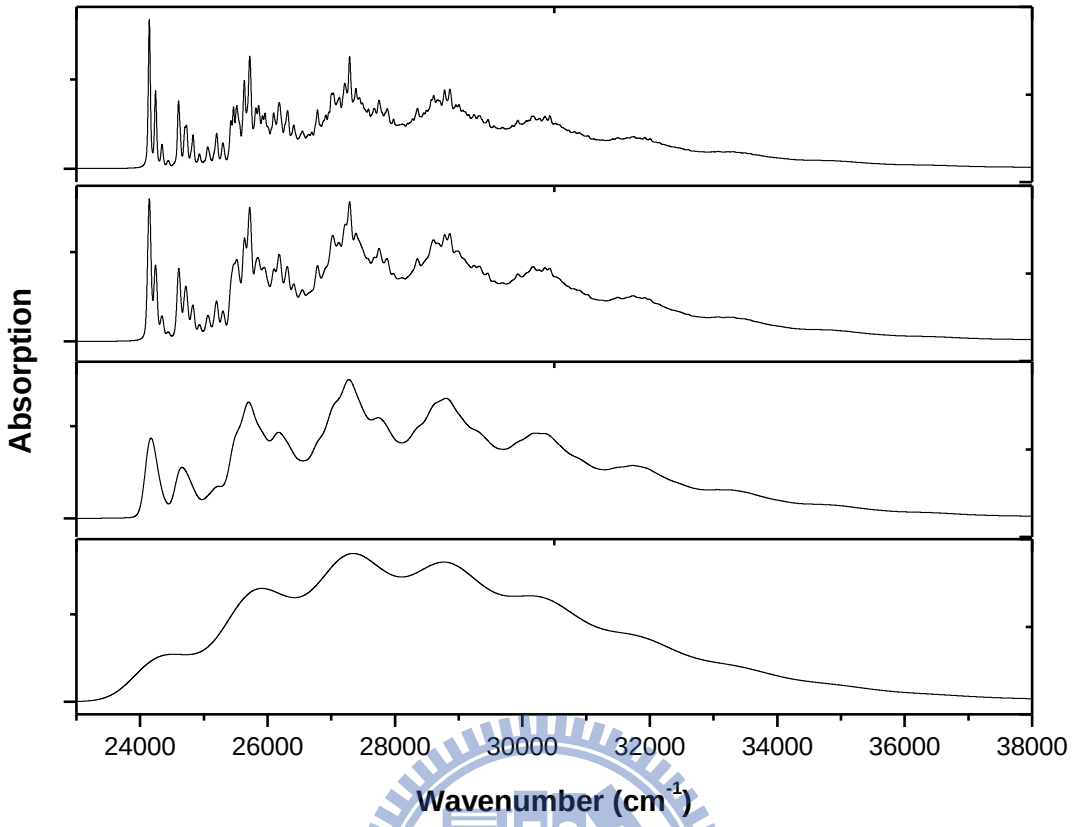

Fig. 56 Simulated absorption spectra of the anionic **HBI** at 77K. (a) for r_{ba} = 5 cm^{-1}, and D_{ba} = 15 cm^{-1} from B3LYP/TD-B3LYP calculation, (b) for r_{ba} = 5 cm^{-1}, and D_{ba} = 30 cm^{-1} from B3LYP/TD-B3LYP calculation, (c) for r_{ba} = 5 cm^{-1}, and D_{ba} = 100 cm^{-1} from B3LYP/TD-B3LYP calculation, (d) for r_{ba} = 5 cm^{-1}, and D_{ba} = 500 cm^{-1} from B3LYP/TD-B3LYP calculation.

4.2.4 Excitation Energy and Oscillator Strength of HBI for C_1 Symmetry

Both TD-DFT and CIS calculations estimated the vertical and adiabatic excitation energies which are shown in **Table 21** and TD-B3LYP with PCM (Acetonitrile, 1,2-ethanediol, and water) results are also shown in **Table 22**. The vertical excitation energies from equilibrium S_0 to S_1 are larger than the adiabatic excitation energies from equilibrium S_0 to equilibrium S_1 slightly vary from 0.07 eV to 0.11 eV. The more

HF exchange is contained in DFT exchange-correlation functional, the higher the vertical and adiabatic excitation energies are. Also, in other words, CIS method would get the highest value in these four methods not only the vertical excitation but also the adiabatic excitation. TD-DFT and CIS calculations of vertical and adiabatic excitation energies are all slightly larger than the results of Ref. [15] in anionic **HBI**.

Table 21 Vertical and adiabatic excitation energies (eV) for TD-B3LYP, TD-B3LYP-35, TD-BHandHLYP , and CIS calculations.

	Vertical energy	**Adiabatic energy**
CASPT2[a]	2.67	2.52 (20349 cm^{-1})
TD-B3LYP	3.06	2.99 (24144 cm^{-1})
TD-B3LYP-35	3.19	3.11 (25095 cm^{-1})
TD-BHandHLYP	3.29	3.21 (25912 cm^{-1})
CIS	3.84	3.73 (30111 cm^{-1})

[a]Calculation data is from Ref. [15] with 6-31+G(d) basis set.

For the different solvents of TD-B3LYP with PCM calculation in **Table 22,** all of the vertical and adiabatic excitation energies with PCM (Acetonitrile, 1,2-ethanediol, and water) are lower than the values without PCM calculation. One may notice that the vertical and adiabatic excitation energies within PCM calculations would be improved to close the results in other study such as 2.95 eV and 2.57 eV in acetonitrile solvent versus 2.67 eV and 2.52 eV for CASPT2 calculation, respectively.

Table 22 Vertical and adiabatic excitation energies (eV) for TD- B3LYP with PCM (Acetonitrile, 1,2-ethanediol, and water) calculations.

	Vertical energy	**Adiabatic energy**
PCM (Acetonitrile)	2.95 (1.0377)	2.57 (20735 cm^{-1})
PCM (1,2-ethanediol)	2.92 (1.0617)	2.57 (20718 cm^{-1})
PCM (Water)	2.95 (1.0332)	2.56 (20656 cm^{-1})

Table 23 summarizes the vertical excitation energies (eV) and oscillator strengths (*f*) for theoretical calculations in gas phase. The vertical excitation energy for CIS and TD-DFT calculation is overestimated but the results of ZINDO show a better agreement with the reported studies (2.60, 2.62, 2.64, and 2.66 eV for ZINDO// B3LYP, B3LYP-35, BHandHLYP, and HF calculation verse 2.67 eVfor CASPT2 calculation, respectively).

Table 23 Vertical excitation energies (eV) for previous studies, TD-DFT[a], CIS, and ZINDO methods. Oscillator strengths are provided in the brackets.

	Gas phase
CASPT2[b]	2.67
TD-B3LYP	3.06 (0.9076)
TD-B3LYP-35	3.19 (0.9818)
TD-BHandHLYP	3.29 (1.0426)
CIS	3.84 (1.4534)
ZINDO// B3LYP[c]	2.60 (1.2084)
ZINDO// B3LYP-35[c]	2.62 (1.2075)
ZINDO// BHandHLYP[c]	2.64 (1.2060)
ZINDO// HF[c]	2.66 (1.2065)

[a]TD-DFT calculation includes TD-B3LYP, TD-B3LYP-35, and TD-BHandHLYP functionals with 6-31+G(d) basis set.

[b]Calculation data is from Ref. [15] with 6-31+G(d) basis set.

[c]ZINDO method for the S_0 optimized by B3LYP, B3LYP-35, BHandHLYP, and HF with 6-31+G(d) basis set.

4.3 wt-GFP

4.3.1 Geometries of wt-GFP for C_1 Symmetry

The B3LYP/TD-B3LYP method optimized geometries is shown in **Fig. 57** which displayed a huge system. It may increase the computational cost for such a huge molecule. If we want an efficient calculation for a bigger molecular, the strategy for optimization is using the semiempirical method (AM1, PM3 etc) first. Then we can use the semiempirical optimized geometry for B3LYP/TD-B3LYP initial geometrical guess.

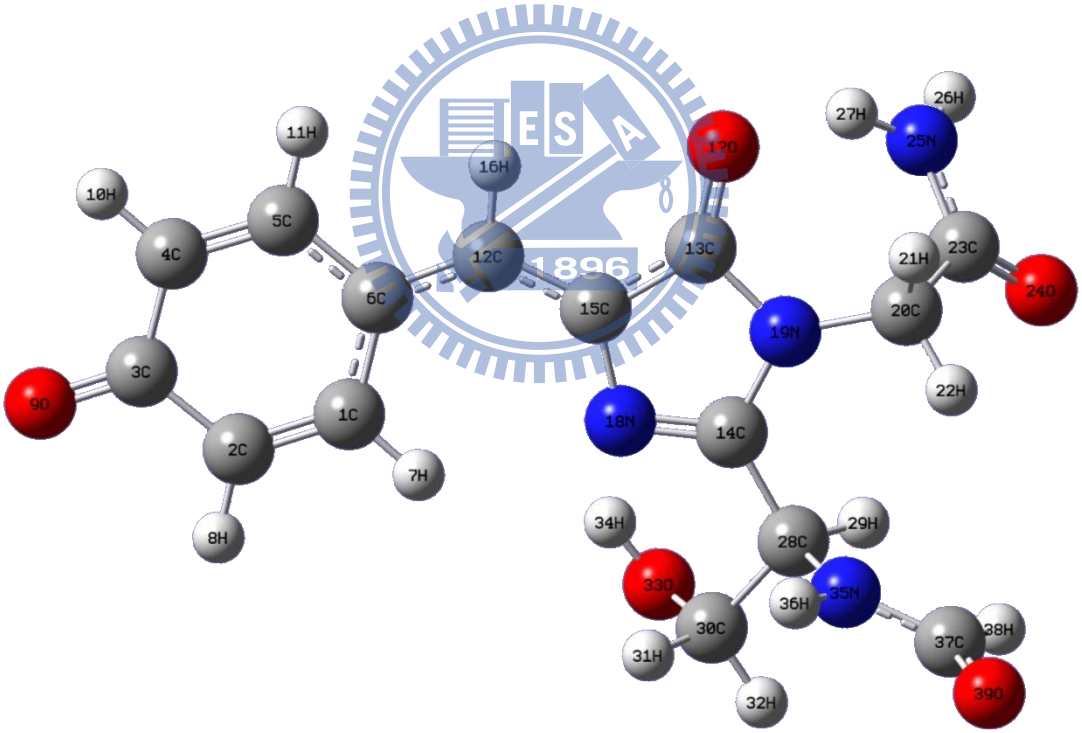

Fig. 57 B3LYP/6-31+G(d) and TD-B3LYP/6-31+G(d) optimized geometries of the S_0 and S_1 states for the anionic form of the **wt-GFP** in gas phase.

4.3.2 Absorption Spectra of wt-GFP for C_1 Symmetry

The simulation spectrum of the anionic **wt-GFP** presents a large broad width compared with the experiment spectrum (see **Fig. 58**). Similarly, it does not match with the experiment.

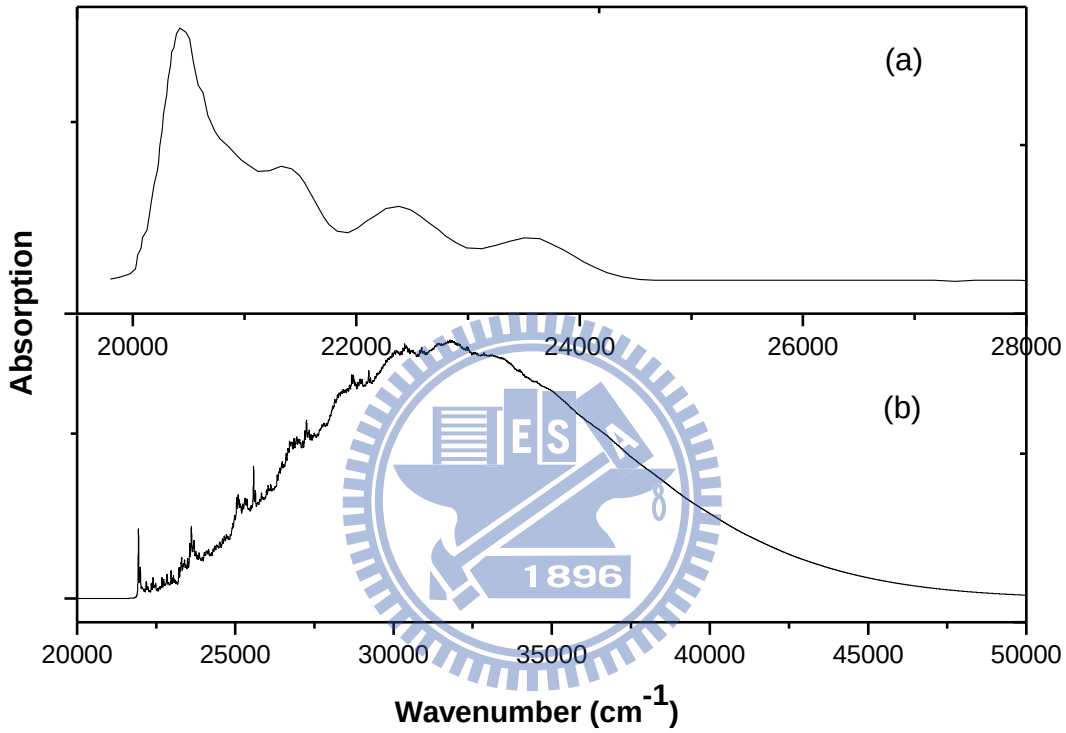

Fig. 58 Absorption spectra of the anionic form of the **wt-GFP** at 77K. (a) Experiment spectrum from Ref. [13], (b) simulated spectrum for r_{ba} = 10 cm^{-1} from B3LYP/TD-B3LYP calculation.

4.4 HBMPI

4.4.1 Geometries of HBMPI for C_1 Symmetry

B3LYP/TD- B3LYP methods with 6-31+G(d) basis set optimized geometries are shown in **Fig. 59** For the calculation of gas phase, the bond lengths and angles in the S_0 and S_1 phenol ring and imidazolidinone ring have similar values. Both the bridge bonds 4C−12C and 12C−14C have single−double bond character between S_0 and S_1. But the bridge angle 4C−12C−14C reduces from 132.0˚ to 128.9˚.

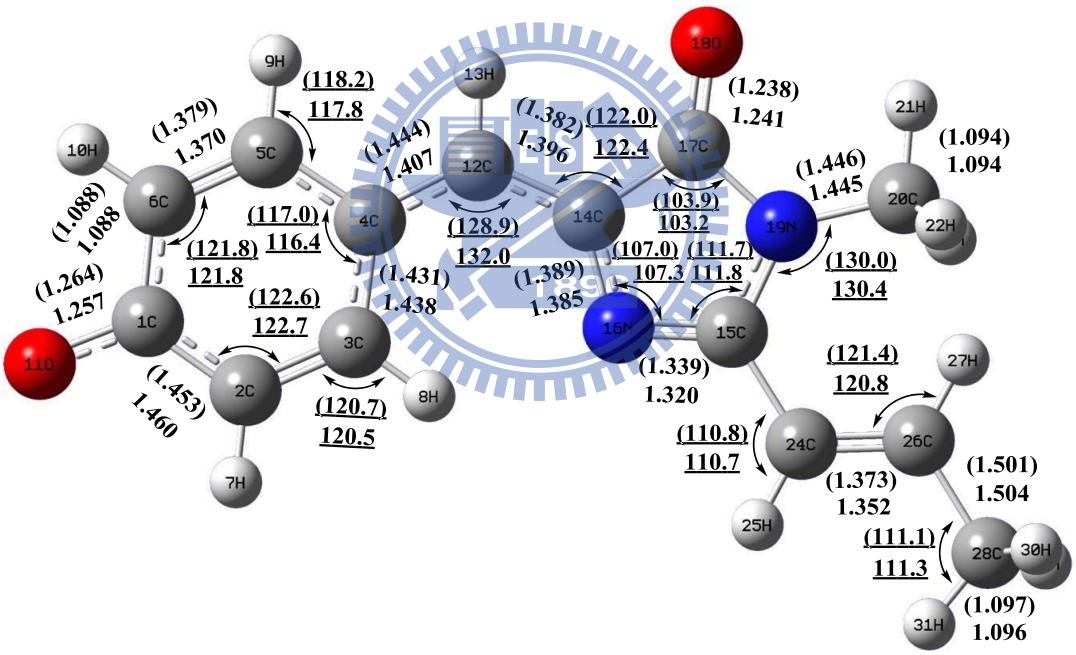

Fig. 59 B3LYP/6-31+G(d) and TD-B3LYP/6-31+G(d) optimized geometries of the S_0 and S_1 states for the anionic form of the **HBMPI** in gas phase. The bond lengths (bold, in angstrom) and angles (underline, in degree) of S_1 are provided in the brackets.

4.4.2 Vibrational Frequencies of HBMPI for C_1 Symmetry

The calculated vibrational frequencies of S_0 and S_1 states and its corresponding Huang-Rhys factors are listed in **Table 24**. All 87 vibrational frequencies are shown no imaginary frequency in B3LYP/TD-B3LYP calculation. The largest value of Huang-Rhys factors is 0.3048 for mode 68.

Table 24 Unscaled calculated vibrational frequencies of the S_0 (ω_j, cm^{-1}) and S_1 (ω'_j, cm^{-1}) for C_1 symmetry using B3LYP/TD-B3LYP method. The corresponding Huang-Rhys factors (S^{HF}, dimensionless) and the 3rd derivative of S_0 potential energy surface (K_{j3}, Hartree*amu$^{-3/2}$*Bohr^{-3}) are also shown.

Mode	ω_j	ω'_j	S^{HF}	K_{j3}	Mode	ω_j	ω'_j	S^{HF}	K_{j3}
1	3215	3214	0.0008	1.17581	**45**	1002	984	0.0000	0.00000
2	3192	3196	0.0106	1.15766	**46**	994	967	0.0000	0.00000
3	3179	3182	0.0017	-1.08349	**47**	989	966	0.0047	-0.00026
4	3172	3174	0.0008	-1.10790	**48**	977	947	0.0000	0.00000
5	3159	3171	0.0056	-1.17285	**49**	977	915	0.0120	0.00499
6	3148	3155	0.1751	1.08500	**50**	947	909	0.0000	0.00000
7	3137	3138	0.0046	0.90714	**51**	922	857	0.1851	-0.00083
8	3129	3136	0.0651	0.95594	**52**	864	833	0.0000	0.00000
9	3097	3095	0.0748	-0.96020	**53**	839	830	0.0272	0.00417
10	3079	3083	0.0000	0.00016	**54**	812	810	0.0073	0.00432
11	3035	3039	0.0000	0.00000	**55**	807	782	0.0000	0.00000
12	3028	2963	0.0007	-0.66650	**56**	798	777	0.0000	0.00000
13	3004	2951	0.0028	0.66780	**57**	795	733	0.0798	-0.00050
14	1709	1696	0.0752	-0.06573	**58**	760	724	0.0000	0.00000
15	1694	1663	0.0304	-0.01946	**59**	757	705	0.0023	-0.00417
16	1664	1613	0.0000	0.03575	**60**	736	701	0.0000	0.00000
17	1621	1565	0.0042	-0.00290	**61**	676	655	0.0000	0.00000
18	1591	1534	0.0164	0.01971	**62**	673	625	0.0044	0.00075
19	1543	1521	0.0611	-0.00339	**63**	629	589	0.0157	0.00006
20	1534	1520	0.0000	-0.00452	**64**	593	585	0.0019	0.00016
21	1524	1506	0.0000	0.00004	**65**	541	521	0.0000	0.00000
22	1524	1493	0.0361	0.01241	**66**	522	511	0.0062	-0.00004
23	1508	1478	0.0078	-0.01918	**67**	493	452	0.0000	0.00000
24	1502	1473	0.0000	0.00000	**68**	457	450	0.3048	0.00011
25	1489	1465	0.1954	0.00702	**69**	423	405	0.0000	0.00000

26	1477	1437	0.0212	-0.00831	**70**	408	396	0.0050	-0.00005
27	1461	1428	0.0002	0.00418	**71**	357	346	0.0000	0.00000
28	1432	1417	0.0059	0.02199	**72**	346	311	0.0138	-0.00055
29	1422	1415	0.0004	0.00538	**73**	302	303	0.1238	-0.00013
30	1411	1349	0.0109	0.00408	**74**	269	246	0.0000	0.00000
31	1364	1330	0.2628	-0.00050	**75**	253	238	0.1043	-0.00007
32	1335	1325	0.0196	0.01234	**76**	241	225	0.0000	0.00000
33	1324	1296	0.0000	-0.00748	**77**	219	209	0.0000	0.00000
34	1318	1293	0.0279	0.00214	**78**	211	206	0.0093	0.00000
35	1288	1271	0.0747	0.00000	**79**	194	176	0.0000	0.00000
36	1279	1224	0.1842	0.00000	**80**	173	150	0.0000	0.00000
37	1221	1204	0.1829	-0.00014	**81**	146	102	0.0020	-0.00009
38	1194	1167	0.0034	-0.00220	**82**	119	100	0.0000	0.00000
39	1185	1156	0.0000	0.00138	**83**	96	87	0.0000	0.00000
40	1157	1116	0.0000	0.00000	**84**	70	60	0.0000	0.00000
41	1122	1109	0.0473	0.01820	**85**	58	48	0.1757	0.00000
42	1112	1076	0.0079	0.00036	**86**	45	38	0.0000	0.00000
43	1066	1043	0.0000	0.00000	**87**	42	20	0.0000	0.00000
44	1047	998	0.2541	-0.00443					

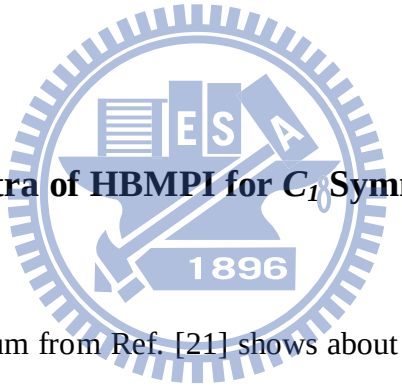

4.4.3 Absorption Spectra of HBMPI for C_1 Symmetry

The experimental spectrum from Ref. [21] shows about 4300 cm^{-1} for FWHM (see **Fig. 60(a)**) in 1 M KOH. From **Fig. 60(b)**, the B3LYP/TD-B3LYP simulation is shifted with 900 cm^{-1} blue shift for the maximum absorption but the FWHM is a little larger about 1800 cm^{-1}. For experimental spectra of neutral **HBDI** and anionic **HBMPI**, the absorption maxima of anionic **HBMPI** is shifted to 462 nm due to the extension of the conjugated system compared to neutral **HBDI** (370 nm).

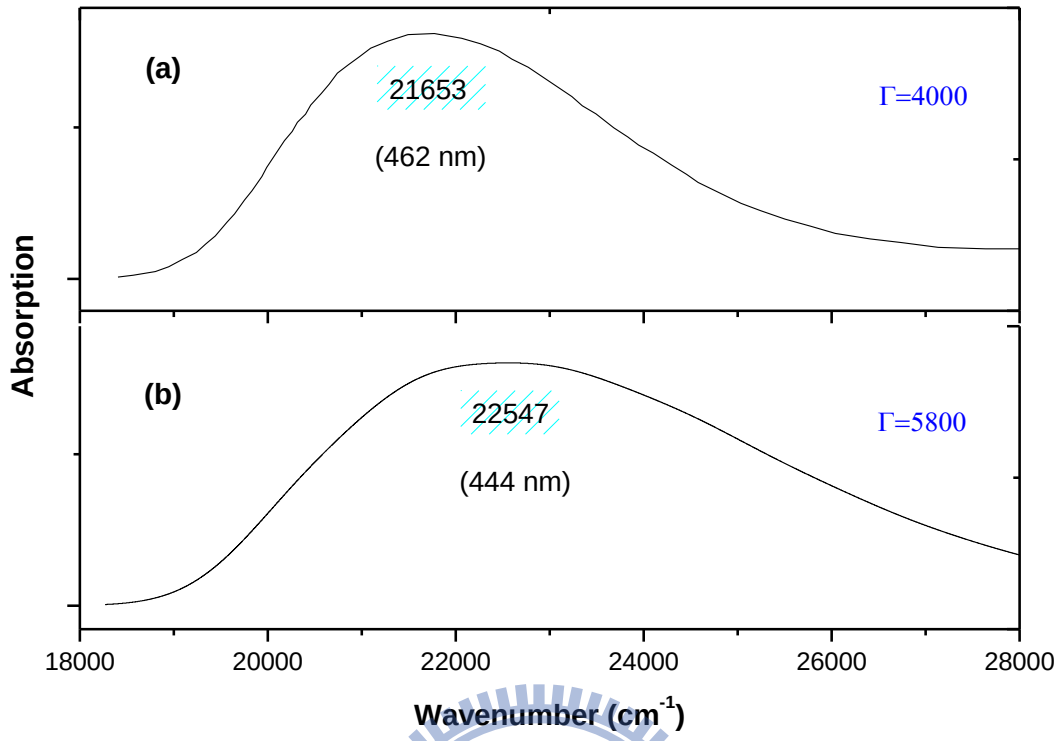

Fig. 60 Absorption spectra of the anionic form of the **HBMPI** at 77K. (a) Experiment spectrum from Ref. [21], (b) simulated spectrum for r_{ba} = 10 cm^{-1} and D_{ba} = 1000 cm^{-1} from B3LYP/TD-B3LYP calculation.

Chapter 5 Conclusions

From the theoretical perspective, discussing the electronic structure of isolated chromophores is the first step toward understanding their photochemical properties in the protein environments. The strategy is keeping the primary geometry of the chromophore to model isolated chromophore species and then calculating the molecular properties of the chromophores in the gas phase and in solution using quantum mechanical methods. In view of successful PCM method form the literatures, taking solvent interactions with a chromophore into account is a basic way to describe the protein environment, and they really play an important role for both absorption and fluorescence spectra. So far, only few studies have ever tried to discuss the Franck-Condon simulation of the GFP chromophore. A great deal of effort has been made on the absorption and fluorescence spectra in various solvents. However, it seems to be lacking for the Franck-Condon approach with including inhomogeneous broadening of solvent effect.

In the present work, it is quite similar between the equilibrium geometries of S_0 and S_1 with and without PCM by combination of B3LYP/TD-B3LYP method. There is something particularly noteworthy in the Franck-Condon simulation. Although the equilibrium geometries do not change too much, the differences would be observed from those absorption or fluorescence spectra which is a directly evidence.

So far, we have demonstrated that peak positions and spectral widths of neutral **HBDI** by B3LYP/TD-B3LYP with and without PCM method, which is shown in a good agreement compared with the experimental spectrum. Another thing has to be noticed is anharmonic Franck-Condon simulation which is shifted less than a few hundreds of wavenumbers. To sum up, spectral peaks and widths of absorption and

fluorescence are well reproduced by the present Franck-Condon simulation combining with inhomogeneous broadening of solvent effect.

But the simulation spectra for the anionic form of **HBI** and **wt-GFP** do not give a better agreement with respect to the experimental spectrum. The problem which we must solve next is to improving the spectral widths of anionic **HBI** and **wt-GFP**. For anionic **HBMPI** case, the single-double bond in the bridge both links the Π-systems on the two rings to form the larger conjugated system and the more extended conjugated Π-system in the chromophore may cause the significant red shift of the **DsRed** absorption properties compared to those of GFP.

Three different DFT exchange-correlation functionals and HF, which contain different HF exchanges, were used and the results of simulation gave the evidence for indicating that the correlation functionals are really important. Thus, the most likely explanation is that the more HF exchange is contained in DFT exchange-correlation functionals may cause the blue shift.

Now that we are sure that absorption and fluorescence spectra are good in present Franck-Condon simulation, the next step is to expand green fluorescence into red, blue, yellow, and so on. The spectral diversity is obtained by variant connections of the imidazolinone ring and the interactions with their protein environment. In the future, a palette of fluorescence simulation would be accomplished.

References

1. SHIMOMURA, O., *The discovery of aequorin and green fluorescent protein.* Journal of Microscopy, 2005. **217**(1): p. 3-15.
2. Tsien, R.Y., *THE GREEN FLUORESCENT PROTEIN.* Annu. Rev. Biochem, 1998. **67**: p. 509-544.
3. SHIMOMURA, O., *A Short Story of Aequorin.* Biol. Bull., 1995. **189**: p. 1-5.
4. Zimmer, M., *GFP: from jellyfish to the Nobel prize and beyond.* Chem. Soc. Rev., 2009. **38**: p. 2823-2832.
5. Mats Ormö, A.B.C., Karen Kallio, Larry A. Gross, Roger Y. Tsien and S. James Remington, *Crystal Structure of the Aequorea victoria Green Fluorescent Protein.* Science 1996. **273**: p. 1392-1395.
6. Katjuša Brejc, T.K.S., Paul A. Kitts, Steven R. Kain, Roger Y. Tsien, Mats Ormö , and S. James Remington, *Structural basis for dual excitation and photoisomerization of the Aequorea victoria green fluorescent protein.* Proc. Natl. Acad. Sci. USA, 1997. **94**: p. 2306-2311.
7. SHIMOMURA, O., *Structure of the chromophore of Aequorea green fluorescent protein.* FEBS LETTERS, 1979. **104**(2): p. 220-222.
8. Chris W. Cody, D.C.P., William M. Westler, Franklyn G. Prendergast, William W. Ward, *Chemical structure of the hexapeptide chromophore of the Aequorea green-fluorescent protein.* Biochemistry, 1993. **32**: p. 1212-1218.
9. R Heim, D.C.P., and R Y Tsien *Wavelength mutations and posttranslational autoxidation of green fluorescent protein.* Biochemistry, 1994. **91**: p. 12501-12504.
10. Andrew B. Cubitt, R.H., Stephen R. Adams, Aileen E. Boyd, Larry A. Gross and Roger Y. Tsien, *Understanding, improving and using green fluorescent proteins* Trends in Biochemical Sciences, 1995. **20**(1): p. 448-455.
11. G.H. Patterson, S.M.K., W.D. Sharif, S.R. Kain and D.W. Piston, *Use of the green fluorescent protein and its mutants in quantitative fluorescence microscopy.* Biophysical Journal, 1997. **73**(5): p. 2782-2790.
12. S. B. Nielsen, A.L., J. U. Andersen, U.V. Pedersen, S. Tomita, and L. H. Andersen, *Absorption Spectrum of the Green Fluorescent Protein Chromophore Anion In Vacuo.* Phys. Rev. Lett., 2001. **87**(22): p. 228102.
13. M Chattoraj, B.A.K., G U Bublitz, and S G Boxer, *Ultra-fast excited state dynamics in green fluorescent protein: multiple states and proton transfer.* Proc. Natl. Acad. Sci. USA, 1996. **93**: p. 8362-8367.
14. Gerold Bublitz, B.A.K., and Steven G. Boxer, *Electronic Structure of the Chromophore in Green Fluorescent Protein (GFP).* J. Am. Chem. Soc., 1998. **120**: p. 9370-9371.

15. Maria Elena Martin, F.N., Massimo Olivucci, *Origin, Nature, and Fate of the Fluorescent State of the Green Fluorescent Protein Chromophore at the CASPT2//CASSCF Resolution.* J. AM. CHEM. SOC., 2004. **126**: p. 5452-5464.
16. Naomi M. Webber, a.S.R.M., *Electronic spectroscopy and solvatochromism in the chromophore of GFP and the Y66F mutant.* Photochem. Photobiol. Sci., 2007. **6**: p. 976-981.
17. Deborah Stoner-Ma, E.H.M., Jérôme Nappa, Kate L. Ronayne, Peter J. Tonge, and Stephen R. Meech, *Proton Relay Reaction in Green Fluorescent Protein (GFP): Polarization-Resolved Ultrafast Vibrational Spectroscopy of Isotopically Edited GFP.* J. Phys. Chem. B, 2006. **110**(43): p. 22009-22018.
18. Deborah Stoner-Ma, A.A.J., Kate L. Ronayne, Je´roˆme Nappa, Peter J. Tonge, Stephen R. Meech, *Ultrafast electronic and vibrational dynamics of stabilized A state mutants of the green fluorescent protein (GFP): Snipping the proton wire.* Chemical Physics, 2008. **350**(1-3): p. 193-200.
19. Konstantin L. Litvinenko, N.M.W., and Stephen R. Meech, *Internal Conversion in the Chromophore of the Green Fluorescent Protein: Temperature Dependence and Isoviscosity Analysis.* J. Phys. Chem. A, 2003. **107**(15): p. 2616-2623.
20. Larry A. Gross, G.S.B., Ross C. Hoffman, Kim K. Baldridge, and Roger Y. Tsien, *The structure of the chromophore within DsRed, a red fluorescent protein from coral.* Proc Natl Acad Sci USA 2000. **97**: p. 11990-11995.
21. Xiang He, A.F.B., and Peter J. Tonge, *Synthesis and Spectroscopic Studies of Model Red Fluorescent Protein Chromophores.* Org. Lett., 2002. **4**(9): p. 1523-1526.
22. Se´verine Boye, S.B.N., Helle Krogh, Iben Bloch Nielsen, Ulrik V. Pedersen, Alasdair F. Bell, Xiang He, Peter J. Tonge, and Lars H. Andersen, *Gas-phase absorption properties of DsRed model chromophores.* Phys. Chem. Chem. Phys., 2003. **5**: p. 3021-3026.
23. A. P. Esposito, P.S., W. W. Parson, and P. J. Reid, *Vibrational spectroscopy and mode assignments for an analog of the green fluorescent protein chromophore.* Journal of Molecular Structure, 2001. **569**(1-3): p. 25-41.
24. Chaoyuan Zhu, K.K.L., Michitoshi Hayashi, and Sheng Hsien Lin, *Theoretical treatment of anharmonic effect on molecular absorption, fluorescence spectra, and electron transfer.* Chemical Physics, 2009. **358**(1-2): p. 137-146.
25. Lieb, E.H., *Thomas-fermi and related theories of atoms and molecules.* Reviews of Modern Physics, 1981. **53**(4): p. 603.
26. Hohenberg, P.a.K., W., *Inhomogeneous Electron Gas.* Physical Review, 1964.

136(3B): p. B864.

27. Holthausen, W.K.a.M.C., *A Chemist's Guide to Density Functional Theory, Second Edition.* Wiley-VCH, 2001.
28. Kohn, W.a.S., L. J., *Self-Consistent Equations Including Exchange and Correlation Effects.* Physical Review, 1965. **140**(4A): p. A1133.
29. Kohn, W., *Nobel Lecture: Electronic structure of matter—wave functions and density functionals.* Reviews of Modern Physics, 1999. **71**(5): p. 1253.
30. Becke, A.D., *A new mixing of Hartree–Fock and local density-functional theories.* J. Chem. Phys., 1993. **98**: p. 1372.
31. Becke, A.D., *Density-functional exchange-energy approximation with correct asymptotic behavior.* Physical Review A, 1988. **38**(6): p. 3098.
32. Becke, A.D., *Density-functional thermochemistry. III. The role of exact exchange* J. Chem. Phys., 1993. **98**.
33. Runge, E.a.G., E. K. U., *Density-Functional Theory for Time-Dependent Systems.* Physical Review Letters, 1984. **52**(12): p. 997.
34. Gross, M.A.L.M.a.E.K.U., *TIME-DEPENDENT DENSITY FUNCTIONAL THEORY.* Annu. Rev. Phys. Chem., 2004. **55**: p. 427-455.
35. E. Cances, B.M., and J. Tomas, *A new integral equation formalism for the polarizable continuum model: Theoretical background and applications to isotropic and anisotropic dielectrics.* J. Chem. Phys., 1997. **107**: p. 3032.
36. Maurizio Cossi, V.B., Roberto Cammi, and Jacopo Tomasi, *Ab initio study of solvated molecules: a new implementation of the polarizable continuum model.* Chemical Physics Letters, 1996. **255**: p. 327-335.
37. Jacopo Tomasi, B.M., and Roberto Camm, *Quantum Mechanical Continuum Solvation Models.* Chem. Rev., 2005. **105**(8): p. 2999-3094.
38. Giovanni Scalmani, M.J.F., Benedetta Mennucci, Jacopo Tomasi, Roberto Cammi, and Vincenzo Barone, *Geometries and properties of excited states in the gas phase and in solution: Theory and application of a time-dependent density functional theory polarizable continuum model* J. Chem. Phys., 2006. **124**: p. 094107
39. S. H. Lin, C.H.C., K. K. Liang, R. Chang, Y. J. Shiu, J. M. Zhang, T.-S. Yang, M. Hayashi, and F. C. Hsu, *Ultrafast Dynamics and Spectroscopy of Bacterial Photosynthetic Reaction Centers.* Advances in Chemical Physics, 2002. **121**: p. 1-88.
40. M. J. Frisch, G.W.T., H. B. Schlegel et al., *GAUSSIAN 09, Revisions A.02.* Gaussian, Inc., Wallingford, CT, 2009.
41. Radom, A.P.S.a.L., *Harmonic Vibrational Frequencies: An Evaluation of Hartree-Fock, Møller-Plesset, Quadratic Configuration Interaction, Density*

Functional Theory, and Semiempirical Scale Factors. J. Phys. Chem., 1996. **100**(41): p. 16502-16513.

42. Kyril M. Solntsev, O.P., Jian Dong, Julien Rehault, Yongbing Lou, Clemens Burda, and Laren M. Tolbert, *Meta and Para Effects in the Ultrafast Excited-State Dynamics of the Green Fluorescent Protein Chromophores.* J. Phys. Chem. B, 2008. **112**(9): p. 2700-2711.
43. Jian Dong, K.M.S., and Laren M. Tolbert, *Solvatochromism of the Green Fluorescence Protein Chromophore and Its Derivatives.* J. Am. Chem. Soc., 2006. **128**(37): p. 12038-12039.
44. V. Helms, C.W., and P.W. Langhoff, *Low-lying electronic excitations of the green fluorescent protein chromophore.* Journal of Molecular Structure (Theochem), 2000. **506**(1-3): p. 179-189.
45. I. V. Polyakov, B.L.G., E. M. Epifanovsky, A. I. Krylov, and A. V. Nemukhin, *Potential Energy Landscape of the Electronic States of the GFP Chromophore in Different Protonation Forms: Electronic Transition Energies and Conical Intersections.* J. Chem. Theory Comput., 2010. **6**(8): p. 2377-2387.
46. Miki Kurimoto, P.S., Richard W. Gurney, Scott Lovell, Jean Chmielewski, and Bart Kahr, *Kinetic Stabilization of Biopolymers in Single-Crystal Hosts: Green Fluorescent Protein in r-Lactose Monohydrate.* J. Am. Chem. Soc., 1999. **121**: p. 6952-6953.
47. Azuma Matsuura, T.H., Hiroyuki Sato, Atsuya Takahashi, and Minoru Sakurai, *Theoretical study on the absorption maxima of real GFPs.* Chemical Physics Letters, 2010. **484**(4-6): p. 324-329.
48. L. Lammich, M.Å.P., M. Brøndsted Nielsen, and L. H. Andersen, *The Gas-Phase Absorption Spectrum of a Neutral GFP Model Chromophore.* Biophysical Journal, 2007. **92**(1): p. 201-207.
49. Riccardo Nifosı, a.Y.L., *Predictions of Novel Two-Photon Absorption Bands in Fluorescent Proteins.* J. Phys. Chem. B, 2007. **111**(50): p. 14043-14050.
50. Nifosi, V.T.a.R., *Ab Initio Molecular Dynamics of the Green Fluorescent Protein (GFP) Chromophore: An Insight into the Photoinduced Dynamics of Green Fluorescent Proteins.* J. Phys. Chem. B,, 2001. **105**(24).